



Virginia Commonwealth University
VCU Scholars Compass

Theses and Dissertations

Graduate School

2018

Biosensing and Catalysis Applications of Nanoporous Gold (NPG) and Platinum-Speckled Nanoporous Gold (NPG-Pt) Electrodes

Christopher J. Freeman
Virginia Commonwealth University

Follow this and additional works at: <https://scholarscompass.vcu.edu/etd>

 Part of the [Analytical Chemistry Commons](#), and the [Materials Chemistry Commons](#)

© The Author

Downloaded from

<https://scholarscompass.vcu.edu/etd/5473>

This Dissertation is brought to you for free and open access by the Graduate School at VCU Scholars Compass. It has been accepted for inclusion in Theses and Dissertations by an authorized administrator of VCU Scholars Compass. For more information, please contact libcompass@vcu.edu.

Biosensing and Catalysis Applications of Nanoporous Gold (NPG) and Platinum-Speckled Nanoporous Gold (NPG-Pt) Electrodes

A dissertation in partial fulfillment of the requirements for the degree of Doctor of Philosophy at
Virginia Commonwealth University

by

Christopher James Freeman

Bachelor of Science - Chemistry, Virginia Commonwealth University, Richmond, VA USA,
2011

Director: Dr. Maryanne M. Collinson

Professor of Chemistry

Virginia Commonwealth University

Richmond, VA

May, 2018

Acknowledgements

The first people I would like to thank are my wife Pryce and my boys, Flynn and Shay, whose help, love, and support made this journey to a Ph.D. possible. Without them, I could not have come this far. My mother-in-law and sister-in-law, Peggy York and Galyn Norwood, also deserve thanks for reading and editing pages upon pages of chemistry, even though chemistry is not their bailiwick. I would also like to thank my advisor Dr. Maryanne Collinson whose knowledge, guidance, and support was instrumental in my pursuit of a graduate degree, encouraging me through the hard days of research. Dr. Collinson, along with Dr. Ruder, believed in me and helped cultivate my love of chemistry, encouraging me to return to VCU. Dr. Ruder knew, before I did, that this was the path for me. Another big thank you goes to Dr. Sarah Rutan, whose interest in my personal and professional growth helped me refine and broaden my skills, highlighting the importance of a polished product. Additionally, I would like to extend thanks to Dr. Julio Alvarez, and Dr. Dexian Ye, who have devoted their time and energy to my development, ultimately making me a better, more rounded chemist. I would like to extend a thank you to Dr. Joseph Reiner who provided many hours of inspiring and thoughtful conversation during our collaboration and beyond. Thank you to Dr. Dmitry Pestov and Dr. Naveen Kumar Palapati and the Nanocharacterization Core Facility. Finally, I want to thank Virginia Commonwealth University and the Department of Chemistry.

Table of Contents

| | |
|--|------|
| Acknowledgements | ii |
| List of Figures | viii |
| List of Tables | xv |
| List of Abbreviations | xvi |
| Abstract | xxi |
| Chapter 1: Introduction | 1 |
| 1.1. Introduction..... | 2 |
| 1.2. Nanoporous Gold (NPG) Electrodes | 4 |
| 1.2.1. Fabrication Methods | 5 |
| 1.2.2. Nanoporous Gold Substrates..... | 9 |
| 1.3. Small Volume Electrochemical Measurements | 10 |
| 1.3.1. Microvials | 10 |
| 1.3.2. Stationary Drops | 12 |
| 1.3.3. Lab-on-Chip Design and Flow Cells | 12 |
| 1.3.4. Miniaturized Electrodes | 15 |
| 1.4. Additional Material Incorporation | 16 |
| 1.4.1. Platinum | 17 |
| 1.4.2. Palladium | 18 |
| 1.4.3. Rhodium..... | 19 |

| | |
|---|----|
| 1.4.4. Ruthenium..... | 19 |
| 1.4.5. Surface Modification | 20 |
| 1.5. Sensing Applications | 21 |
| 1.5.1. Enzymatic | 21 |
| 1.5.2. DNA..... | 21 |
| 1.5.3. Immunosensors | 22 |
| 1.5.4. Direct Sensing..... | 23 |
| 1.5.4.1. Ascorbic Acid | 23 |
| 1.5.4.2. Cysteine..... | 25 |
| 1.5.4.3. Uric Acid..... | 26 |
| 1.5.4.4. Glucose | 27 |
| 1.5.4.5. Hydrogen Peroxide | 28 |
| 1.6. Fuel Cell Catalysis | 28 |
| 1.6.1. Types..... | 29 |
| 1.6.2. Fuels | 32 |
| 1.6.2.1. Methanol | 33 |
| 1.6.2.2. Ethanol | 34 |
| 1.6.2.3. Formic Acid | 35 |
| 1.7. Thesis Statement | 36 |
| 1.8. References..... | 37 |
| Chapter 2: Instrumentation and Characterization | 48 |
| 2.1. Introduction..... | 49 |
| 2.2. Electrochemistry | 49 |
| 2.2.1. Cyclic Voltammetry..... | 50 |
| 2.2.2. Chronoamperometry | 53 |

| | |
|---|----|
| 2.2.3. Potentiometry | 54 |
| 2.3. Scanning Electron Microscopy | 55 |
| 2.4. X-ray Photoelectron Spectroscopy | 58 |
| 2.5. References | 60 |
| Chapter 3: Electrochemical Comparison of Nanoporous Gold (NPG) to Planar Gold (PG) in the Presence of Biofouling Solutions..... | 61 |
| 3.1. Introduction..... | 62 |
| 3.2. Experimental | 63 |
| 3.2.1. Electrode preparation | 63 |
| 3.2.2. Electrochemical procedures | 64 |
| 3.3. Results and Discussion | 65 |
| 3.3.1. Background | 65 |
| 3.3.2 Potentiometry of $[\text{Fe}(\text{CN})_6]^{3-}/[\text{Fe}(\text{CN})_6]^{4-}$ | 66 |
| 3.3.3. Potentiometry of Ascorbic Acid: An Unpoised System | 71 |
| 3.3.4. Blood Redox Potential | 73 |
| 3.4. Conclusions..... | 76 |
| 3.5. References | 77 |
| Chapter 4: Fabrication of Microdroplet Nanoporous Gold (MDNPG) Electrodes and Performance of Potentiometric Measurements in Ultra-small Volumes | 80 |
| 4.1. Introduction..... | 81 |
| 4.2. Experimental Section | 83 |
| 4.2.1. Materials | 83 |
| 4.2.2. Nanoporous Gold (NPG) Preparation | 84 |
| 4.2.3. Droplet Formation and Mixing | 84 |
| 4.2.4. Data Collection and Analysis..... | 86 |
| 4.2.5. Preparation of Nanoporous Gold (NPG) on Glass..... | 87 |

| | |
|--|-----|
| 4.3. Results and Discussion | 90 |
| 4.3.1. Measurement of Open-Circuit Potentials (OCP) in Subnanoliter Droplets..... | 90 |
| 4.3.2. Poised Redox Reactions..... | 94 |
| 4.3.3. Unpoised Redox Reactions | 96 |
| 4.4. Conclusions..... | 99 |
| 4.5. References..... | 100 |
| Chapter 5: Electrochemical Applications of Fabricated Mini-Nanoporous Gold (mNPG) Electrodes and Platinum-Speckled Mini-Nanoporous Gold (mNPG-Pt) Electrodes | |
| 5.1. Introduction..... | 104 |
| 5.2. Experimental Methods | 108 |
| 5.2.1. Materials | 108 |
| 5.2.2 Capillary Tube Functionalization and Nanoporous Gold Preparation..... | 108 |
| 5.2.3. Electrochemical Measurements | 109 |
| 5.2.4. Electrode Characterization..... | 110 |
| 5.3. Results and Discussion | 111 |
| 5.3.1. Electrode Validation and Redox Molecule Response..... | 111 |
| 5.3.2. Incorporation of Platinum into mNPG Electrodes..... | 122 |
| 5.3.3. Comparison of mNPG to mNPG-Pt Electrodes and Investigation of Response Enhancement..... | 128 |
| 5.3.4. Response of Cysteine in the Presence of Multiple Species at Physiological Concentrations | 132 |
| 5.4. Conclusion | 134 |
| 5.5. References..... | 135 |
| Chapter 6: Electrocatalytic Applications of Platinum-Speckled mini-Nanoporous Gold (mNPG-Pt) Electrodes Fabricated on a Functionalized, Low Cost Glass Substrate | |
| | 138 |

| | |
|--|-----|
| 6.1. Introduction..... | 139 |
| 6.2. Experimental Methods and Electrode Characterization | 142 |
| 6.3. Electro-oxidation of Fuel Possibilities..... | 143 |
| 6.4. Conclusion | 147 |
| 6.5. References..... | 149 |
| Chapter 7: Conclusions and Future Work..... | 151 |
| 7.1. Conclusions..... | 152 |
| 7.2. Future Work..... | 156 |
| 7.2.1. Miniaturized Device Fabrication | 156 |
| 7.2.2. Specific Surface Modification | 156 |
| 7.2.3. Increased Platinum Loading for Direct Oxidation..... | 157 |
| 7.3. References..... | 158 |
| Vita..... | 159 |

List of Figures

Chapter 1

Figure 1.1. Simplified graphical representation of the surface of nanoporous gold and planar gold in the presence of albumin and a small redox molecule in solution. Electron transfer is hindered at planar gold but not at nanoporous gold. Reprinted with permission from ref. 435

Figure 1.2. Different electrochemical approaches for the preparation of nanoporous gold (NPG) electrode on gold support: (a) top-down, (b) bottom-up, and (c and c') combination of both bottom-up and top-down approaches. Adopted from ref. 496

Figure 1.3. (a) Cartoon representation of a fabricated microvial from a glass capillary and gold wire working electrode. Adopted from ref. 79 (b) top-view optical image of a glass capillary microvial fabricated using chloridized silver wire. Adopted from ref. 80.....11

Figure. 1.4. Cartoon representation of a single drop measurement using multiple gold electrodes, a reference membrane, and sample on a glass microscope slide. Reprinted with permission from ref. 82.12

Figure. 1.5. Sketches of the construction of individually driven interdigitated gold electrodes and IDA gold electrodes assembled into microfluidic cells. (A) Top schematic view of the microfluidic device. (1) Inlet; (2) reference electrode, located next to inlet to the cell; (3) reference electrode, located next to outlet to the cell; (4) outlet and auxiliary electrode; (E_1 – E_4) working electrodes. (B) Schematic illustration of the construction of a microfluidic cell with four individually driven gold electrodes. (a) Polycarbonate slice with finished Au working electrodes (E_1 – E_4) and orifices for flow inlet and outlet, and toner mask of channels (wax paper not shown) before application; (b) same components of (a) after heat-transfer of toner channel; (c) microfluidic flow cell before heat-sealing of the second polycarbonate slice; (d) complete microfluidic cell with two attached miniaturized Ag/AgCl reference electrodes. Adopted from ref. 87.14

Figure 1.6. Scheme of fabrication of cylindrical macroporous gold electrode (a) glass capillary tube (b) electroless Ag coating, (c) silica particle template deposition, (d) electrodeposition of thin Ni layer onto Ag, (e) electrodeposition of Au into voids, (f) insertion of second macroporous electrode into capillary tube, (g) sealing of structure, (h) etching of template and glass capillary using HF. Adopted from ref. 88.....15

Figure 1.7. Cartoon representation of a sandwich-like antibody-antigen complex used in immunosensors.22

Chapter 2

Figure 2.1. Cartoon representation of a standard (a) two-electrode and (b) three-electrode electrochemical cell with working electrode (**WE**), reference electrode (**RE**) and auxiliary electrode (**AE**).....50

Figure 2.2. (a) Waveform for cyclic voltammetry showing the potential change from the initial potential (E_i) to a final potential (E_f) and back to initial. (b) Corresponding voltammogram of the forward, anodic scan and the reverse, cathodic scan of an ideal reversible redox reaction where E is the potential in volts and i is current in amps. Arrow denotes scan direction.....51

Figure 2.3. Cyclic voltammetry used to determine the electroactive surface area (EASA) of electrodes using (a) reduction of gold oxide peak and (b) desorption of hydrogen on platinum. The area under the curve represents the charge passed over the electrode and can be converted to area using the standard charge per unit area for gold ($390 \mu\text{C}/\text{cm}^2$) and platinum ($210 \mu\text{C}/\text{cm}^2$), respectively. 53

Figure 2.4. (a) Waveform for chronoamperometry showing no change in the potential from the initial potential (E_i). (b) Corresponding response of current over time.54

Figure 2.5. Structure of a scanning electron microscope (SEM). Reprinted with permission from ref. 756

Figure 2.6. The interaction zone of electrons and specimen atoms below a specimen surface. Adopted from ref. 7.....57

Figure 2.7. Cartoon representation of the excitation of emitted core shell photoelectrons due to kinetic energy transfer from incident X-rays.58

Chapter 3

Figure 3.1. Schematic representation of nanoporous gold (NPG) preparation in nitric acid for 13 minutes and rinsed in DI water. Electrode is fabricated by capturing dealloyed square onto a cut planar gold slide.64

Figure 3.2. Reprinted with permission from reference 1. Copyright 2016, The Electrochemical Society. (a) OCP- time traces acquired at a biofouled planar gold electrode in 0.20 mM $[\text{Fe}(\text{CN})_6]^{3-}$ in pH 7.4 phosphate buffer following successive additions of $[\text{Fe}(\text{CN})_6]^{4-}$ (b) Corresponding Nernst plot. The solid line is the linear regression fit to the data points: $y = -0.0598x + 0.153$; $R^2 = 0.997$. (c) CV acquired at the end of the potentiometric experiment, 50 mV/s. The final concentrations of ferri/ferrocyanide in solution were 0.18/0.22 mM.67

Figure 3.3. Reprinted with permission from reference 1. Copyright 2016, The Electrochemical Society. SEM images of nanoporous gold (NPG) at four different magnifications. Inset shows cross-sectional image.68

Figure 3.4. Reprinted with permission from reference 1. Copyright 2016, The Electrochemical Society. (a) OCP-time traces acquired at NPG after exposure to fibrinogen. The solution initially contained in 0.1 mM potassium ferricyanide in pH 7.4 phosphate buffer to which increments of potassium ferrocyanide were added. (b) Nernst slope (absolute value) obtained at biofouled planar gold (red) and nanoporous gold (black) electrodes at three different concentrations. Error bars represent the standard deviations from six electrodes made on different days.69

Figure 3.5. Reprinted with permission from reference 1. Copyright 2016, The Electrochemical Society. CVs acquired at the end of the potentiometric experiment, 50 mV/s, at nanoporous gold (NPG) and planar gold. The final concentrations of ferri/ferrocyanide were 0.095/0.095 (top) or 0.072/0.075 mM (bottom) in pH 7.4 phosphate buffer. The electrodes were soaked in 1 mg/mL fibrinogen for several hours prior to the potentiometric experiments.70

Figure 3.6. Reprinted with permission from reference 1. Copyright 2016, The Electrochemical Society. (a) Nernst plot for the addition of ascorbic acid to pH 7.4 phosphate buffer. The solid line is the linear regression fit to the data points: slope = -42.5 mV, $R^2 = 0.999$. (b) Background subtracted CVs of 0.27 mM ascorbic acid in buffer at 50 mV/s at nanoporous gold (NPG) and planar gold electrodes. (c) Background subtracted CVs of ascorbic acid after modification of the electrodes with 1 mg/mL fibrinogen for several hours.72

Figure 3.7. Reprinted with permission from reference 1. Copyright 2016, The Electrochemical Society. (a) Continuous OCP-time traces acquired at unmodified nanoporous gold (NPG) and planar gold in heparinized human plasma (b) CVs acquired at the end of the potentiometric experiments, 50 mV/s.74

Chapter 4

Figure 4.1. Reprinted with permission from reference 1. American Chemical Society Copyright 2016. Schematic illustration of the droplet-based OCP measurement apparatus. (A) The relevant components are mounted onto an inverted microscope with manipulation stages and a CCD camera as described in the main text. (A,i) Top down and (A,ii) side view of the microscope slide-based holder. A 1 cm hole drilled through a microscope slide is sealed from the bottom by a #1.5 glass coverslip that has a nanoporous gold leaf attached. A copper lead is attached to this

gold leaf and serves as the ground reference connection. The ca. 100 μL well is filled with hexadecane solution to prevent the aqueous droplets from evaporating. (A,iii) A closer view near a single droplet shows that the receiving droplet is in contact with the nanoporous (NP) gold substrate. (A,iv) A closer look at the nanoporous electrode via an SEM scan shows the porous nature of the electrode. (B) A schematic illustration of the droplet-measurement protocol. (B,i) Backing pressure is applied to a pipet containing the receiving solution (blue), and the pipet is lowered to attach the droplet onto the NP electrode. (B,ii) The end of a micropipette containing the reference solution (purple, 0.1 M KCl) is positioned inside the receiving droplet. (B,iii) Backing pressure is applied to a second pipet containing the injection solution (red) and a small droplet is formed. This second pipet is moved toward the receiving droplet. (B,iv) Upon contact between the receiving droplet and the injection droplet, the contents are rapidly mixed. (C) A bright field image of a receiving droplet sitting on the surface of nanoporous gold with an injection droplet nearby. The receiving droplet is weakly attached to the surface as evidenced by the small contact area highlighted with the yellow ellipse near the center of the droplet.85

Figure 4.2. Schematic representation of (A) glass functionalization using (3-mercaptopropyl) trimethoxysilane (MPTMS) in hexanes for 1 hour in a 60°C water bath and (B) preparation of nanoporous gold (NPG) via dealloying in concentrated nitric acid for 13 minutes, rinsing with DI water, and capture of dealloyed square on copper fitted functionalized glass slide.87

Figure 4.3. Reprinted with permission from reference 1. American Chemical Society Copyright 2016. Bright field optical microscopy images of receiving droplets on the surface of a modified nanoporous gold electrode. The desired shape of the droplet is apparent during the first ~ 20 s and begins to degrade around 90 s leading to complete loss of the droplet at 150 s. The droplet diameter in the $t = 20$ s image is ca. 90 μm88

Figure 4.4. Cartoon representation of fabricated microdroplet electrode using Kwikcast to secure NPG electrode to another glass slide with 1 cm hole, modification of NPG surface with 1-hexanethiol, and placement of hexadecane in the well created.89

Figure 4.5. Reprinted with permission from reference 1. American Chemical Society Copyright 2016. OCP–time trace for (a) the addition of 5 mM potassium ferrocyanide to a receiving droplet containing 0.5 mM potassium ferricyanide and (b) the addition of 50 mM potassium ferrocyanide to a receiving droplet containing 5 mM potassium ferricyanide. With each addition, the voltage quickly changes and equilibrates. The red portion of both curves is a least-square fit to the data with a single exponential function with time constant $\tau = 302.1 \pm 0.2$ ms (a) and $\tau = 200.4 \pm 0.1$ ms (b). (c) The small droplets enable measurement of rapid kinetics. This is verified by comparing the time constant of the change in voltage for the droplet system (blue trace, $\tau = (0.51 \pm 0.01)$ s) and a large bulk electrode with a geometric area of 0.079 cm^2 in 17.1 mL of solution (red trace, $\tau = (4.1 \pm 0.3)$ s).....92

Figure 4.6. Reprinted with permission from reference 1. American Chemical Society Copyright 2016. Nernst plot for (a) potassium ferrocyanide ($[\text{Fe}(\text{CN})_6]^{4-}$) and ferricyanide ($[\text{Fe}(\text{CN})_6]^{3-}$) with receiving droplets of 290, 470, and 620 pL represented by red circles (red ●), blue circles (blue ●), and black triangles (▼), respectively. (b) Ferrous (Fe^{2+}) and ferric (Fe^{3+}) ammonium sulfate with receiving droplets of 590, 290, and 640 pL represented by the red circles (red ●), blue circles (blue ●), and black triangles (▼), respectively, and (c) hydroquinone (HQ) and benzoquinone (BQ) with receiving droplets of 1000 pL for both run 1 (red circles, red ●) and run 2 (blue circles, blue ●). The solid line represents the linear regression fit to the data (solid points).95

Figure 4.7. Reprinted with permission from reference 1. American Chemical Society Copyright 2016. Nernst plot for (a) potassium ferrocyanide ($[\text{Fe}(\text{CN})_6]^{4-}$) and ferricyanide ($[\text{Fe}(\text{CN})_6]^{3-}$) with receiving droplets of 290, 470, and 620 pL represented by red circles (red ●), blue circles (blue ●), and black triangles (▼), respectively. (b) Ferrous (Fe^{2+}) and ferric (Fe^{3+}) ammonium sulfate with receiving droplets of 590, 290, and 640 pL represented by the red circles (red ●), blue circles (blue ●), and black triangles (▼), respectively, and (c) hydroquinone (HQ) and benzoquinone (BQ) with receiving droplets of 1000 pL for both run 1 (red circles, red ●) and run 2 (blue circles, blue ●). The solid line represents the linear regression fit to the data (solid points).98

Chapter 5

Figure 5.1. Optical images of electrochemical cell showing mNPG as working electrode and bare Ag/AgCl wire as reference electrode in a cut 1.5 mL centrifuge tube. All electrochemical measurements were conducted in a solution volume of 100 μL110

Figure 5.2. (a) Open-circuit potential (OCP) time trace of the additions of ferrocyanide to a ferricyanide receiving solution using a mini-nanoporous gold (mNPG) electrode. (b) Nernst plot constructed from time traces such as that shown in (a). Each symbol represents a separate experiment using a different mNPG electrode. A slope of -58.3 mV was obtained with a y-intercept of 146.0 mV. Correlation coefficient = 0.9965.....112

Figure 5.3. Open-circuit potential (OCP) time traces for the addition of aliquots of (a) ascorbic acid (AA) every 100 seconds, (b) cysteine (Cys) every 200 seconds, and (c) uric acid (UA) every 100 seconds, respectively, to a 100 μL solution of 0.1 M PBS (0.1 M KCl as electrolyte, pH = 7.4) following an initial wait time of 100 seconds. Potential was measured using a mini-nanoporous gold (mNPG) electrode as the working electrode and Ag/AgCl as the reference electrode.114

Figure 5.4. Nernst plots constructed using time trace and concentrations of (a) ascorbic acid, (b) cysteine, and (c) uric acid. The solid line represents a linear least squares regression analysis of three different data sets (represented as different symbols). The slope for each line is shown and all had correlation coefficients > 0.99.116

Figure 5.5. OCP time-traces showing little to no response to additions of (a) glucose and (b) hydrogen peroxide to 100 μL of 0.1 M PBS receiving solution. Breaks in the trace indicate the addition of the redox molecule of interest.120

Figure 5.6. SEM images of (A-C) mNPG and (D-F) mNPG-Pt surfaces at increasing magnifications. Pores range from 5 to 20 nm.123

Figure 5.7. Cyclic voltammograms of a NPG electrode before (dashed -) and after (solid -) platinum deposition using a potential window of -0.4 to 1.4 V, in 0.5 M H_2SO_4 at a scan rate 100 mV/s. The gold oxide reduction peak at 0.5 V decreases and the hydrogen desorption peak of platinum at -0.1 V appears following deposition.124

Figure 5.8. XPS spectra of NPG without platinum deposition showing (a) Au 4f 5/2 and 7/2 peaks at 87.3 and 83.6 eV, respectively, (b) Ag 3d 3/2 and 5/2 at 373.9 and 367.9 eV, respectively, and (c) lack of Pt 4f 5/2 and 7/2 peaks. Following the deposition of platinum into the NPG framework (d) Au 4f 5/2 and 7/2 peaks at 87.9 and 84.2 eV, respectively, (e) Ag 3d 3/2 and 5/2 at 374.2 and 368.2 eV, respectively, and (f) presence of Pt 4f 5/2 and 7/2 peaks at 74.7 and 71.5 eV, respectively. Raw data shown. Binding energies were normalized using obtained C1s peak (not shown). Composition of NPG and NPG-Pt were calculated as $\text{Au}_{0.839}$, $\text{Ag}_{0.161}$, $\text{Pt}_{0.0}$ and $\text{Au}_{0.793}$, $\text{Ag}_{0.164}$, $\text{Pt}_{0.043}$, respectively.127

Figure 5.9. Open-circuit potential (OCP) time traces for the addition of aliquots of (a) ferrocyanide every 100 seconds to a receiving solution of ferricyanide in 0.1 M PBS as well as the time-traces for (b) ascorbic acid (AA) every 100 seconds, (c) cysteine (Cys) every 200 seconds, and (d) uric acid (UA) every 200 seconds, respectively, to a 100 μL solution of 0.1 M PBS (0.1 M KCl as electrolyte, pH = 7.4) following an initial wait time of 100 seconds. Potential was measured using a Pt-speckled mini-nanoporous gold (mNPG-Pt) electrode as the working electrode and Ag/AgCl as the reference electrode.129

Figure 5.10. Nernst plots comparing the response of mNPG-Pt (blue) and mNPG (red) electrodes to the addition of (a) ferrocyanide to ferricyanide in 0.1 M PBS and the addition of (b) ascorbic acid, (c) cysteine, and (d) uric acid to 0.1 M PBS, respectively. All equations show the calculated slopes and y-intercepts of each plot with correlation coefficients all >0.99. Different shapes of each color represent a separate set of data.130

Figure 5.11. Open-circuit potential (OCP) time-traces showing a characteristic stair-step with additions of (a) glucose every 200 seconds (after an initial wait time of 100 seconds) or (b) hydrogen peroxide (after a 100 second initial wait time) with difference in time between the first and second addition was 200 seconds and subsequent addition was every 100 seconds to separate 100 μL initial receiving solutions of 0.1 M PBS (0.1 M KCl as electrolyte pH = 7.4). ...131

Figure 5.12. Nernst plots showing the response of mNPG-Pt electrodes to the addition of (a) glucose and (b) hydrogen peroxide. The solid line represents a linear least squares regression

analysis of different data sets (represented as different symbols). The slope for each line is shown and all had correlation coefficients > 0.99131

Figure 5.13. Open-circuit potential (OCP) time traces for the addition of aliquots of cysteine (Cys) in 0.1 PBS solution containing 50 μM AA and 300 μM UA to an initial receiving solution of 0.1 M PBS also containing 50 μM AA and 300 μM UA. The time-traces were obtained simultaneously using (a) mNPG and (b) mNPG-Pt electrodes. The first addition of cysteine occurred at ~ 5 seconds causing a large drop in initial potential.132

Figure 5.14. Nernst plot showing the response of mNPG-Pt (**blue**) and mNPG (**red**) electrodes to the addition of cysteine to 0.1 M PBS containing physiological concentrations of ascorbic acid (50 μM) and uric acid (300 μM). Potential measurements were obtained simultaneously.133

Chapter 6

Figure 6.1. Illustrated representation of a fuel cell with a platinum-speckled nanoporous gold (NPG-Pt) anode, traditional platinum cathode, and acidic media as the electrolyte. Fuel is oxidized at the anode to form protons and electrons, protons diffuse across the electrolyte to the cathode where, in the presence of oxygen, protons are reduced to water.139

Figure 6.2. Cyclic voltammogram of methanol oxidation using NPG (**red**) commercial platinum (**black**) and NPG-Pt (**blue**) electrodes all at 1 M concentration in 0.5 M H_2SO_4 . Potential window of -0.1 to 0.7 V, scan rate 50 mV/s.144

Figure 6.3. Cyclic voltammogram of ethanol oxidation peaks using NPG (**red**) commercial platinum (**black**) and NPG-Pt (**blue**) electrodes all at 1 M concentration in 0.5 M H_2SO_4 . Potential window of -0.2 to 1.2 V, scan rate 50 mV/s.145

Figure 6.4. CV overlay of formic acid oxidation peaks using commercial platinum (dashed) and NPG-Pt (solid) electrodes in 0.5 M H_2SO_4 . Potential window of -0.4 to 1.0 V, scan rate 50 mV/s146

List of Tables

Chapter 6

| | |
|---|-----|
| Table 6.1. Comparison of electrooxidative current densities of platinum-speckled mini-nanoporous gold (mNPG-Pt), mini-nanoporous gold (mNPG), and planar platinum (Pt) electrodes in presence of different fuels in 0.5 M H ₂ SO ₄ | 147 |
|---|-----|

List of Abbreviations

| | |
|--------------------------------------|------------------------------------|
| NPG: | nanoporous gold |
| mNPG: | mini-nanoporous gold |
| NaCl: | sodium chloride |
| Au: | gold |
| Ag: | silver |
| Pt: | platinum |
| Si: | silicon |
| Ni: | nickel |
| Cu: | copper |
| Al: | aluminum |
| Zn: | zinc |
| MPTMS: | (3-mercaptopropyl)trimethoxysilane |
| PSI: | photosystem I |
| TPDA: | terephthalaldehyde |
| SH: | thiol |
| μ TAC: | micro total analysis system |
| PDMS: | polydimethylsiloxane |
| IDA: | interdigitated array |
| Fc: | ferrocene |
| $\text{K}_4\text{Fe}(\text{CN})_6$: | potassium ferrocyanide |

| | |
|---------------------------------|--|
| Ru: | ruthenium |
| Rh: | rhodium |
| Pd: | palladium |
| Os: | osmium |
| Ir: | iridium |
| DAFC: | direct alcohol fuel cell |
| SAM: | self-assembled monolayer |
| H ₂ O ₂ : | hydrogen peroxide |
| HRP: | horse radish peroxidase |
| DNA: | deoxyribonucleic acid |
| ssDNA: | single-stranded DNA |
| AA: | ascorbic acid |
| OH: | hydroxyl |
| H ⁺ : | proton |
| Cys: | cysteine |
| GSH: | glutathione |
| CySS: | cystine |
| ATP: | adenosine triphosphate |
| NADH: | nicotinamide adenine dinucleotide |
| ROS: | radical oxygen species |
| PEMFC: | polymer electrolyte membrane fuel cell |
| AFC: | alkaline fuel cell |
| PAFC: | phosphoric acid fuel cell |
| MCFC: | molten carbonate fuel cell |
| SOFC: | solid oxide fuel cell |

| | |
|-----------------------|---|
| MEA: | membrane electrode assembly |
| DOE: | Department of Energy |
| KOH: | potassium hydroxide |
| DMFC: | direct methanol fuel cell |
| CO ₂ : | carbon dioxide |
| CO: | carbon monoxide |
| H ₂ O: | water |
| CH ₃ COOH: | acetic acid |
| WE: | working electrode |
| RE: | reference electrode |
| AE: | auxiliary electrode |
| CV: | cyclic voltammetry (or voltammogram) |
| OCP: | open-circuit potential |
| SEM: | scanning electron microscopy |
| BSE: | back-scattered electrons |
| SE: | secondary electrons |
| PMT: | photomultiplier tube |
| EDS: | energy-dispersive X-ray spectroscopy |
| XPS: | X-ray photoelectron spectroscopy |
| Al K α : | monochromatic x-rays |
| CHA: | concentric hemispherical electron energy analyzer |
| RSF: | relative sensitivity factor |
| PG: | planar gold |
| KCl: | potassium chloride |
| PBS: | phosphate buffered saline |

| | |
|-----------------------------------|-----------------------------------|
| $[\text{Fe}(\text{CN})_6]^{3-}$: | ferricyanide |
| AgCl: | silver chloride |
| $[\text{Fe}(\text{CN})_6]^{4-}$: | ferrocyanide |
| VCU: | Virginia Commonwealth University |
| e^- : | electron |
| ORP: | oxidation-reduction potential |
| HQ: | hydroquinone |
| BQ: | benzoquinone |
| H_2SO_4 : | sulfuric acid |
| K_2PtCl_4 : | potassium tetrachloroplatinate |
| mNPG-Pt: | platinum-speckled nanoporous gold |
| EASA: | electroactive surface area |

| | |
|-----------------|--------------------------|
| E_i : | initial potential |
| E_f : | final potential |
| I_c : | charging current |
| ν : | scan rate |
| C_{dl} : | double layer capacitance |
| A: | area |
| E_{peak} : | peak potential |
| E_m : | measured potential |
| E_{ind} : | indicating electrode |
| E_{ref} : | reference electrode |
| $E_{binding}$: | binding energy |

| | |
|------------------------|-----------------------------------|
| E_{photon} : | incident photon |
| E_{kinetic} : | kinetic energy |
| W : | work function |
| E^0 : | standard reduction potential |
| R : | gas constant |
| T : | temperature in kelvin |
| n : | number of electrons |
| C_{Red} : | concentration of reduced species |
| C_{Ox} : | concentration of oxidized species |

Abstract

Biosensing and Catalysis Applications of Nanoporous Gold (NPG) and Platinum-Speckled Nanoporous Gold (NPG-Pt) Electrodes

by Christopher James Freeman

A dissertation in partial fulfillment of the requirements for the degree of Doctor of Philosophy at
Virginia Commonwealth University

Director: Dr. Maryanne M. Collinson

Professor of Chemistry

Virginia Commonwealth University, 2018

The importance of porous materials has risen substantially in the last few decades due to their ability to reduce the size and cost of bioanalytical devices and fuel cells. First, this work aims to describe the fabrication of nanoporous gold (NPG) electrodes that are resistant to electrode passivation due to fibrinogen biofouling in redox solutions. The effect on potentiometric and voltammetric experiments was seen as a deviation from ideal behavior on planar gold electrodes, whereas NPG electrodes were consistently behaving in a Nernstian fashion at low concentrations of ferri-ferrocyanide ($\leq 100 \mu\text{M}$). An improvement in electrode

behavior on NPG electrodes versus planar gold was seen in solutions containing ascorbic acid as well as blood plasma. Second, cost effective NPG electrodes were fabricated using a glass substrate to test the response in the presence of a variety of redox molecules. The optical transparency of these electrodes allowed for microdroplet measurements to be made using an inverted microscope in several redox solutions for validation and subsequent biological applicability. Nernstian behavior was demonstrated for all one- and two-electron transfer systems in both poised and unpoised solutions. All experiments were conducted using volumes between 280 and 1400 pL producing rapid results in less than one minute. Third, in order to decrease the requirement for complex instrumentation, microdroplet fabrication technique was used to create mini-nanoporous gold (mNPG) electrodes on glass capillary tubes. The cylindrical shape of the electrodes allowed for testing in sample volumes of 100 μ L. The response to ferri-ferrocyanide, ascorbic acid, cysteine, and uric acid was then investigated with Nernstian behavior shown. However, the mNPG electrodes were insensitive to glucose and hydrogen peroxide. In order to increase the sensitivity of the electrodes, a minimal amount of platinum was electrodeposited onto the NPG surface using a low concentration of platinum salt (0.75 mM) for a short deposition time (2 seconds) producing a Nernstian response to both glucose and hydrogen peroxide. Lastly, to test the viability of crossover applications, the platinum incorporated NPG electrode was employed as a fuel cell anode material, testing their oxidation capability with methanol, ethanol, and formic acid.

Chapter 1

Introduction

1.1. Introduction

Electrochemistry principles and practices have become a critical part of a growing scientific and technological movement to fabricate and implement specialized devices in fields such as medicine¹⁻⁴, the automotive industry^{5,6}, electronics^{7,8}, forensics⁹, and sensors¹⁰⁻¹³, to name a few. Electrochemistry is a diverse and dynamic field, which investigates electrochemical processes through the movement of electrons and the electrical and chemical changes created by the passage of current.¹⁴ The incorporation of nanomaterials has provided a larger surface area which allows for an increase in available sites for electron transfer.¹⁵⁻¹⁷ The intrinsic nature of porous materials used in electroanalytical measurements have allowed for testing without the need for sample pretreatment or dilution as well as the fabrication of more robust electrodes that are resistant to contamination.^{15,18-21} The fabrication of an electrode material can be exploited in a number of different applications including biosensing²²⁻²⁵ and energy conversion and storage.^{5,26-28}

The demand for smaller and smaller devices, which maintain the efficiency, effectiveness, and lifespan, at a similar or lower cost, is fueling a specialized subset of electrochemistry, aptly referred to as microelectrochemistry or microscopic electrochemistry. This field utilizes the fabrication of conductive materials with a very high surface area to geometric area ratio allowing measurements to take place using a very small volume.

Advances in the fields of biosensors and biotechnology have led to great improvements in real-time environmental monitoring and medical on-site and field testing, focusing on developing sensors for point-of-care.²⁹ The benefits of miniaturization have been realized with a drastic decrease in sample volume needed that can significantly decrease analysis time and allow

access to constrained areas.^{12,18,30-33} For example, environmental samples collected from groundwater, rivers, lakes, and oceans as well as water samples from treatment facilities have been studied to measure analyte concentration, including contaminants, which has promoted a shift towards real-time sampling and evaluation.³⁴⁻³⁶ The effects of contaminants on an aquatic environment can be catastrophic for wildlife as well as individuals living near the affected area.³⁷ Also, using minimal sample volumes can decrease the risk posed to patient health, especially at-risk individuals such as heart patients and infants. Given the stress currently on the bodies of these patients, additional blood samples could do far greater harm than good or may not be able to be obtained safely. The benefits of rapid sample testing coupled with minimal environmental or biological impact show the need to miniaturize electrochemical biosensors. Possible fabrication of these biosensors must begin with the selection of an appropriate material that is low-cost, responds to a number of redox molecules, and provides a large surface area.

Nanofabrication utilizes and assembles materials on an atomic scale, thus rendering electrodes with a size and shape to permit usage in and for sensitive and selective situations and environments.³⁸ Because of this specialization, function becomes a deciding factor when fabricating and constructing an electrode, especially in cases where sample sizes are limited and/or are very small. This is where porous materials play an important role in electrode and device fabrication. This chapter will focus on nanoporous gold electrodes, including information on how they are fabricated, the benefits of fabrication techniques, surface modification, and the various applications of these electrodes.

1.2. Nanoporous Gold (NPG) Electrodes

Nanoporous gold (NPG) is a valuable electrode material because it has a large surface area with respect to its geometric area. Nanoporous gold, unlike bulk gold, consists of a 3D-bicontinuous framework comprised interconnected pores and ligaments. The pores can range in sizes from 2 to 100, and the surface area can be 2-1000 times larger than planar gold.^{39,40-42} The distribution and organization of the pores are what distinguish nanoporous gold from planar, electrodeposited, macroporous, and hierarchical porous gold.^{40,43} This structure has been shown to change the reactivity of gold due to the strain put onto the gold at the atomic level.⁴⁴ Since bulk gold does not adsorb hydrogen or oxygen, to a large extent, at standard temperature⁴⁵ it is said to be chemically inert. The areas of the porous structure that allow this to become more active are those where the gold is less coordinated to other gold atoms.

The unique structure of nanoporous gold (NPG) has been shown to be an advantage in many applications.⁴⁰⁻⁴² Having a highly conductive and biocompatible porous network allows for numerous applications in biological sensing applications. In addition, the ability of the surface to be modified increases its usefulness in applications such as biosensing.^{33,46,47} High surface area to volume ratio allows for the fabrication of very small electrodes as well as the creation of small chip-size designs.⁴⁸ Also, in addition to small-scale fabrication, the inherent structure of the NPG allows a bioseiving effect to take place. Gold electrode surfaces can become passivated in biological solutions containing proteins. Proteins, like albumin and fibrinogen, adsorb to the electrode surface and reduce the exposed area that can transfer electrons. The more the surface is coated, the more interference with electron transfer and a substantial decrease in signal response. This behavior is known as biofouling and is the case of electrode failure when used in biological

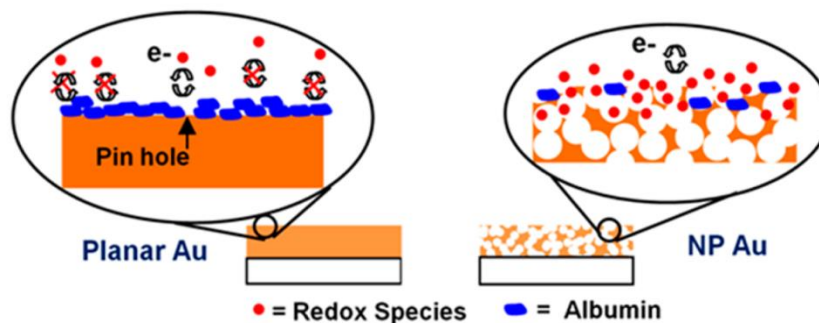


Figure 1.1. Simplified graphical representation of the surface of nanoporous gold and planar gold in the presence of albumin and a small redox molecule in solution. Electron transfer is hindered at planar gold but not at nanoporous gold. Reprinted with permission from ref. 43.

media.¹⁹ Due to the small pores, small redox active molecules can diffuse into the structure while larger biofouling agents adhere to the surface enhancing the electrochemical activity of NPG electrodes versus planar gold as seen in **Figure 1.1**.⁴³ As the protein albumin binds to the electrode surface, the electroactive area in planar gold electrodes is reduced significantly, whereas the pores in NPG are still available for redox molecules to interact.

1.2.1. Fabrication Methods

The distribution and sizes of pores and ligaments of nanoporous gold strongly depends on the fabrication method used. Nanoporous gold electrode fabrication falls under these general methods: bottom-up and top-down or a combination of both.⁴⁹ **Figure 1.2** shows a schematic representation of electrochemical bottom-up (b), top-down (a), and a combination of both (c and c') to form nanoporous gold electrodes.⁴⁹ Bottom-up involves the building of a material starting at the substrate forming a monolayer or series of monolayers to create a porous structure. A template can allow for the fabrication of ordered pore structure or nanoparticles can be deposited

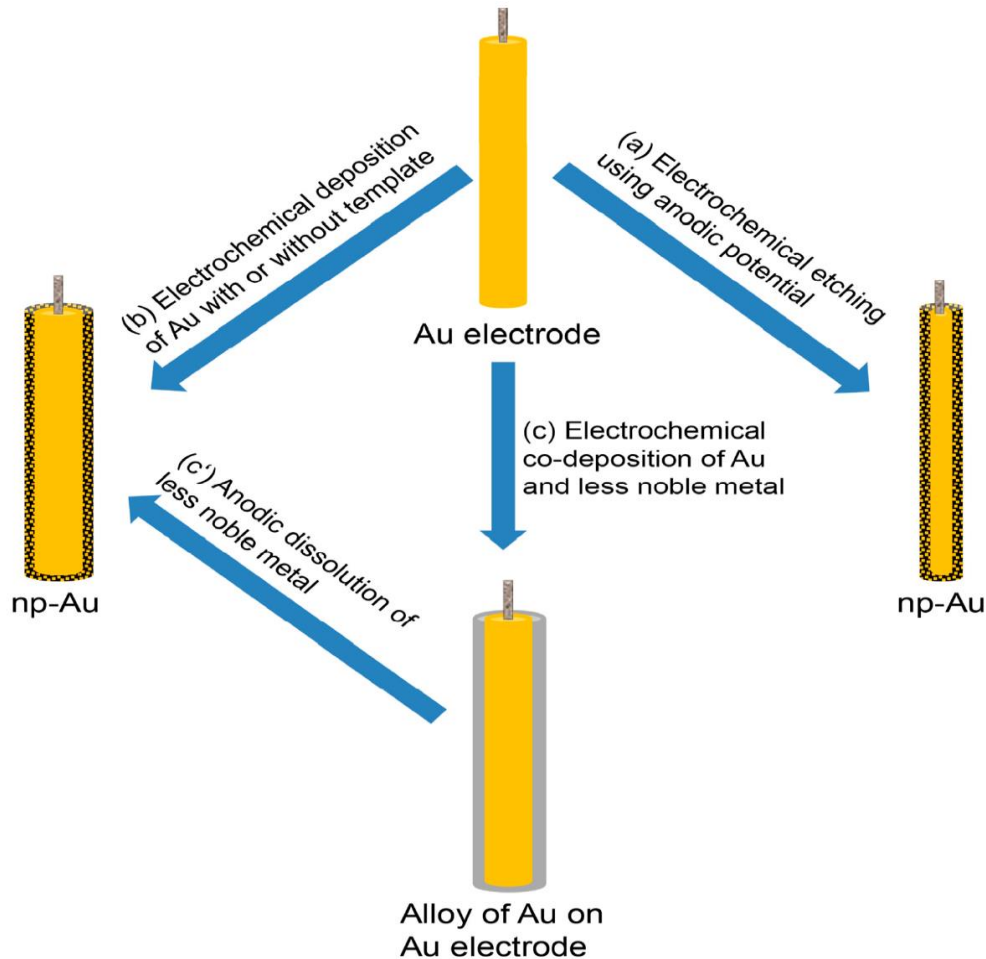


Figure 1.2. Different electrochemical approaches for the preparation of nanoporous gold (NPG) electrode on gold support: (a) top-down, (b) bottom-up, and (c and c') combination of both bottom-up and top-down approaches. Adopted from ref. 49.

onto a substrate. An example involves polystyrene spheres that are coated onto a substrate, usually bulk gold. Gold is then electrodeposited onto the empty spaces and the spheres are removed. This allows for the organized control of pore size, as the pores formed are the size of the immobilized spheres.⁵⁰ Top-down fabrication involves the destruction or dissolution of a material in order to form the desired structure.⁵¹ Electrochemical etching has been shown to produce porous materials when used in creating porous aluminum and semiconductors.^{52,53}

The higher cost of bulk gold has pushed scientists toward using gold-metal alloys. The process of removing the lesser metal leaving a framework of pores and ligaments has allowed for the fabrication of nanoporous metals. Dealloying can be accomplished either electrochemically or chemically. Electrochemical dealloying, similar to etching, uses an applied potential to remove the lesser metal from the Au alloy. NPG films were synthesized via the dealloying of Al-Au films using a sodium chloride solution (10 wt.% NaCl) and held the potential at 1.5 V to leach the aluminum.⁵⁴ Increasing the composition of aluminum increased the porous nature of the gold films. Also, Au-Ni alloy films were used to prepare NPG with the dissolution of Ni at potentials of 1.0, 1.3 and 1.5 V, respectively.⁵⁵ Electrochemical dealloying has been shown to produce porous gold materials using Ag-Au, Cu-Au, Al-Au, and Au-Zn.^{38,56,57}

Alternatively, chemical dealloying removes the need for an electrochemical setup where an acid selectively dissolves the unwanted metal. For the purposes of this work, the focus will be on dealloying a Au-Ag alloy. It was believed originally that the process of dealloying simply revealed an underlying structure of the more noble gold by dissolving undesired silver. Instead, dealloying is a dynamic process that involves not only the dissolution of Ag, but also the diffusion and aggregation of gold atoms. Exposing concentrated acid to the alloy begins the process of Ag dissolution. If dealloying simply removed the Ag, then after period of time, all the silver in the top most layers would be dissolved and the underlying alloy would be covered by inert gold inhibiting further dealloying.⁵⁶⁻⁵⁸ Thus, the pores and ligaments formed are due to interactions between the alloy surface and acid interface. First, Ag atoms are dissolved by the acid and as more Ag dissolves, the more susceptible other neighboring Ag atoms due to a reduction in coordination as well as surface exposure. The remaining Au atoms are also less coordinated and therefore, unstable. Instead of remaining in their post-dissolution orientation, the

Au atoms diffuse and aggregate forming more stable islands. The agglomeration of Au atoms in turn reveals a layer of alloy, which is then exposed to acid and the process continues where Ag is dissolved and Au atoms diffuse to the islands. The initial distances between islands represents a very close adherence to the ligaments seen after dealloying is stopped.^{59,60} This process reinforces the findings that an increase in the dealloying time not only increases the pore and ligament size, but also decreases the structural stability of the 3D framework. Floating the Au-Ag alloy on concentrated acid for 5 minutes up to 5 days can provide pore sizes in the range of 5-200 nm. The longer the dealloying time or larger initial Ag content of the alloy will cause larger pore sizes.^{42,43,60-62} Another route utilized a longer dealloying time, but with diluted nitric acid to slow the dealloying process.⁶³

Dealloying binary Au-Ag alloys has been the traditional chemical route of preparing NPG. The introduction of a third metal in the initial alloy has been investigated as a route to increase electrode activity. Ternary Ag-Au-Pt alloys can be obtained commercially (via cold rolling)⁶⁴ or through the vapor deposition of different compositions of the three metals.⁶⁵ The selective dissolution of Ag, as described above, results in porous framework of Au and Pt.^{64,66,67} The downside of this technique stems from the increased cost of platinum that is distributed within the framework and not actively used in sensing or catalysis. Additionally, an increase in dealloying time, used to expose the limited amount of Pt and increase reactivity, will reduce the integrity of the framework. Due to the somewhat fragile nature of dealloyed gold, it is important to attach the gold to a solid support.

1.2.2. Nanoporous gold substrates

Gold is a common substrate for the fabrication of NPG. Several methods describe the use of a solid gold substrate. A gold wire^{68,69} or gold vapor deposited onto an additional support like titanium and/or glass. Alternatively, a thin layer of gold can be sputter or vapor deposited onto a less costly support, usually titanium coated glass. The substrate itself can be the electrode as described previously in the etching of the bulk gold. In addition, due to gold-gold interactions, dealloyed gold can be captured directly on the surface. Glassy carbon however, does not directly bind gold it is not an ideal substrate material unless the surface is modified. The use of thiol containing benzene, mercaptobenzene, has been used as an anchor for gold nanoparticles. The benzene is electrografted onto the glassy carbon surface leaving a monolayer of available thiol (-SH) groups for the gold to attach.⁷⁰ Silicon was used as the substrate and a Ag-Au alloy was placed on the surface using electron beam evaporation⁷¹ as well as through direct current sputtering using chromium as an adhesion layer.⁴⁸

In an effort to reduce the cost of electrode fabrication, glass substrates have been a recent focus of NPG electrode fabrication. Glass is inexpensive compared to gold-coated slides and is common in most laboratories. The main deterrent to using glass as a gold electrode substrate stems from the inability of glass to bind gold, so directly placing NPG on the surface will not result in a stable electrode. It is possible to sputter coat a glass slide with a Au-alloy (Ag, Si, etc.) and proceed to dealloy,^{72,73} thus reducing production costs. However, control over deposition is limited as the alloy is vaporized or sputtered onto the entire glass slide. An alternative to sputter coating or vapor deposition involves the functionalization of the glass with a thiol silane, like (3-mercaptopropyl) trimethoxysilane (MPTMS).⁷⁴⁻⁷⁷ Ciesielski and coworkers demonstrated the immobilization of photosystem I (PSI) onto the surface of a dealloyed gold leaf electrode to

convert solar power into usable energy. Electrodes were fabricated using gold leaf exposed to concentrated nitric acid at different times from 15 minutes to 24 hours. The gold surface was modified with 2-aminoethanethiol as an anchor and terephthalaldehyde (TPDA) as a linker to bind PSI.⁷⁸ The NPG was captured on a Au-Si substrate and photocurrent responses were measured. Interestingly, in order to determine the coverage of the anchor-linker on the NPG surface, a non-conductive substrate was required. This group chose to functionalize the glass with 3-mercaptopropyl trimethoxysilane (MPTMS). The glass is coated with a layer of the silane, which, due to its methoxy groups, reacts with the –OH groups on the surface of the glass forming a layer on the surface. This anchor contains a thiol group (-SH) which forms a Au-S bond, chemically attaching the NPG to the glass surface.⁷⁸ Even though the glass substrate was not used in the photocurrent measurements, it presented a possible avenue for the fabrication of NPG electrodes on a very inexpensive and commonly available substrate.

1.3. Small Volume Electrochemical Measurements

The term miniaturization in electrochemistry refers to the decrease in electrode size, scale, or the amount of sample used. The importance of miniaturization stems from the need for rapid testing and the desire to use a minimal amount of sample. Measurement in small volumes allow for rapid testing, possible complexing with other instrumentation, and the push to move to lab-on-chip style designs where an entire electrochemical setup is contained on a chip no larger than a microscope slide.

1.3.1. Microvials

A method of controlling the volume of sample solution involved the control of the space available for a sample to be placed. Using glass capillary tubes two groups formed microvials

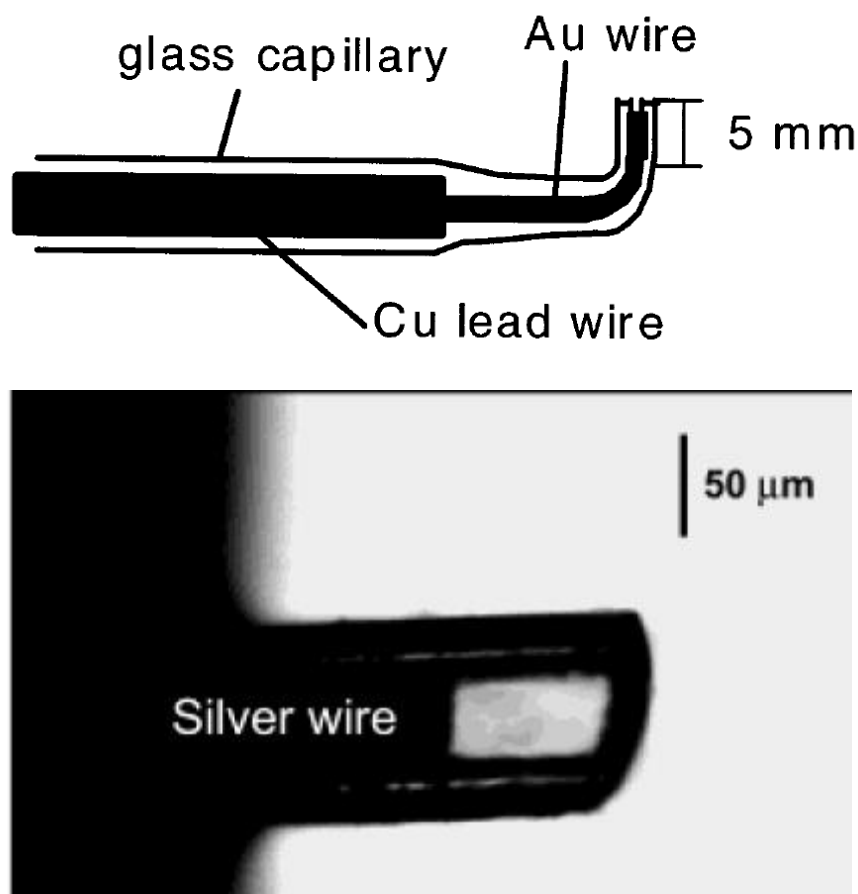


Figure 1.3. (a) Cartoon representation of a fabricated microvial from a glass capillary and gold wire working electrode. Adapted from ref. 79 (b) top-view optical image of a glass capillary microvial fabricated using chloridized silver wire. Adapted from ref. 80

that contained 100-200 pL of sample. Both methods involved the use of capillary tubes where an electrode (working or reference electrode) was inserted into one end and the space left empty formed the vial.^{79,80} **Figure 1.3** shows the fabricated microvials. The volume of each vial can vary depending on electrode placement. Vial volume was calculated using the inner diameter and length of the empty tube. In order to prevent evaporation, the cell was covered with mineral oil creating a hydrophobic environment. The transport of hydrogen peroxide out of or dopamine in to a single cell was investigated. An additional method involved the lithographic production of microvials onto a polystyrene substrate. Volumes as low as 14 pL were used to conduct voltammetric measurements with ferrocenecarboxylic acid in phosphate buffer.⁸¹

1.3.2. Stationary Drops

Small volume measurements have been done using single drop samples. Work has been done to sandwich a sample between an electrode and a hydrophobic substrate in order to maintain the integrity of the drop shape maximizing exposure to the electrode. Multiple Au wire electrodes were packed in an epoxy resin and a membrane containing a reference material was placed on the end. A single drop of sample was placed on a glass microscope slide which is attracted to the slide, trapping the drop between the slide and the electrodes (**Fig. 1.4**).⁸² The

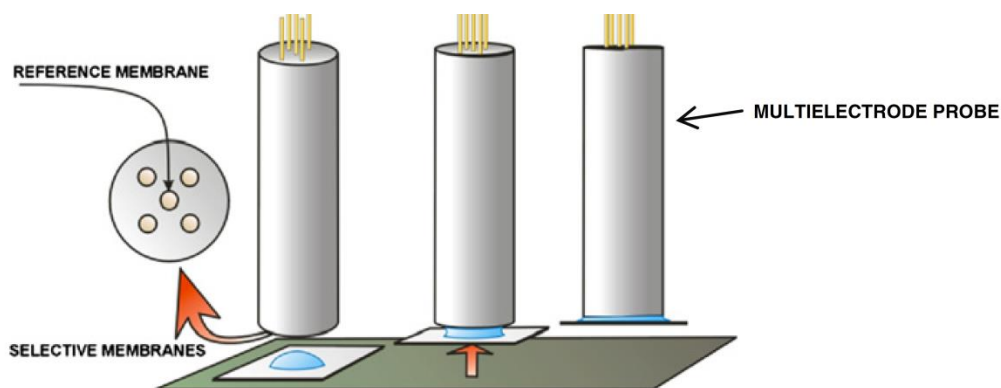


Figure. 1.4. Cartoon representation of a single drop measurement using multiple gold electrodes, a reference membrane, and sample on a glass microscope slide. Reprinted with permission from ref. 82.

contact between the electrodes and the drop are essential in reducing evaporation. This technique allows for the potentiometric measurement of a very small sample volume, but does not allow for the addition of additional solution given the confinements of the electrochemical setup.

1.3.3. Lab-on-Chip Design and Flow Cells

Lab-on-chip or micro total analysis system (μ TAC) designs seek out to take lab scale measurements and move all of the complex methods into small, integrated devices. These designs can use a variety of different substrates including glass, paper, polymers, quartz, metals,

polydimethylsiloxane (PDMS) and silicon.⁸³ The primary components of a chip involve the flow of a sample or solution, a material that is active for a test or measurement to take place, a power source, and some method of data output.²² Smaller devices lead to lower costs, smaller volumes, less energy required to power devices, and decreased analysis time. Current commercially available chips have been developed to quantify cardiac biomarkers, clotting factors, proteins, blood gases, and salt concentration.²² The most commonly known form of chips are used to identify pregnancy.⁸⁴

The push for real-time testing has allowed for vast improvements over the past few decades with the development and implementation of flow cells. Flow cells are machined chips that contain a series of channels allowing for the constant stream of solution. A sample is then injected and interacts when in contact with an electrode fabricated on or into one of the channels. A downside to flow cells results in the need for additional instrumentation such as a pump to keep the solution flowing. Electrodes have been fabricated in an interdigitated array (IDA) platform where a series of electrodes are placed next to each other where a redox-cycling mediator can amplify the signal.⁸⁵⁻⁸⁷ The array is constructed using a lithographic technique and ferrocene (Fc) is used the mediator. As oxidation occurs at one electrode, and an adjacent electrode, with an opposite set potential, can reduce the aforementioned oxidized species. This allows a large signal to be obtained using very small concentrations of the redox molecule as well as rapid detection. When coupled to a flow cell, a large response can be seen as soon as an injected sample reached the electrode array. An example of an IDA incorporated into a microfluidic device is shown in **Figure 1.5**, where a simplified schematic (A) shows flow through the device interacting with four separate gold electrodes. These devices are fabricated using polycarbonate slices heat-sealed onto four separate Au electrodes to create the fluid

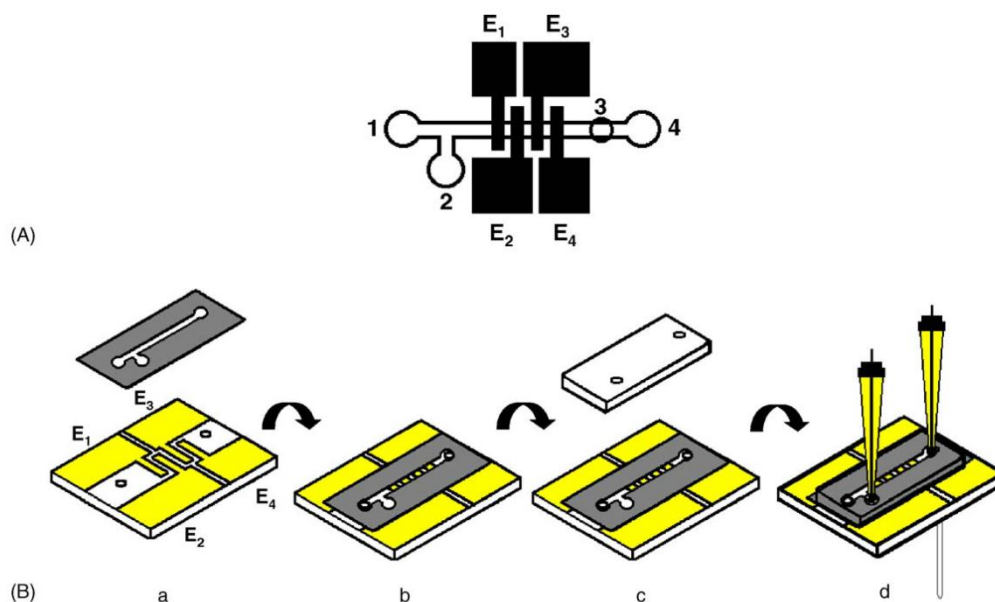


Figure. 1.5. Sketches of the construction of individually driven interdigitated gold electrodes and IDA gold electrodes assembled into microfluidic cells. (A) Top schematic view of the microfluidic device. (1) Inlet; (2) reference electrode, located next to inlet to the cell; (3) reference electrode, located next to outlet to the cell; (4) outlet and auxiliary electrode; (E_1 – E_4) working electrodes. (B) Schematic illustration of the construction of a microfluidic cell with four individually driven gold electrodes. (a) Polycarbonate slice with finished Au working electrodes (E_1 – E_4) and orifices for flow inlet and outlet, and toner mask of channels (wax paper not shown) before application; (b) same components of (a) after heat-transfer of toner channel; (c) microfluidic flow cell before heat-sealing of the second polycarbonate slice; (d) complete microfluidic cell with two attached miniaturized Ag/AgCl reference electrodes. Adapted from ref. 87.

channel. A second polycarbonate slice is then heat-sealed to provide a dock for the reference Ag/AgCl electrode.⁸⁷ Devices were characterized using potassium ferrocyanide ($K_4Fe(CN)_6$) using cyclic voltammetry and chronoamperometry (techniques described in more detail in Ch. 2) showing ideal electrode behavior. Using previously described methods of NPG fabrication and coupling device fabrication procedures can provide a multitude of devices that have larger signal responses due to vastly increased electroactive surface area.

1.3.4. Miniaturized Electrodes

Instead of using a substrate as a platform for electrochemical measurements, small electrodes have been produced to interact with small sample volumes. Reduction of electrode area is ideal as this allows smaller volume samples to be used; however, a reduction in electrode area can reduce the signal obtained. To combat this, miniaturized devices have been produced that use a pair of cylindrical macroporous electrodes. First, a glass-capillary is coated with Ag, then a Ni layer is electrodeposited using a silica particle template, and, once the template is removed, Au is electrodeposited to fill the voids (**Fig. 1.6**). Subsequently the Ag, Ni, and glass

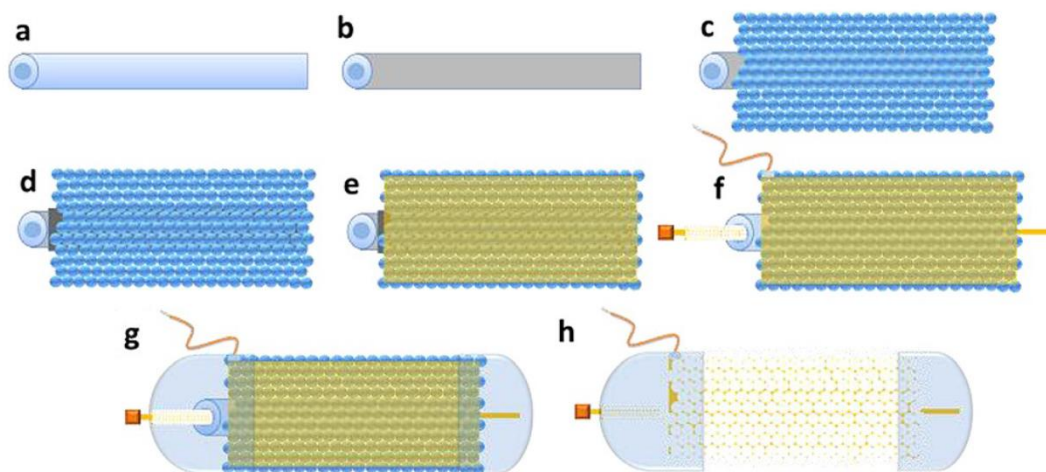


Figure 1.6. Scheme of fabrication of cylindrical macroporous gold electrode (a) glass capillary tube (b) electroless Ag coating, (c) silica particle template deposition, (d) electrodeposition of thin Ni layer onto Ag, (e) electrodeposition of Au into voids, (f) insertion of second macroporous electrode into capillary tube, (g) sealing of structure, (h) etching of template and glass capillary using HF. Adopted from ref. 88.

capillary are removed after the insertion of a second macroporous electrode into the capillary and sealing of the device.⁸⁸ These electrodes are an example of increasing the electroactive area with by using high surface area materials allowing for geometric area reduction without signal loss.

1.4. Additional Material Incorporation

It can be advantageous to incorporate additional metals into the framework of an electrode, especially one with high catalytic properties that offer a substantial increase in kinetic output or allow more sensitivity in response of specific molecules.⁸⁹ Many metals from the noble metal family are used for their catalytic properties, resistance to oxidation and corrosion in presence of moisture, and are inert. However, many members of the noble metals have downsides, such as high cost, high affinities to sulfur (form metal sulfides and sulfates), inability to be recycled when poisoned, and ones with a relatively low melting point, all of which make utilization of them unfavorable. The noble metals include ruthenium (Ru), rhodium (Rh), palladium (Pd), silver (Ag), osmium (Os), iridium (Ir), platinum (Pt), and gold (Au), although, rhodium, palladium, ruthenium, and platinum are the most commonly used as catalysts in electrochemical applications.⁹⁰ While these metals all are able to operate at low temperatures, more important is the d-orbital electron structure on the surface of their atoms. This structure promotes the formation of weak molecular bonds, providing a platform for a more strongly bonding reaction. These metals, however, do not experience a change in their structure, and do not participate in the actual reaction, but act to bring together other molecules. However, rhodium, palladium, and platinum are finite in supply, and the locations of mining sites are very limited, making the cost of these materials very high (one ounce of platinum, palladium, and rhodium is reported to be \$943.75, \$1041.05, and \$1111.98, respectively).⁹¹ Since the demand and applications for potential catalytic tools, such as electrodes, requires the incorporation of one or more of these catalytic metals, much research has been focused on how to lessen the amount needed to induce an efficient catalytic effect.^{89,92,93}

1.4.1. Platinum

Platinum is a noble metal, which has long had a prominent role in the workings of catalytic converters. Because of its ability to withstand oxygen-excessive conditions, platinum has played an important role when working in diesel applications.⁹⁴ However, growing demand for instruments which have the ability to detect, respond, and/or identify specific biological compounds, as well as the increasing push for power sources which create renewable and environmentally friendly energy has expanded the platform of platinum. Since it is the lowest in cost, when compared to palladium and rhodium, it is often chosen when reactivity is equally effective. Platinum has a high melting point, has limited interactions with poisons such as sulfur compounds, and can be efficiently recycled, all of which make it a competitive catalytic material.⁹⁵

Electrodes used for detection, reactivity, and identification of biological compounds have begun to incorporate themselves in medical applications, forensics, and even in biochemical sensors and diffusers.^{11,25} These electrode reactions rely heavily on the use of catalysts, particularly when there is a need for increased sensitivity, which is made possible due to the fast electron transfer kinetics. Platinum allows for a faster reaction in the presence of a variety of specific molecules, which otherwise would proceed at a rate too slow to see a response.⁹⁶

In fuel cells, platinum is desired, as it is able to oxidize oxygen at a faster and more efficient rate. This is important since fuel cells work, at the most basic level, to convert hydrogen and oxygen into water and produce electricity in the process. At the anode, hydrogen is oxidized to produce hydrogen ions and electrons, which flow to the cathode. Meanwhile, at the cathode, oxygen is reduced and, in reaction with the hydrogen ions, water is produced as the only by-

product. The catalytic properties of platinum can be exploited at both the anode and the cathode to assist in increasing the reaction kinetics.^{92,97,98}

Platinum catalysts are preferred over palladium catalysts to minimize hydrogenolysis when reducing nitro-compounds to amines.⁹⁹ Unfortunately, there are problems with platinum, the biggest ones being cost and limited quantity. These two downsides are connected as platinum naturally occurs in only two particular geological formations – mainly South Africa and Russia, where up to 80% of the world's Pt resources are held by South Africa alone. This short supply causes prices to increase as the growing demand increases.⁹¹ Another issue with platinum is the surface adsorbed carbon monoxide, which poisons the platinum, rendering it ineffective after it is coated.⁹²

1.4.2. Palladium

Palladium is used in catalysis, electronics, and in purification and storage of hydrogen. Palladium is an effective and popular catalytic material, and has similar properties to platinum, including a high melting point, and resistance to corrosion when operating at normal temperatures.¹⁰⁰ Additionally, palladium has a very strong affinity for hydrogen, owing to both its catalytic and hydrogen absorbing properties (up to 900 times its own volume) which require little to no activation energy when absorbed on the palladium surface.¹⁰¹ Because of this, palladium has been actively pursued and utilized for use in hydrogen purification, storage, detection, and fuel cells. The use of palladium over platinum for catalysis was promoted for two reasons, the primary one being a substantial difference in cost, with palladium being 1/5 of the cost of platinum in 2011 and \$222/oz. cheaper than platinum at the end of 2016.^{100,102} However, palladium is also limited in availability, with only one mine in the United States;

other mines also in Canada, South Africa, and Russia.¹⁰³ Recent demand for use in gasoline catalytic converters, and finite reserves have resulted in a cost inflation, whereby the price per ounce now exceeds that of platinum (\$943.75/oz. Pt compared to \$1041.05/oz. for Pd).⁹¹ The second reason for use of Pd over Pt as a catalyst is the tolerance to carbon monoxide, a trait platinum does not share. The susceptibility of platinum to carbon monoxide poisoning has introduced concerns over its widespread use in fuel cells, causing researchers to look for alternatives, such as palladium.¹⁰⁴

1.4.3. Rhodium

Rhodium (Rh) is another member of the noble metals, which has properties allowing for its use as a catalyst in a number of electrochemical applications. Rhodium is used extensively in the production of catalytic converters used in automobiles due to its low electrical resistance, high resistance to oxidation and very high melting point.^{105,106} Additionally Rh has a high electrical and heat conductivity, which also makes it suitable for catalysis applications. Rhodium is one of the rarest elements on Earth, as its abundance is thought to be around 0.0001 ppm.¹⁰⁷ (16) Because of its scarcity, rhodium is very expensive (\$1111.98/oz)⁹¹, and as such, is frequently used as an alloying agent in other materials, such as platinum and palladium. The influence of Rh increases reaction kinetics, as Rh has such a high electrical and heat conductivity. Rhodium is often alloyed with platinum and iridium to make an oxidation-resistant metal that can withstand very high temperatures.^{107,108}

1.4.4. Ruthenium

Ruthenium is another member of the platinum group of transition metals, and as such, is inert to most other chemicals. Ruthenium is the least expensive of the catalytic materials

introduced thus far, costing \$230.00/oz.¹⁰⁹ Used extensively as an oxide to coat anodes in chlorine production and in solar cells, it is also an effective hardener for platinum and palladium. If alloyed with platinum and/or palladium, ruthenium can be used as electrical contacts which are resistant to severe conditions, due to its anti-corrosive characteristics.¹¹⁰ Ruthenium is a highly catalytic substance, and has become common in the fabrication of fuel cells in the generation of Ru-Pt catalysts because of their ability to avoid CO poisoning, which is a common downside to direct alcohol fuel cells (DAFCs). Ruthenium is suspected to be carcinogenic, however, and is explosive in the presence of potassium chlorate.¹¹¹

1.4.5. Surface Modification

Instead of incorporating an additional metal into an electrode structure, it is possible to modify the surface in order to increase the sensitivity of the electrode for a particular analyte. The formation of self-assembled monolayers (SAMs) for use in electrochemical sensing has been used for almost three decades. Since the molecule ferrocene (Fc) has been known as an efficient electron mediator, the use of alkane thiols that have a terminal Fc group have been anchored to a gold electrode surface. The sulfur group binds to the Au leaving Fc available for electron transfer.^{112,113} Another method of modifying a surface is through the electrochemical grafting of a molecule onto an electrode surface.¹¹⁴ The reduction of a diazonium salt results in a radical that binds to the electrode surface.^{115,116} This technique has shown for preparing uniform and evenly distributed homogeneous monolayers of organic molecules. The immobilizing of enzymes, DNA, and antibodies will be discussed in Section 1.5.

1.5. Sensing Applications

The use of electrochemical tools for the sensing of target molecules falls into several categories. The use of enzymes, DNA, and antibodies immobilized onto the surface of an electrode has allowed for specific detection of analyte molecules giving a large signal for a generally small analyte concentration. Alternatively, direct sensing allows for a larger number of molecules that can show an electrochemical response depending on the experimental conditions.

1.5.1. Enzymatic

Sensors that employ enzymes use the inherent ability of these proteins to interact with target molecules that may not show a response on an electrode and form a detectable by-product. One of the most commonly used enzyme sensors is a commercially available glucose meter. The enzyme glucose oxidase is placed on a wicking test strip and when in the presence of glucose, the enzyme catalyzes the reaction to form hydrogen peroxide (H_2O_2). As opposed to glucose, H_2O_2 is detectable by measuring the current produced once the sample has interacted with the test strip. The signal current is then converted to concentration of glucose.^{117,118} In order to increase the efficiency of glucose detection, bienzymatic sensors have been produced. Coupling glucose oxidase, to form H_2O_2 , with horseradish peroxidase (HRP) has shown an enhanced signal with decrease signal degradation. HRP reduced H_2O_2 to water and the signal is generated through the reduction of the now oxidized HRP by the electrode surface.¹¹⁹

1.5.2. DNA

A similar technique to enzymatic sensors where target strands of single-stranded DNA (ssDNA) are detected instead involves ssDNA probe immobilization onto the electrode surface.

This probe will recognize complementary ssDNA strand and spontaneously form a double helix. A signal change will occur when the strands interact, known as hybridization.¹²⁰ There are several immobilization techniques including electrostatic adsorption, covalent bonding via a terminated thiol or amine group to the electrode surface, or biotinylation (where biotin binds to avidin/streptavidin).¹²¹ Additionally, the DNA can be labelled with a redox molecule to increase signal response and allow for greater sensitivity.¹²²

1.5.3. Immunosensors

The foundation of immunosensors takes advantage of the natural interactions between an antibody and the specific antigen that binds to it. The desired antibody is first immobilized onto the surface of an electrode. Immobilization techniques range from using a thiol bound to a gold surface to glass or silicon using an aminosilane as an anchor and linking an amine-terminated antibody to the linker.^{26,123,124} The next step involves labelling a non-anchored antibody that has a different active site than the anchored antibody, with a redox molecule like ferrocene or an

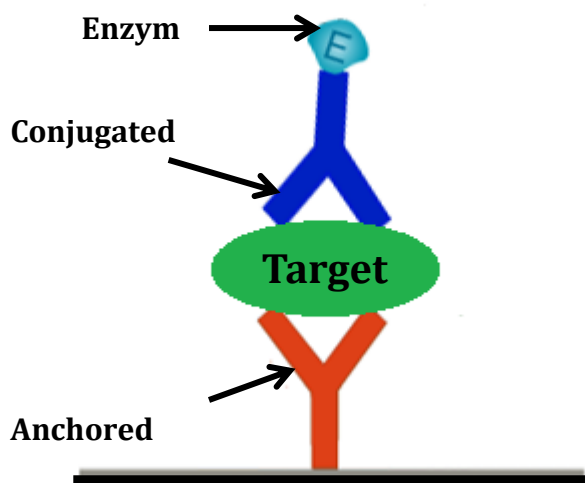


Figure 1.7. Cartoon representation of a sandwich-like antibody-antigen complex used in immunosensors.

enzyme that can catalyze a reaction in solution. Since the non-bound antibody is moving through the solution, it will eventually bind an antigen molecule if it is present. The antibody-antigen complex will then bind to the anchored antibody forming a sandwich-like complex that activates either the redox molecule or enzyme (**Fig. 1.7**). The redox molecule is then be oxidized or reduced and then interacts with the electrode surface to produce a signal.

1.5.4. Direct Sensing

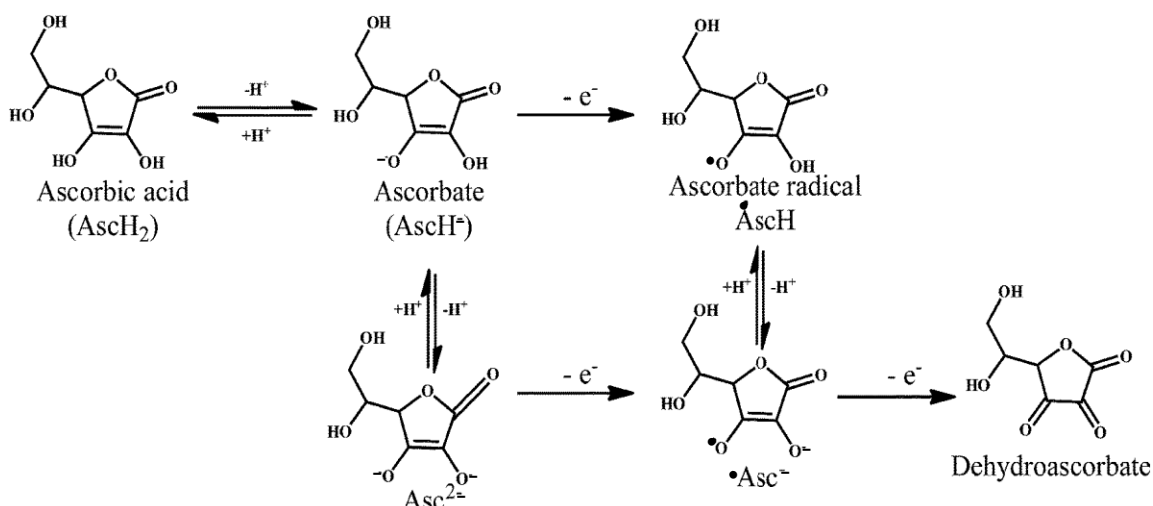
Specificity, as shown above, reduces the ability of electrodes to respond to a series of different molecules. The immobilization of antibodies, enzymes, or DNA has shown great response to individual target molecules. However, a multitude of different functionalization techniques would be necessary to develop in order to provide a sensing platform for a larger number of redox molecules. This is where the electrode material can be designed in a way to be sensitive to a number of redox molecules to improve the response to analytes. In order to accomplish this, it is necessary to understand how particular molecules of interest interact with the surface of an electrode as well as particular techniques that have been shown to increase the detection capability of electrodes. This work will present a brief overview of the relevance of and mechanism at which ascorbic acid, cysteine, uric acid, glucose, and hydrogen peroxide react when subjected to a particular electrochemical technique.

1.5.4.1. Ascorbic Acid

Commonly known as vitamin C, ascorbic acid (AA) plays a crucial role in healthy human function. The ability of AA to reduce free radicals by being converted to dehydroascorbic acid gives it its well-known antioxidant capabilities.^{4,125,126} Singlet oxygen can also be scavenged by AA and has been suggested, through intravenous injection, to be a treatment for cancer.¹²⁷

Humans, along with primates, are unable to produce ascorbic acid and must consume food containing the vitamin. The normal concentration of ascorbic acid in whole blood is $\sim 50 \mu\text{M}$.¹²⁸ The lack of AA can lead to connective tissue degeneration, also known as scurvy. The use of voltammetry,^{129,130} differential-pulse voltammetry,^{49,125,131} and potentiometry^{15,74} have been used to study the response of electrodes to the presence of ascorbic acid.

The oxidation of AA on the surface of an electrode occurs when the potential set is more positive than the formal redox potential. Ascorbic acid is a two-electron transfer molecule where, at physiological pH=7.4, one of the hydroxyl (-OH) groups is deprotonated forming the ascorbate ion. In the presence of a free radical or available electron, an electron is donated from ascorbate forming the ascorbate radical. This form can react with another ascorbate radical forming ascorbate and dehydroascorbate (**Scheme 1.1**).¹³² Oxidation of AA on an electrode

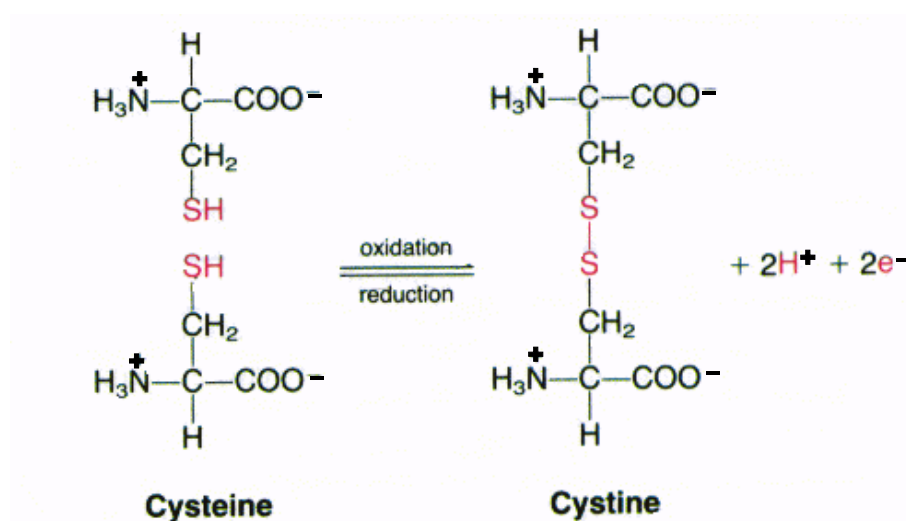


Scheme 1.1. Reaction mechanism of the radical scavenging of ascorbic acid. Adapted from ref. 130.

surface is proposed to occur with an ascorbate ion (in pH=7.4) transferring an electron to the surface and adsorbing. This causes the second hydroxyl group to interact with the electrode and a second electron is lost following or coupled with the loss of a proton (H^+).

1.5.4.2. Cysteine

The only one of the 20 amino acids that contains a sulfur group, cysteine is crucial in the formation of disulfide bridges in DNA as well as many different proteins, enzymes, ion channels and receptors.¹³³ Cysteine (Cys), along with glutathione (GSH), play important roles in the reduction of overall oxidative stress via the oxidation of cysteine to its disulfide form cystine (CySS) (**Scheme 1.2**). Cysteine sensing has been reported using cyclic voltammetry,^{134,135}



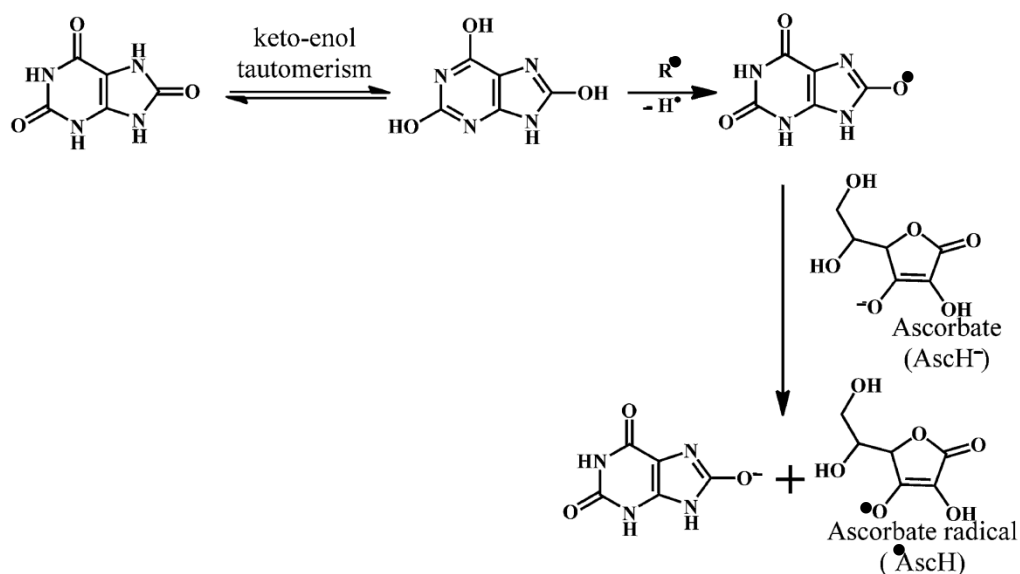
Scheme. 1.2. Oxidation reduction reaction of cysteine (Cys) oxidized to cystine (CySS).

interplasmon coupling,¹³⁶ and fluorescence assays.¹³⁷ It is noteworthy to mention that at physiological pH (7.4), Cys exists as a zwitterion as the carboxylic group hold a negative charge while the amine group is positively charged.^{137,138} An indicator of increased oxidative stress and possible disease has been shown in a decrease in the physiological concentration of cysteine (~100 μM) in whole blood. This is due to the scavenging of free-radical species by Cys at a rate faster than the ability of GSH to reduce CySS back to Cys. Given the sulfur present, cysteine and cystine are known to adsorb onto Au and Ag surfaces forming SAMs that can aid in the detection of dopamine and ascorbic acid. It has been suggested that the oxidation of Cys first begins with

the adsorption of the molecule onto the surface of the electrode as a radical. The ability to be oxidized depends on the distance at which the molecules adsorb. If the molecules adsorb with a favored orientation and are within ~ 2.88 angstroms of other adsorbed cysteine molecules, then oxidation can occur at an anodic potential.

1.5.4.3. Uric Acid

One of the most abundant antioxidants in whole blood ($\sim 300 \mu\text{M}$), uric acid is well known as the cause of gout and an indicator of hypertension. This occurs due to a buildup of excess uric acid in joints caused by the overconsumption rich foods containing purines. These purines are broken down to form uric acid. The mechanism of uric acid oxidation is unique to other biologically relevant redox molecules due to the inability of humans to break it down.¹³⁹ At physiological pH, uric acid is deprotonated and forms the urate ion. Like ascorbic acid and cysteine, uric acid undergoes a two-electron transfer. However, the radical scavenging ability of uric acid is seen through the initial conformational change due to keto-enol tautomerism



Scheme 1.3. Reaction mechanism of the radical scavenging of uric acid. Adapted from ref. 130.

(Scheme 1.3).¹³² The carbonyl group gains a proton from an adjacent amine group resulting in double bond and hydroxyl group formation. In physiological pH (7.4), the hydroxyl proton is lost leaving a negative charge on the oxygen. This negative charge can interact with a free radical species and form a urate radical. The presence of other molecules, like ascorbic acid, returns the urate radical to its ion form. The previously described stability of the ascorbyl radical is the driving force behind this natural radical scavenging pathway.¹³² In natural systems, uric acid is broken down via the enzyme uricase. In the absence of this enzyme, it has been hypothesized that the stability of the urate ion plays a significant role in the possible resistance to the second electron loss without the application of an external potential. Differential pulse and cyclic voltammetry have been extensively used to sense uric acid in addition to ascorbic acid and dopamine^{131,140–143}, which all involve inducing oxidation via an applied potential.

1.5.4.4. Glucose

The molecule has a reputation as the main indicator of diabetes as well as playing a critical role in physiological energy storage. Glucose is formed through the breakdown of more complex sugars or through the gluconeogenesis pathway. Stores of glucose are broken down through glycolysis to pyruvate, which is further broken down into two high-energy adenosine triphosphate (ATP) and two nicotinamide adenine dinucleotide (NADH) molecules. ATP can be broken through dephosphorylation to fuel cellular processes. Oxidation of glucose results in a loss of two electrons and two protons. Oxidation is enzymatically catalyzed by glucose oxidase, which also forms hydrogen peroxide as a by-product. Immobilization of this enzyme onto an electrode surface has been the focus of many groups where the amperometric detection of hydrogen peroxide is correlated to glucose concentration.^{118,144–148} However, advances have recently shown non-enzymatic detection as well using chronoamperometry.^{149–152}

1.5.4.5. Hydrogen Peroxide

Hydrogen peroxide, H_2O_2 , is a common by-product of the enzymatic breakdown of many biological molecules. Increases in H_2O_2 concentration have been correlated to an increase in oxidative stress due to its enzymatic formation from radical oxygen species (ROS). An increase in oxidative stress due to illness, disease, or severe fatigue can cause an increase in ROS and thus an increase in H_2O_2 . An increase in concentration can lead to attack of cellular structures or biomolecules, like liposomes, DNA, or proteins.¹⁵³ The importance of the concentration of H_2O_2 in physiological samples ($\sim 10 \mu\text{M}$) has led to a large push in developing methods and materials for sensing.

As mentioned previously in Section 1.5.4.4., glucose oxidase will produce H_2O_2 in the presence of glucose.^{118,144–148} A linear relationship between H_2O_2 and current produced at a set potential has been shown. An increase in the concentration of H_2O_2 will lead to a corresponding increase in current.^{154,155} Also, fluorescent probes have been used to detect H_2O_2 near mitochondrial DNA.^{153,156}

1.6. Fuel Cell Catalysis

The fabrication of catalysts for use in fuel cells is a growing and active area of research, answering the demand for renewable and environmentally friendly energy sources. Additionally, fuel cells have been shown to have comparable efficiency, output, and portability to traditional fossil fuel energy sources. Research of fuel cells has produced a few variations in structure and fuel used, but fundamentally, these are all devices that generate electrical energy via chemical reactions. Most fuel cells catalyze both an oxidation reaction (using hydrogen or other fuel) and

an oxygen reduction reaction, using hydrogen and oxygen to produce water and heat overall, and creating electricity. Since fuel cells produce electricity through an electrochemical process, and not combustion, the process is clean, quiet, and very efficient.

1.6.1. Types

Fuel cells represent a growing field of research, and as such, vary in structure, fuel source, and electrolyte used. Fuel cells are primarily classified based on the electrolyte they utilize, and since these differences can impact the reactions which occur in the cell, the type of catalyst needed, the optimal temperature, and fuel type, the specific fuel cell application is an important consideration. There are, however, some commonplace and widely used types of fuel cells, and much of the current research focuses on altering components of these five popular cells; polymer electrolyte membrane fuel cells (PEMFC), alkaline fuel cells (AFC), phosphoric acid fuel cells (PAFC), molten carbonate fuel cells (MCFC), solid oxide fuel cells (SOFC), and direct alcohol fuel cells (DAFC).

One widely adopted type of fuel cell is the proton exchange membrane fuel cell, also known as polymer electrolyte membrane fuel cells (PEMFC). PEM fuel cells use a solid polymer as an electrolyte and porous carbon electrodes containing a platinum or platinum alloy catalyst. The central core of the PEMFC is the membrane electrode assembly (MEA), which is a construct containing electrodes and membranes. Each electrode consists of a gas diffusion layer, as well as a catalytic layer. The MEA moves existing ions through the cathode, after oxidizing the fuel at the anode, creating water and heat as by-products.¹⁵⁷ PEMFCs are typically fueled with pure hydrogen from tanks or reformers, water, and oxygen from the air. PEM fuel cells are durable and long lasting, due to their ability to operate at low temperatures, allowing them to start

quickly and put less stress on system components. Additionally, PEM fuel cells have a power to weight ratio of 45-60% (compared to the average U.S. power grid at 35% efficiency), which makes them good candidates for use in automobiles and electronics.¹⁵⁸ However, these cells require a noble metal catalyst, such as platinum, and this makes the fuel cell costly. Typical loadings in the electrode today are about 0.4-0.8 mg platinum/cm², which is significantly lower than 25 mg/cm² with early platinum black catalysts.¹⁵⁹ The US Department of Energy (DOE) has set targets of 0.3 mg/cm² for 2010 and 0.2 mg/cm² for 2015.¹⁶⁰

Another popular type of fuel cell is the alkaline fuel cell, which has been used since the mid-1960s by NASA because of the high power generating abilities - about 70% efficiency.¹⁶¹ Alkaline fuel cells use a potassium hydroxide solution as the electrolyte. The concentration of the potassium hydroxide (KOH) solution can be manipulated depending on the desired temperature of use. While a large variety of catalysts can be used in AFCs (Ni, Ag, noble metals, metal oxides), the fuel must be pure hydrogen since any amount of CO₂ will poison the electrode.¹⁶² AFCs are also very costly, making commercial application unfeasible.¹⁶³

Phosphoric (or Sulfuric) Acid Fuel Cells (PAFC) are popular since they are more tolerant to CO₂, allowing the use of regular air and non-pure hydrogen. However, since liquid phosphoric acid is used as the electrolyte there are issues with corrosion because it is non-volatile and only water is lost via evaporation. This tendency towards corrosion restricts the options for electrode and catalyst materials. The electrodes are usually constructed from gold, titanium, and/or carbon, while platinum group catalysts are singularly employed. The optimal temperature of acid fuel cells is around 200 °C, but this high temperature makes platinum sensitive to CO poisoning, and lower temperatures (150 °C) diminish efficiency and current density. These fuel cells are able to

generate electricity around 40% efficiency (point of comparison - power grid in U.S. is about 35%), making them a viable alternative source of energy.

Molten carbonate fuel cells (MCFC) use a molten carbonate salt, such as lithium carbonate, potassium carbonate, or sodium carbonate, suspended in a porous ceramic matrix as the electrolyte. MCFCs can use a variety of different fuels since their operating high temperature (around 650°C) decreases the cell's sensitivity to carbon monoxide poisoning.¹⁶⁴ These fuels include methane, coal-derived fuel gas, or natural gas, all of which eliminate the need for external reformers. The high temperature also increases reaction kinetics, eliminating the need for a noble metal catalyst. MCFC's are stationary power sources, achieving an efficiency of 60-80%. However, there are some downsides to MCFs, such as limited transport capabilities since the electrolyte is liquid, CO₂ must be injected regularly into the cathode, the cell has a tendency towards corrosion, and the cost of the steel components is substantial.¹⁶⁵

The solid oxide fuel cells (SOFC) use a solid ceramic electrolyte, such as zirconium oxide, and are seen in three different constructs; planar, coplanar, and microtubular. The planar designs consist of flat stacks with channels in the anode and cathode to allow air and hydrogen through. The tubular design is comprised of a solid oxide tube, which is sealed on one end, forming the cathode. Air is supplied to the inside of an extended solid oxide tube (which is sealed at one end) while fuel flows round the outside of the tube. SOFCs work at very high temperatures (800-1,000°C), allowing for high energy output (50-60%),¹⁶⁶ with even higher output possibilities if the heat released is harnessed (80%).¹⁶⁷ The high operating temperature also increases the choice in fuel types, removes the need for a reaction catalyst, and is able to reform fuels internally. Because of this high efficiency, solid oxide fuel cells are used extensively in large and small stationary power plants, which can use the cogeneration of steam

for additional power. Overall, SOFCs have few problems with electrolyte management, and have little corrosion tendencies. However, the cost of manufacture remains very high, and is impractical for production on a large, commercial scale.¹⁶⁸

The direct alcohol fuel cell (DAFC) was originally invented and developed in the 1990s. Notably, the direct alcohol fuel cell's ability to utilize hydrogen directly from the alcohol fuel, thereby making this fuel cell a viable source of mainstream, commercially available power.¹⁶⁹ By constructing the fuel cell with a platinum based anode, the cells can use alcohols such as methanol, ethanol, isopropyl, or formic acid, to draw hydrogen from, with a by-product of electrical energy and water.¹⁷⁰ DMFCs are easier to transport, allowing for use in portable devices, and operate at a temperatures between 50-90°C. A traditional direct alcohol fuel cell (DAFC) is based on the polymer electrode membrane (PEM) fuel cell modules that use a membrane electrolyte. In these electrodes, the polymer membrane is made of a range of different materials, and is the basis of much research.¹⁷¹ Factors which complicate DAFC commercialization include the typically lower efficiency and power density, as well as the higher cost of DAFCs compared to H₂-based fuel cells, due to the need for expensive platinum catalysts.^{92,145}

1.6.2. Fuels

Direct alcohol fuel cells (DAFC) are able to harness the hydrogen available in simple alcohols and formic acid, in an oxidation reaction occurring at the anode, with a subsequent reduction at the cathode. This field of electrochemistry is of importance since previous fuel cells necessitate the use of pure hydrogen as a fuel source, or operate at extreme temperatures, making widespread commercialization unfeasible. The need for pure H₂ requires a reformer for

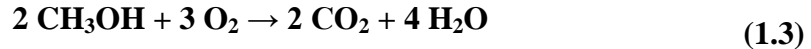
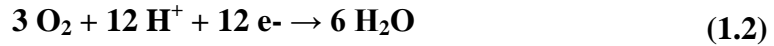
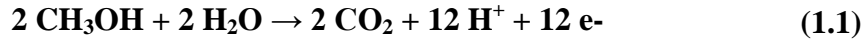
purification and/or a tank attachment, while operation at very high temperatures demands fabrication with materials designed to protect and sustain the heat released in these reactions. Both of these added requirements present cost issues, which makes DAFCs more competitive, as the fuel source is more readily available, and the added equipment and materials is unneeded. Additionally, the hazards posed by using a volatile fuel source such as pure H₂, and use at temperatures at or exceeding 650°C, are such that use in mainstream applications is very limited.^{172–176}

This presented work focuses on the fabrication and implementation of a nanoporous gold substrate positioned on a glass backbone. This gold electrode provided an easy transition into a direct alcohol fuel cell utilizing a sulfuric acid electrolyte. By speckling the nanoporous surface with very small amounts of platinum catalyst, the resulting reactive electrode created a direct alcohol fuel half-cell, which was then tested for efficacy in different fuels, such as the alcohols methanol and ethanol, as well as formic acid. Many of the precursors of the direct alcohol fuel cells have, and continue to, utilize pure hydrogen as a fuel source; however, this work does not investigate hydrogen as a potential fuel.

1.6.2.1. Methanol

Methanol is a simple alcohol, but has very high hydrogen to carbon ratio (4H per C), an important characteristic since DMFCs use a series of oxidation and reduction reactions to turn that hydrogen into electricity. Methanol is a high-density fuel source compared to pure hydrogen (over 6000 W hr/kg), releasing six protons and electrons per molecule during oxidation. It's ability to function at low temperatures (30-150°C),¹⁷⁷ and low cost make methanol a viable fuel option. Compared to ethanol, methanol has high selectivity to CO₂ formation during the

electrochemical oxidation process, which gives it a marked advantage as a fuel source. Methanol can be obtained from currently used fossil fuels, such as natural gas or coal, but can be acquired through fermentation of agricultural products in the form of biomasses. In this way, methanol can be characterized as a renewable fuel source, and since CO₂ is the most harmful byproduct, methanol is environmentally friendly,^{174,178,179} and is a liquid at ambient temperatures, and can be stored as such, which means it can utilize existing infrastructure for storage and transportation. Notably, methanol can be directly fed into a fuel cell without the need of a reformer. However, methanol fuel cells have raised concerns over membrane crossover due the ability of methanol to permeate the membrane, which ultimately decreases overall cell efficiency. Unlike reformer-based systems, which convert methanol to hydrogen, the DMFC directly oxidizes the methanol at the anode (**Eq. 1.1**), while reducing oxygen at the cathode (**Eq. 1.2**). The overall reaction is shown in **Equation 1.3**.¹⁸⁰

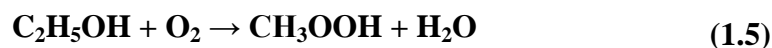


1.6.2.2. Ethanol

Ethanol, like methanol is a hydrogen rich, simple alcohol, with the propensity to be a renewable and environmentally friendly energy source. Since ethanol is currently used in gasoline (10%) for combustion engines, the infrastructure needed for the production and manufacture is already present, which may pose less setup; while transportation and storage of ethanol requires less controls and precautions since it is not as toxic to humans as methanol or hydrogen.¹⁸¹ Ethanol is produced via fermentation of certain carbohydrates which then are

filtered, distilled and dehydrated (removal of water).¹⁸² Ethanol has a higher specific energy (8.0 kWh/kg) compared to methanol (6.1 kWh/kg).¹⁸³ Ethanol does have a slow reaction time, even with catalysts present, making optimization of the anode material a main research focus.

When the reaction is most efficient, the only products are carbon dioxide (CO₂) and water (H₂O). A less efficient reaction results in acetic acid (CH₃COOH, **Eq. 1.5**) which is, as its name might suggest, an acid. So the more efficient the fuel cell's reaction, the less acidic its product will be.¹⁸⁴ The overall reaction of the complete oxidation of ethanol is shown in **Equation 1.4**.²⁷



1.6.2.3. Formic Acid

Formic acid is a promising fuel alternative, since it has a high volumetric capacity (53 g H₂/L), and is an efficient hydrogen carrier where 1L of formic acid carries 590L of elemental hydrogen, while having low toxicity and flammability.²⁷ Since formic acid is a liquid under normal conditions, and can be stored as such and widely used in agriculture and industry, there is the ability to utilize existing infrastructure for manufacture, transport, and storage. Formic acid represents an environmentally friendly and renewable fuel option, which boasts oxidation kinetics and better energy conversion efficiency than methanol and traditional hydrogen fuel cells.²⁷ However, formic acid is unstable for long periods since it quickly poisons and deactivates the platinum-based catalysts utilized in the fuel cell construct, making commercial manufacture and use of formic acid fuel cells improbable without development of a more CO tolerant cell.²⁷

1.7. Thesis Statement

In this work, the production and investigation of different nanoporous gold (NPG) based electrodes using low-cost and readily available materials in order to create an electrode capable of responding to a variety of redox molecules. Electrode response to standard and biologically relevant redox molecules was first investigated in the presence of biofouling agents. Low-cost routes were employed to fabricate NPG electrodes on a glass substrate, which allowed for potentiometric measurements in nanoscopic volumes when coupled with an inverted microscope. This method was exploited further to produce NPG on capillary tubes that allowed for single drop solution volumes using several biologically relevant molecules. To enhance the electrode response to otherwise non-responsive molecules, a minimal amount of platinum was incorporated into the NPG structure. Finally, the crossover capability of the fabricated electrodes into different electrochemistry applications such as fuel cell catalysis was investigated. Research aims to introduce a low-cost electrode with the flexibility to respond to numerous species enhanced with the minimal addition of platinum in biosensing and catalysis applications.

1.8. References

1. Loewenstein, D., Stake, C. and Cichon, M. Assessment of using fingerstick blood sample with i-STAT point-of-care device for cardiac troponin i assay. *Am. J. Emerg. Med.* **31**, 1236–1239 (2013).
2. Ryan, R. J., Lindsell, C. J., Hollander, J. E., O’Neil, B., Jackson, R., Schreiber, D., Christenson, R. and Gibler, W. B. A Multicenter Randomized Controlled Trial Comparing Central Laboratory and Point-of-Care Cardiac Marker Testing Strategies: The Disposition Impacted by Serial Point of Care Markers in Acute Coronary Syndromes (DISPO-ACS) Trial. *Ann. Emerg. Med.* **53**, 321–328 (2009).
3. Alpert, J. S., Thygesen, K. A., White, H. D. and Jaffe, A. S. Diagnostic and therapeutic implications of type 2 myocardial infarction: Review and commentary. *Am. J. Med.* **127**, 105–108 (2014).
4. Roginsky, V. A. and Stegmann, H. B. Ascorbyl radical as natural indicator of oxidative stress: quantitative regularities. *Free Radic. Biol. Med.* **17**, 93–103 (1994).
5. Tian, N., Zhou, Z. Y. and Sun, S. G. Platinum metal catalysts of high-index surfaces: from single-crystal planes to electrochemically shape-controlled nanoparticles. *J. Phys. Chem. C* **112**, 19801–19817 (2008).
6. Bryce C, T., Stephen A, S. and Luther, E. P. Nanoporous metal foams. *Angew. Chemie - Int. Ed.* **49**, 4544–4565 (2010).
7. Sirringhaus, H. Reliability of organic field-effect transistors. *Adv. Mater.* **21**, 3859–3873 (2009).
8. Acton, O., Ting, G., Ma, H., Ka, J. W., Yip, H. L., Tucker, N. M. and Jen, A. K. Y. Π - Σ -Phosphonic Acid Organic Monolayer/Sol-Gel Hafnium Oxide Hybrid Dielectrics for Low-Voltage Organic Transistors. *Adv. Mater.* **20**, 3697–3701 (2008).
9. Auroux, P.-A., Koc, Y., deMello, A., Manz, A. and Day, P. J. R. Miniaturised nucleic acid analysis. *Lab Chip* **4**, 534 (2004).
10. Lewenstam, A. Routines and Challenges in Clinical Application of Electrochemical Ion-Sensors. *Electroanalysis* **26**, 1171–1181 (2014).
11. Tiwari, J. N., Vij, V., Kemp, K. C. and Kim, K. S. Engineered carbon-nanomaterial-based electrochemical sensors for biomolecules. *ACS Nano* **10**, 46–80 (2016).
12. Yin, T. and Qin, W. Applications of nanomaterials in potentiometric sensors. *TrAC - Trends Anal. Chem.* **51**, 79–86 (2013).
13. Kimmel, D. W., Leblanc, G., Meschievitz, M. E. and Cliffel, D. E. Electrochemical sensors and biosensors. *Anal. Chem.* **84**, 685–707 (2012).
14. Bard, A. J. and Faulkner, L. R. *Electrochemical Methods: Fundamentals and Applications*. (John Wiley and Sons, Inc., 1980).
15. Farghaly, A. a., Lam, M., Freeman, C. J., Uppalapati, B. and Collinson, M. M. Potentiometric Measurements in Biofouling Solutions: Comparison of Nanoporous Gold to Planar Gold. *J. Electrochem. Soc.* **163**, H3083–H3087 (2016).
16. Guo, D. J. and Ding, Y. Porous Nanostructured Metals for Electrocatalysis. *Electroanalysis* **24**, 2035–2043 (2012).
17. Snyder, J., Livi, K. and Erlebacher, J. Dealloying Silver/Gold Alloys in Neutral Silver Nitrate Solution: Porosity Evolution, Surface Composition, and Surface Oxides. *J. Electrochem. Soc.* **155**, C464 (2008).

18. Kozai, T. D. Y., Jaquins-Gerstl, A. S., Vazquez, A. L., Michael, A. C. and Cui, X. T. Brain tissue responses to neural implants impact signal sensitivity and intervention strategies. *ACS Chem. Neurosci.* **6**, 48–67 (2015).
19. Kuhlmann, J., Dzugan, L. C. and Heineman, W. R. Comparison of the Effects of Biofouling on Voltammetric and Potentiometric Measurements. *Electroanalysis* **24**, 1732–1738 (2012).
20. Wisniewski, N. and Reichert, M. Methods for reducing biosensor membrane biofouling. *Colloids Surfaces B Biointerfaces* **18**, 197–219 (2000).
21. Wisniewski, N., Moussy, F. and Reichert, W. M. Characterization of implantable biosensor membrane biofouling. *Fresenius J. Anal. Chem.* **366**, 611–621 (2000).
22. Chin, C. D., Linder, V. and Sia, S. K. Commercialization of microfluidic point-of-care diagnostic devices. *Lab Chip* **12**, 2118 (2012).
23. Das, J., Jo, K., Jae, W. L. and Yang, H. Electrochemical immunosensor using p-aminophenol redox cycling by hydrazine combined with a low background current. *Anal. Chem.* **79**, 2790–2796 (2007).
24. Hrapovic, S., Liu, Y., Male, K. B. and Luong, J. H. T. Electrochemical Biosensing Platforms Using Platinum Nanoparticles and Carbon Nanotubes. *Anal. Chem.* **76**, 1083–1088 (2004).
25. Xu, Y. and Wang, E. Electrochemical biosensors based on magnetic micro/nano particles. *Electrochim. Acta* **84**, 62–73 (2012).
26. Zhang, R. and Olin, H. Porous gold films-a short review on recent progress. *Materials (Basel)*. **7**, 3834–3854 (2014).
27. Gomes, J. F., Bergamaski, K., Pinto, M. F. S. and Miranda, P. B. Reaction intermediates of ethanol electro-oxidation on platinum investigated by SFG spectroscopy. *J. Catal.* **302**, 67–82 (2013).
28. Cacciola, G., Antonucci, V. and Freni, S. Technology up date and new strategies on fuel cells. *J. Power Sources* **100**, 67–79 (2001).
29. Gubala, V., Harris, L. F., Ricco, A. J., Tan, M. X. and Williams, D. E. Point of care diagnostics: Status and future. *Anal. Chem.* **84**, 487–515 (2012).
30. Li, C. M. and Hu, W. Electroanalysis in micro- and nano-scales. *J. Electroanal. Chem.* **688**, 20–31 (2013).
31. Trouillon, R., Passarelli, M. K., Wang, J., Kurczy, M. E. and Ewing, A. G. Chemical analysis of single cells. *Anal. Chem.* **85**, 522–542 (2013).
32. Wahl, a., Barry, S., Dawson, K., MacHale, J., Quinn, a. J. and O’Riordan, a. Electroanalysis at Ultramicro and Nanoscale Electrodes: A Comparative Study. *J. Electrochem. Soc.* **161**, B3055–B3060 (2013).
33. Chapman, C. a R., Chen, H., Stamou, M., Biener, J., Biener, M. M., Lein, P. J. and Seker, E. Nanoporous gold as a neural interface coating: Effects of topography, surface chemistry, and feature size. *ACS Appl. Mater. Interfaces* **7**, 7093–7100 (2015).
34. Reay, R. and Flannery, A. Microfabricated electrochemical analysis system for heavy metal detection. *Sensors Actuators B ...* **34**, 450–455 (1996).
35. Herzog, G. and Beni, V. Stripping voltammetry at micro-interface arrays: A review. *Anal. Chim. Acta* **769**, 10–21 (2013).
36. Xie, X., Stueben, D. and Berner, Z. The Application of Microelectrodes for the Measurements of Trace Metals in Water. *Anal. Lett.* **38**, 2281–2300 (2005).
37. Taillefert, M., Luther, G. W. and Nuzzio, D. B. The application of electroanalytical tools

- for in situ measurements in aquatic systems. *Electroanalysis* **12**, 411 (2000).
38. Kolluri, K. and Demkowicz, M. J. Coarsening by network restructuring in model nanoporous gold. *Acta Mater.* **59**, 7645–7653 (2011).
 39. Rouquerolt, J., Avnir, D., Fairbridge, C. W., Everett, D. H., Haynes, J. H., Pernicone, N., Ramsay, J. D. F., Sing, K. S. W. and Unger, K. K. Recommendations for the characterization of porous solids. *Pure Appl. Chem.* **66**, 1739–1758 (1994).
 40. Zhao, B. and Collinson, M. M. Hierarchical porous gold electrodes: Preparation, characterization, and electrochemical behavior. *J. Electroanal. Chem.* **684**, 53–59 (2012).
 41. Collinson, M. M. Nanoporous Gold Electrodes and Their Applications in Analytical Chemistry. *ISRN Anal. Chem.* **2013**, 1–21 (2013).
 42. Wittstock, A., Wichmann, A., Bäumer, M. and Ba, M. Nanoporous gold as a platform for a building block catalyst. *ACS Catal.* **2**, 2199–2215 (2012).
 43. Patel, J., Radhakrishnan, L., Zhao, B., Uppalapati, B., Daniels, R. C., Ward, K. R. and Collinson, M. M. Electrochemical properties of nanostructured porous gold electrodes in biofouling solutions. *Anal. Chem.* **85**, 11610–11618 (2013).
 44. Fujita, T., Guan, P., McKenna, K., Lang, X., Hirata, A., Zhang, L., Tokunaga, T., Arai, S., Yamamoto, Y., Tanaka, N., Ishikawa, Y., Asao, N., Yamamoto, Y., Erlebacher, J. and Chen, M. Atomic origins of the high catalytic activity of nanoporous gold. *Nat. Mater.* **11**, 775–780 (2012).
 45. Bond, G. C. The Catalytic Properties of Gold. *Gold Bull.* **5**, 11–13 (1972).
 46. Matharu, Z., Daggumati, P., Wang, L., Dorofeeva, T. S., Li, Z. and Seker, E. Nanoporous-Gold-Based Electrode Morphology Libraries for Investigating Structure-Property Relationships in Nucleic Acid Based Electrochemical Biosensors. *ACS Appl. Mater. Interfaces* **9**, 12959–12966 (2017).
 47. Bélanger, D. and Pinson, J. Electrografting: a powerful method for surface modification. *Chem. Soc. Rev.* **40**, 3995 (2011).
 48. Chapman, C. A., Wang, L., Biener, J., Seker, E., Biener, M. M. and Matthews, M. J. Engineering On-Chip Nanoporous Gold Material Libraries via Precision Photothermal Treatment. *Nanoscale* **8**, 785–795 (2016).
 49. Bhattarai, J., Neupane, D., Nepal, B., Mikhaylov, V., Demchenko, A. and Stine, K. Preparation, Modification, Characterization, and Biosensing Application of Nanoporous Gold Using Electrochemical Techniques. *Nanomaterials* **8**, 171 (2018).
 50. Zhao, B. and Collinson, M. M. Well-defined hierarchical templates for multimodal porous material fabrication. *Chem. Mater.* **22**, 4312–4319 (2010).
 51. Biswas, A., Bayer, I. S., Biris, A. S., Wang, T., Dervishi, E. and Faupel, F. Advances in top-down and bottom-up surface nanofabrication: Techniques, applications and future prospects. *Adv. Colloid Interface Sci.* **170**, 2–27 (2012).
 52. Fang, C., Bandaru, N. M., Ellis, A. V. and Voelcker, N. H. Electrochemical fabrication of nanoporous gold. *J. Mater. Chem.* **22**, 2952–2957 (2012).
 53. Leitao, D. C., Apolinario, A., Sousa, C. T., Ventura, J., Sousa, J. B., Vazquez, M. and Araujo, J. P. Nanoscale topography: A tool to enhance pore order and pore size distribution in anodic aluminum oxide. *J. Phys. Chem. C* **115**, 8567–8572 (2011).
 54. Zhang, Q., Wang, X., Qi, Z., Wang, Y. and Zhang, Z. A benign route to fabricate nanoporous gold through electrochemical dealloying of Al-Au alloys in a neutral solution. *Electrochim. Acta* **54**, 6190–6198 (2009).
 55. Rouya, E., Reed, M. L., Kelly, R. G., Bart-Smith, H., Begley, M. and Zangari, G.

- Synthesis of Nanoporous Gold Structures via Dealloying of Electroplated Au-Ni Alloy Films. *ECS Trans.* **6**, 41–50 (2007).
56. Erlebacher, J. An Atomistic Description of Dealloying. *J. Electrochem. Soc.* **151**, C614 (2004).
 57. Zhang, Z., Wang, Y., Qi, Z., Zhang, W., Qin, J. and Frenzel, J. Generalized fabrication of nanoporous metals (Au, Pd, Pt, Ag, and Cu) through chemical dealloying. *J. Phys. Chem. C* **113**, 12629–12636 (2009).
 58. Grillo, R., Torrisi, V. and Ruffino, F. Nanoporous Au: An experimental study on the porosity of dealloyed AuAg leafs. *Superlattices Microstruct.* **100**, 780–791 (2016).
 59. Erlebacher, J., Aziz, M. J., Karma, A., Dimitrov, N. and Sieradzki, K. Evolution of nanoporosity in dealloying. *Nature* **410**, 450–453 (2001).
 60. Ding, Y., Kim, Y. J. and Erlebacher, J. Nanoporous gold leaf: ‘Ancient technology’/advanced material. *Adv. Mater.* **16**, 1897–1900 (2004).
 61. Seker, E., Reed, M. L. and Begley, M. R. Nanoporous gold: Fabrication, characterization, and applications. *Materials (Basel)*. **2**, 2188–2215 (2009).
 62. McCue, I., Benn, E., Gaskey, B. and Erlebacher, J. Dealloying and Dealloyed Materials. *Annu. Rev. Mater. Res.* **46**, 263–286 (2016).
 63. Dixon, M. C., Daniel, T. A., Hieda, M., Smilgies, D. M., Chan, M. H. W. and Allara, D. L. Preparation, structure, and optical properties of nanoporous gold thin films. *Langmuir* **23**, 2414–2422 (2007).
 64. Snyder, J., Asanithi, P., Dalton, A. B. and Erlebacher, J. Stabilized nanoporous metals by dealloying ternary alloy precursors. *Adv. Mater.* **20**, 4883–4886 (2008).
 65. Jin, C., Olsen, B. C., Lubner, E. J. and Buriak, J. M. Nanopatterning via solvent vapor annealing of block copolymer thin films. *Chem. Mater.* **29**, 176–188 (2017).
 66. Vega, A. A. and Newman, R. C. Methanol electro-oxidation on nanoporous metals formed by dealloying of Ag–Au–Pt alloys. *J. Appl. Electrochem.* **46**, 995–1010 (2016).
 67. Akbarzadeh, H., Shamkhali, A. N., Abbaspour, M., Salemi, S. and Hajizadeh, Z. Effect of Pt addition to Ag[sbnd]Au bimetallic nanoclusters: A molecular dynamics study of Ag[sbnd]Au[sbnd]Pt ternary system. *J. Alloys Compd.* **692**, 647–657 (2017).
 68. Hsieh, Y.-T. and Sun, I.-W. One-step electrochemical fabrication of nanoporous gold wire arrays from ionic liquid. *Chem. Commun.* **50**, 246–248 (2014).
 69. Garcia-Gradilla, V., Sattayasamitsathit, S., Soto, F., Kuralay, F., Yardimci, C., Wiitala, D., Galarnyk, M. and Wang, J. Ultrasound-propelled nanoporous gold wire for efficient drug loading and release. *Small* **10**, 4154–4159 (2014).
 70. Harnisch, J. A., Pris, A. D. and Porter, M. D. Attachment of gold nanoparticles to glassy carbon electrodes via a mercaptobenzene film [1]. *J. Am. Chem. Soc.* **123**, 5829–5830 (2001).
 71. Wang, D. and Schaaf, P. Nanoporous gold nanoparticles. *J. Mater. Chem.* **22**, 5344 (2012).
 72. Siepenkoetter, T., Salaj-Kosla, U., Xiao, X., Belochapkin, S. and Magner, E. Nanoporous Gold Electrodes with Tuneable Pore Sizes for Bioelectrochemical Applications. *Electroanalysis* **28**, 2415–2423 (2016).
 73. Lee, K. U., Tran, T. H., Kim, S. H. and Shin, H. J. Fabrication of nanoporous gold thin films on glass substrates for amperometric sensing of aniline. *J. Alloys Compd.* **713**, 132–137 (2017).
 74. Freeman, C. J., Farghaly, A. A., Choudhary, H., Chavis, A. E., Brady, K. T., Reiner, J. E.

- and Collinson, M. M. Microdroplet-Based Potentiometric Redox Measurements on Gold Nanoporous Electrodes. *Anal. Chem.* **88**, 3768–3774 (2016).
75. Campbell, F. W. and Compton, R. G. The use of nanoparticles in electroanalysis: An updated review. *Anal. Bioanal. Chem.* **396**, 241–259 (2010).
 76. DiBenedetto, S. A., Facchetti, A., Ratner, M. A. and Marks, T. J. Molecular self-assembled monolayers and multilayers for organic and unconventional inorganic thin-film transistor applications. *Adv. Mater.* **21**, 1407–1433 (2009).
 77. Piwoński, I., Grobelny, J., Cichomski, M., Celichowski, G. and Rogowski, J. Investigation of 3-mercaptopropyltrimethoxysilane self-assembled monolayers on Au(111) surface. *Appl. Surf. Sci.* **242**, 147–153 (2005).
 78. Ciesielski, P. N., Scott, A. M., Faulkner, C. J., Berron, B. J., Cliffel, D. E. and Jennings, G. K. Functionalized Nanoporous Gold Leaf Photosystem I. *ACS Nano* **2**, 2465–2472 (2008).
 79. Troyer, K. P. and Wightman, R. M. Dopamine transport into a single cell in a picoliter vial. *Anal. Chem.* **74**, 5370–5375 (2002).
 80. Yasukawa, T., Glidle, A., Cooper, J. M. and Matsue, T. Electroanalysis of metabolic flux from single cells in simple picoliter-volume microsystems. *Anal. Chem.* **74**, 5001–5008 (2002).
 81. Clark, R. A., Hietpas, P. B. and Ewing, A. G. Electrochemical Analysis in Picoliter Microvials. *Anal. Chem.* **69**, 259–263 (1997).
 82. Blaz, T., Baś, B., Kupis, J., Migdalski, J. and Lewenstam, A. Multielectrode potentiometry in a one-drop sample. *Electrochem. commun.* **34**, 181–184 (2013).
 83. Bogue, R. Lab-on-a-chip and other miniaturised analytical instruments. *Sens. Rev.* **36**, 109–114 (2016).
 84. Neužil, P., Giselsbrecht, S., Längle, K., Huang, T. J. and Manz, A. Revisiting lab-on-a-chip technology for drug discovery. *Nat. Rev. Drug Discov.* **11**, 620–632 (2012).
 85. Morita, M., Niwa, O. and Horiuchi, T. Interdigitated array microelectrodes as electrochemical sensors. *Electrochim. Acta* **42**, 3177–3183 (1997).
 86. Niwa, O., Morita, M. and Tabei, H. Electrochemical Behavior of Reversible Redox Species at Interdigitated Array Electrodes with Different Geometries: Consideration of Redox Cycling and Collection Efficiency. *Anal. Chem.* **62**, 447–452 (1990).
 87. Daniel, D. and Gutz, I. G. R. Microfluidic cells with interdigitated array gold electrodes: Fabrication and electrochemical characterization. *Talanta* **68**, 429–436 (2005).
 88. Karajić, A., Reculosa, S., Ravaine, S., Mano, N. and Kuhn, A. Miniaturized Electrochemical Device from Assembled Cylindrical Macroporous Gold Electrodes. *ChemElectroChem* **3**, 2031–2035 (2016).
 89. Sheng, T., Xu, Y.-F., Jiang, Y.-X., Huang, L., Tian, N., Zhou, Z.-Y., Broadwell, I. and Sun, S.-G. Structure Design and Performance Tuning of Nanomaterials for Electrochemical Energy Conversion and Storage. *Acc. Chem. Res.* **49**, 2569–2577 (2016).
 90. Mallat, T. and Baiker, A. Potential of Gold Nanoparticles for Oxidation in Fine Chemical Synthesis. *Annu. Rev. Chem. Biomol. Eng.* **3**, 11–28 (2012).
 91. Ghosh, P. C. High platinum cost: obstacle or blessing for commercialization of low-temperature fuel cell technologies. *Clean Technol. Environ. Policy* **19**, 595–601 (2017).
 92. Chen, A. and Holt-Hindle, P. Platinum-based nanostructured materials: Synthesis, properties, and applications. *Chem. Rev.* **110**, 3767–3804 (2010).
 93. Cameron, D. S., Hards, G. a, Harrison, B. and Potter, R. J. Direct Methanol Fuel Cells:

- Recent Developments in the Search for Improved Performance. *Platin. Met. Rev.* **31**, 173–181 (1987).
94. Kim, C. H., Qi, G., Dahlberg, K. and Li, W. Strontium-Doped Perovskites Rival. *Science* **327**, 1624–1627 (2010).
 95. Chhetri, M., Rana, M., Loukya, B., Patil, P. K., Datta, R. and Gautam, U. K. Mechanochemical Synthesis of Free-Standing Platinum Nanosheets and Their Electrocatalytic Properties. *Adv. Mater.* **27**, 4430–4437 (2015).
 96. Rodríguez-López, J., Alpuche-Avilés, M. A. and Bard, A. J. Interrogation of surfaces for the quantification of adsorbed species on electrodes: Oxygen on gold and platinum in neutral media. *J. Am. Chem. Soc.* **130**, 16985–16995 (2008).
 97. Buonaiuto, M., De Crisci, A. G., Jaramillo, T. F. and Waymouth, R. M. Electrooxidation of Alcohols with Electrode-Supported Transfer Hydrogenation Catalysts. *ACS Catal.* **5**, 7343–7349 (2015).
 98. Rudi, S., Gan, L., Cui, C., Gliech, M. and Strasser, P. Electrochemical Dealloying of Bimetallic ORR Nanoparticle Catalysts at Constant Electrode Potentials. *J. Electrochem. Soc.* **162**, F403–F409 (2015).
 99. Yu, Z., Liao, S., Xu, Y., Yang, B. and Yu, D. Hydrogenation of nitroaromatics by polymer-anchored bimetallic palladium-ruthenium and palladium-platinum catalysts under mild conditions. *J. Mol. Catal. A Chem.* **120**, 247–255 (1997).
 100. Calderón Gómez, J., Moliner, R. and Lázaro, M. Palladium-Based Catalysts as Electrodes for Direct Methanol Fuel Cells: A Last Ten Years Review. *Catalysts* **6**, 130 (2016).
 101. Bouazizi, N., Barrimo, D., Nousir, S., Ben Slama, R., Shiao, T. C., Roy, R. and Azzouz, A. Metal-loaded polyol-montmorillonite with improved affinity towards hydrogen. *J. Energy Inst.* **91**, 110–119 (2018).
 102. Antolini, E., Zignani, S. C., Santos, S. F. and Gonzalez, E. R. Palladium-based electrodes: A way to reduce platinum content in polymer electrolyte membrane fuel cells. *Electrochim. Acta* **56**, 2299–2305 (2011).
 103. Fontana, D., Pietrantonio, M., Pucciarmati, S., Torelli, G. N., Bonomi, C. and Masi, F. Palladium recovery from monolithic ceramic capacitors by leaching, solvent extraction and reduction. *J. Mater. Cycles Waste Manag.* **20**, 1–8 (2017).
 104. Von Weber, A. and Anderson, S. L. Electrocatalysis by Mass-Selected Ptn Clusters. *Acc. Chem. Res.* **49**, 2632–2639 (2016).
 105. Gaita, R. and Al-Bazi, S. J. An ion-exchange method for selective separation of palladium, platinum and rhodium from solutions obtained by leaching automotive catalytic converters. *Talanta* **42**, 249–255 (1995).
 106. Hsu, W. H., Jiang, S. J. and Sahayam, A. C. Determination of Pd, Rh, Pt, Au in road dust by electrothermal vaporization inductively coupled plasma mass spectrometry with slurry sampling. *Anal. Chim. Acta* **794**, 15–19 (2013).
 107. Hejral, U., Franz, D., Volkov, S., Francoual, S., Stempfer, J. and Stierle, A. Identification of a Catalytically Highly Active Surface Phase for CO Oxidation over PtRh Nanoparticles under Operando Reaction Conditions. *Phys. Rev. Lett.* **120**, 126101 (2018).
 108. Cook, T. R., McCarthy, B. D., Lutterman, D. A. and Nocera, D. G. Halogen oxidation and halogen photoelimination chemistry of a platinum-rhodium heterobimetallic core. *Inorg. Chem.* **51**, 5152–5163 (2012).
 109. Huo, X., Liu, J. and Strathmann, T. J. Ruthenium catalysts for reduction of N-nitrosamine water contaminants. *Environ. Sci. Technol.* [acs.est.7b05834](https://doi.org/10.1021/acs.est.7b05834) (2018).

doi:10.1021/acs.est.7b05834

110. Zhang, C., Sha, J., Fei, H., Liu, M., Yazdi, S., Zhang, J., Zhong, Q., Zou, X., Zhao, N., Yu, H., Jiang, Z., Ringe, E., Yakobson, B. I., Dong, J., Chen, D. and Tour, J. M. Single-Atomic Ruthenium Catalytic Sites on Nitrogen-Doped Graphene for Oxygen Reduction Reaction in Acidic Medium. *ACS Nano* **11**, 6930–6941 (2017).
111. Moura, A., Fajín, J., Mandado, M. and Cordeiro, M. Ruthenium–Platinum Catalysts and Direct Methanol Fuel Cells (DMFC): A Review of Theoretical and Experimental Breakthroughs. *Catalysts* **7**, 47 (2017).
112. Rudnev, A. V., Zhumaev, U., Utsunomiya, T., Fan, C., Yokota, Y., Fukui, K. I. and Wandlowski, T. Ferrocene-terminated alkanethiol self-assembled monolayers: An electrochemical and in situ surface-enhanced infra-red absorption spectroscopy study. *Electrochim. Acta* **107**, 33–44 (2013).
113. Rudnev, A. V., Yoshida, K. and Wandlowski, T. Electrochemical characterization of self-assembled ferrocene-terminated alkanethiol monolayers on low-index gold single crystal electrodes. *Electrochim. Acta* **87**, 770–778 (2013).
114. Malmos, K., Iruthayaraj, J., Ogaki, R., Kingshott, P., Besenbacher, F., Pedersen, S. U. and Daasbjerg, K. Grafting of thin organic films by electrooxidation of arylhydrazines. *J. Phys. Chem. C* **115**, 13343–13352 (2011).
115. Laforgue, A., Addou, T. and Bélanger, D. Characterization of the deposition of organic molecules at the surface of gold by the electrochemical reduction of aryl diazonium cations. *Langmuir* **21**, 6855–6865 (2005).
116. Oja, S. M., Fan, Y., Armstrong, C. M., Defnet, P. and Zhang, B. Nanoscale Electrochemistry Revisited. *Anal. Chem.* **88**, 414–430 (2016).
117. Parwaiz, M., Lunt, H., Florkowski, C. M., Logan, F. J., Irons, L., Perwick, C., Frampton, C. M. A. and Moore, M. P. Assessment of glucose meter performance at the antenatal diabetes clinic: Exploration of patient-related and pre-analytical factors. *Ann. Clin. Biochem.* **51**, 47–53 (2014).
118. Zhang, S., Wang, N., Yu, H., Niu, Y. and Sun, C. Covalent attachment of glucose oxidase to an Au electrode modified with gold nanoparticles for use as glucose biosensor. *Bioelectrochemistry* **67**, 15–22 (2005).
119. Sun, Y., Bai, Y., Yang, W. and Sun, C. Controlled multilayer films of sulfonate-capped gold nanoparticles/thionine used for construction of a reagentless bienzymatic glucose biosensor. *Electrochim. Acta* **52**, 7352–7361 (2007).
120. Wu, N. Y., Gao, W., He, X. L., Chang, Z. and Xu, M. T. Direct electrochemical sensor for label-free DNA detection based on zero current potentiometry. *Biosens. Bioelectron.* **39**, 210–214 (2013).
121. Rashid, J. I. A. and Yusof, N. A. The strategies of DNA immobilization and hybridization detection mechanism in the construction of electrochemical DNA sensor: A review. *Sens. Bio-Sensing Res.* **16**, 19–31 (2017).
122. Hwang, S., Kim, E. and Kwak, J. Electrochemical detection of DNA hybridization using biometallization. *Anal. Chem.* **77**, 579–584 (2005).
123. Ida, O. and Ida, C. Electrochemical Signal Amplification for Immunosensor Based on 3D Interdigitated Array Electrodes. 2014–2015 (2014).
124. Nassef, H. M., Bermudo Redondo, M. C., Ciclitira, P. J., Ellis, H. J., Fragoso, A. and O’Sullivan, C. K. Electrochemical immunosensor for detection of celiac disease toxic gliadin in foodstuff. *Anal. Chem.* **80**, 9265–9271 (2008).

125. Pisoschi, A. M., Pop, A., Serban, A. I. and Fafaneata, C. Electrochemical methods for ascorbic acid determination. *Electrochim. Acta* **121**, 443–460 (2014).
126. Shyu, K. G., Chang, C. C., Yeh, Y. C., Sheu, J. R. and Chou, D. S. Mechanisms of ascorbyl radical formation in human platelet-rich plasma. *Biomed Res. Int.* **2014**, (2014).
127. Du, J., Cullen, J. J. and Buettner, G. R. Ascorbic acid: Chemistry, biology and the treatment of cancer. *Biochim. Biophys. Acta - Rev. Cancer* **1826**, 443–457 (2012).
128. Padayatty, S. J., Katz, a, Wang, Y., Eck, P., Kwon, O., Lee, J. H., Chen, S., Corpe, C., Dutta, a, Dutta, S. K. and Levine, M. Vitamin C as an Antioxidant : Evaluation of Its Role in Disease Prevention. *J. Am. Coll. Nutr.* **22**, 18–35 (2013).
129. Kuwana, D. T. Ascorbic Acid (Vitamin C): A Cyclic Voltammetric Study of its Oxidation at a Glassy Carbon Electrode. *Anal. Electrochem. A Lab. Man.* 3–7
130. Brezina, M., Koryta, J., Loucka, T., Marsikova, D. and Pradac, J. Adsorption and Kinetics of Oxidation of Ascorbic Acid At Platinum Electrodes. *J. Electroanal. Chem. Interfacial Electrochem.* **40**, 13–17 (1972).
131. Thiagarajan, S. and Chen, S.-M. Preparation and characterization of PtAu hybrid film modified electrodes and their use in simultaneous determination of dopamine, ascorbic acid and uric acid. *Talanta* **74**, 212–222 (2007).
132. Nimse, S. B. and Pal, D. Free radicals, natural antioxidants, and their reaction mechanisms. *RSC Adv.* **5**, 27986–28006 (2015).
133. Grunwell, J. R., Gillespie, S. E., Ward, J. M., Fitzpatrick, A. M., Brown, L. A., Gauthier, T. W. and Hebbar, K. B. Comparison of Glutathione, Cysteine, and Their Redox Potentials in the Plasma of Critically Ill and Healthy Children. *Front. Pediatr.* **3**, 3–8 (2015).
134. Spătaru, N., Sarada, B. V., Popa, E., Tryk, D. A. and Fujishima, A. Voltammetric determination of L-cysteine at conductive diamond electrodes. *Anal. Chem.* **73**, 514–519 (2001).
135. Zare, H. R., Jahangiri-Dehaghani, F., Shekari, Z. and Benvidi, A. Electrocatalytic simultaneous determination of ascorbic acid, uric acid and l-Cysteine in real samples using quercetin silver nanoparticles-graphene nanosheets modified glassy carbon electrode. *Appl. Surf. Sci.* **375**, 169–178 (2016).
136. Sudeep, P. K., Joseph, S. T. S. and Thomas, K. G. Selective detection of cysteine and glutathione using gold nanorods. *J. Am. Chem. Soc.* **127**, 6516–6517 (2005).
137. Xu, H. and Hepel, M. ‘Molecular beacon’-based fluorescent assay for selective detection of glutathione and cysteine. *Anal. Chem.* **83**, 813–819 (2011).
138. Ralph, T. R., Hitchman, M. L., Millington, J. P. and Walsh, F. C. The electrochemistry of l-cystine and l-cysteine. Part 1: Thermodynamic and kinetic studies. *J. Electroanal. Chem.* **375**, 1–15 (1994).
139. Sautin, Y. Y. and Johnson, R. J. Uric Acid: The Oxidant-Antioxidant Paradox. *Nucleosides Nucleotides Nucleic Acids* **27**, 608–619 (2008).
140. Chen, J. C., Chung, H. H., Hsu, C. T., Tsai, D. M., Kumar, a S. and Zen, J. M. A disposable single-use electrochemical sensor for the detection of uric acid in human whole blood. *Sensors and Actuators B-Chemical* **110**, 364–369 (2005).
141. Du, J., Yue, R., Ren, F., Yao, Z., Jiang, F., Yang, P. and Du, Y. Novel graphene flowers modified carbon fibers for simultaneous determination of ascorbic acid, dopamine and uric acid. *Biosens. Bioelectron.* **53**, 220–224 (2014).
142. Wang, C., Du, J., Wang, H., Zou, C., Jiang, F., Yang, P. and Du, Y. A facile

- electrochemical sensor based on reduced graphene oxide and Au nanoplates modified glassy carbon electrode for simultaneous detection of ascorbic acid, dopamine and uric acid. *Sensors Actuators, B Chem.* **204**, 302–309 (2014).
143. Hu, G., Ma, Y., Guo, Y. and Shao, S. Electrocatalytic oxidation and simultaneous determination of uric acid and ascorbic acid on the gold nanoparticles-modified glassy carbon electrode. *Electrochimica Acta* **53**, 6610–6615 (2008).
 144. Samanta, D. and Sarkar, A. Immobilization of bio-macromolecules on self-assembled monolayers: methods and sensor applications. *Chem. Soc. Rev.* **40**, 2567 (2011).
 145. Klocke, A., Von Stetten, F., Zengerle, R. and Kerzenmacher, S. Strategies for the fabrication of porous platinum electrodes. *Adv. Mater.* **23**, 4976–5008 (2011).
 146. Habrioux, A., Sibert, E., Servat, K., Vogel, W., Kokoh, K. B. and Alonso-Vante, N. Activity of platinum-gold alloys for glucose electrooxidation in biofuel cells. *J. Phys. Chem. B* **111**, 10329–10333 (2007).
 147. Qiu, H. and Huang, X. Effects of Pt decoration on the electrocatalytic activity of nanoporous gold electrode toward glucose and its potential application for constructing a nonenzymatic glucose sensor. *J. Electroanal. Chem.* **643**, 39–45 (2010).
 148. Kang, X., Mai, Z., Zou, X., Cai, P. and Mo, J. A novel glucose biosensor based on immobilization of glucose oxidase in chitosan on a glassy carbon electrode modified with gold-platinum alloy nanoparticles/multiwall carbon nanotubes. *Anal. Biochem.* **369**, 71–79 (2007).
 149. Chou, C. H., Chen, J. C., Tai, C. C., Sun, I. W. and Zen, J. M. A nonenzymatic glucose sensor using nanoporous platinum electrodes prepared by electrochemical alloying/dealloying in a water-insensitive zinc chloride-1-ethyl-3-methylimidazolium chloride ionic liquid. *Electroanalysis* **20**, 771–775 (2008).
 150. Ma, D., Tang, X., Guo, M., Lu, H. and Xu, X. Fabrication and characterization of non-enzymatic glucose sensor based on bimetallic hollow Ag/Pt nanoparticles prepared by galvanic replacement reaction. *Ionics (Kiel)*. 1417–1426 (2014). doi:10.1007/s11581-014-1290-1
 151. Park, S., Boo, H. and Chung, T. D. Electrochemical non-enzymatic glucose sensors. *Anal. Chim. Acta* **556**, 46–57 (2006).
 152. Toghiani, K. E. and Compton, R. G. Electrochemical non-enzymatic glucose sensors: A perspective and an evaluation. *Int. J. Electrochem. Sci.* **5**, 1246–1301 (2010).
 153. Wen, Y., Liu, K., Yang, H., Liu, Y., Chen, L., Liu, Z., Huang, C. and Yi, T. Mitochondria-Directed Fluorescent Probe for the Detection of Hydrogen Peroxide near Mitochondrial DNA. *Anal. Chem.* **87**, 10579–10584 (2015).
 154. Yan, Z., Zhao, J., Qin, L., Mu, F., Wang, P. and Feng, X. Non-enzymatic hydrogen peroxide sensor based on a gold electrode modified with granular cuprous oxide nanowires. *Microchim. Acta* **180**, 145–150 (2012).
 155. Meng, F., Yan, X., Liu, J., Gu, J. and Zou, Z. Nanoporous gold as non-enzymatic sensor for hydrogen peroxide. *Electrochim. Acta* **56**, 4657–4662 (2011).
 156. Li, H., Li, Q., Wang, X., Xu, K., Chen, Z., Gong, X., Liu, X., Tong, L. and Tang, B. Simultaneous determination of superoxide and hydrogen peroxide in macrophage RAW 264.7 cell extracts by microchip electrophoresis with laser-induced fluorescence detection. *Anal. Chem.* **81**, 2193–2198 (2009).
 157. Wang, Y., Chen, K. S., Mishler, J., Cho, S. C. and Adroher, X. C. A review of polymer electrolyte membrane fuel cells: Technology, applications, and needs on fundamental

- research. *Appl. Energy* **88**, 981–1007 (2011).
158. Shioyama, H. Carbon Materials used for Polymer Electrolyte Fuel Cells. in *Handbook of Advanced Ceramics: Materials, Applications, Processing, and Properties* 199–210 (2013). doi:10.1016/B978-0-12-385469-8.00012-5
 159. Ferreira Frota, E., Silva de Barros, V. V., de Araújo, B. R. S., Gonzaga Purgatto, Â. and Linares, J. J. Pt/C containing different platinum loadings for use as electrocatalysts in alkaline PBI-based direct glycerol fuel cells. *Int. J. Hydrogen Energy* **42**, 23095–23106 (2017).
 160. Desai, S., Brown, G. and Bollepalli, S. PEM Fuel Cell Catalysts: Cost, Performance, and Durability. *Interface* **14**, 41–46 (2005).
 161. Lin, B. Y. S., Kirk, D. W. and Thorpe, S. J. Performance of alkaline fuel cells: A possible future energy system? *J. Power Sources* **161**, 474–483 (2006).
 162. Aricò, A. S., Srinivasan, S. and Antonucci, V. DMFCs: From Fundamental Aspects to Technology Development. *Fuel Cells* **1**, 133–161 (2001).
 163. Niakolas, D. K., Daletou, M., Neophytides, S. G. and Vayenas, C. G. Fuel cells are a commercially viable alternative for the production of ‘clean’ energy. *Ambio* **45**, 32–37 (2016).
 164. Kawase, M. Manufacturing method for tubular molten carbonate fuel cells and basic cell performance. *J. Power Sources* **285**, 260–265 (2015).
 165. Monaco, A. and Di Matteo, U. Life cycle analysis and cost of a molten carbonate fuel cell prototype. *Int. J. Hydrogen Energy* **36**, 8103–8111 (2011).
 166. Lewis, J. Stationary fuel cells - Insights into commercialisation. *Int. J. Hydrogen Energy* **39**, 21896–21901 (2014).
 167. Liao, T., Cai, L., Zhao, Y. and Chen, J. Efficiently exploiting the waste heat in solid oxide fuel cell by means of thermophotovoltaic cell. *J. Power Sources* **306**, 666–673 (2016).
 168. Stambouli, A. B. and Traversa, E. Solid oxide fuel cells (SOFCs): A review of an environmentally clean and efficient source of energy. *Renew. Sustain. Energy Rev.* **6**, 433–455 (2002).
 169. Sheikh, A. M., Ebn-Alwaled Abd-Alftah, K. and Malfatti, C. F. On reviewing the catalyst materials for direct alcohol fuel cells (DAFCs). *J. Multidiscip. Eng. Sci. Technol.* **1**, 3159–40 (2014).
 170. Joghee, P., Malik, J. N., Pylypenko, S. and O’Hayre, R. A review on direct methanol fuel cells – In the perspective of energy and sustainability. *MRS Energy Sustain.* **2**, E3 (2015).
 171. Ren, X., Zelenay, P., Thomas, S., Davey, J. and Gottesfeld, S. Recent advances in direct methanol fuel cells at Los Alamos National Laboratory. *J. Power Sources* **86**, 111–116 (2000).
 172. Liu, H., Song, C., Zhang, L., Zhang, J., Wang, H. and Wilkinson, D. P. A review of anode catalysis in the direct methanol fuel cell. *J. Power Sources* **155**, 95–110 (2006).
 173. Lu, G. Q. and Wang, C. Y. Development of micro direct methanol fuel cells for high power applications. *J. Power Sources* **144**, 141–145 (2005).
 174. Wasmus, S. and Küver, A. Methanol oxidation and direct methanol fuel cells: a selective review. *J. Electroanal. Chem.* **461**, 14–31 (1999).
 175. El-Nagar, G. A., Hassan, M. A., Lauermann, I. and Roth, C. Efficient Direct Formic Acid Fuel Cells (DFAFCs) Anode Derived from Seafood waste: Migration Mechanism. *Sci. Rep.* **7**, 1–11 (2017).
 176. Akhairi, M. a. F. and Kamarudin, S. K. Catalysts in direct ethanol fuel cell (DEFC): An

- overview. *Int. J. Hydrogen Energy* **41**, 4214–4228 (2016).
177. Ralph, T. R. and Hogarth, M. P. Catalysis for Low Temperature Fuel Cells. *Reading* **46**, 117–135 (2002).
 178. Dillon, R., Srinivasan, S., Aricò, A. S. and Antonucci, V. International activities in DMFC RandD: Status of technologies and potential applications. *J. Power Sources* **127**, 112–126 (2004).
 179. Universit, J. L. Direct Methanol Fuel Cells: From a Twentieth Century Electrochemist's Dream to a Twenty-first Century Emerging Technology. in *Modern Aspects of Electrochemistry No. 34* (eds. Bockris, J. O., Conway, B. E. and White, R. E.) 119–204 (Kluwer Academic Publishers, 2002). doi:10.1007/0-306-46923-5
 180. Hamnett, A. Mechanism and electrocatalysis in the direct methanol fuel cell. *Catal. Today* **38**, 445–457 (1997).
 181. Kamarudin, M. Z. F., Kamarudin, S. K., Masdar, M. S. and Daud, W. R. W. Review: Direct ethanol fuel cells. *Int. J. Hydrogen Energy* **38**, 9438–9453 (2013).
 182. Wang, K., Zhang, J., Tang, L., Zhang, H., Zhang, G., Yang, X., Liu, P. and Mao, Z. Establishment and assessment of a novel cleaner production process of corn grain fuel ethanol. *Bioresour. Technol.* **148**, 453–460 (2013).
 183. Wongyao, N., Therdthianwong, A. and Therdthianwong, S. Performance of direct alcohol fuel cells fed with mixed methanol/ethanol solutions. *Energy Convers. Manag.* **52**, 2676–2681 (2011).
 184. Saisirirat, P. and Joommanee, B. Study on the Performance of the Micro Direct Ethanol Fuel Cell (Micro-DEFC) for Applying with the Portable Electronic Devices. *Energy Procedia* **138**, 187–192 (2017).

Chapter 2

Instrumentation and Characterization

2.1. Introduction

The fabrication and characterization of nanomaterials is of critical importance in any field of chemistry due to the effect the structure of these materials has on their activity. The work presented in the following chapters use a variety of electrochemical techniques in order to fabricate and characterize a series of nanoporous gold electrodes including voltammetry, amperometry, and potentiometry. Additionally, instrumental methods are used to characterize the surface topology as well as surface composition of these electrodes. The following chapter serves as a brief introduction to each of these methods.

2.2. Electrochemistry

The field of electrochemistry focuses around the study of the flow of electrons to and from the active surface of an electrode and the molecules present in a solution. The loss of electrons is known as oxidation and the gain of electrons is known as reduction as shown in **Equation 2.1**. An oxidized molecule can gain an electron to form its reduced form. This



exchange of electrons is the basis for all electrochemistry. Electrochemical measurements and techniques can be accomplished using either a two- or three-electrode experimental setup. In this work, we utilize a two-electrode set up for potentiometry experiments (see below). The electrochemical cell contains two electrodes: a working or indicator electrode and a reference electrode. These electrodes are placed in the same solution (**Fig. 2.1a**). The difference in potential between the working and reference electrode is measured under conditions of zero current flow. In a three-electrode system, the working and reference electrodes are placed in a

solution along with a third electrode, called an auxiliary or counter electrode (AE) (**Fig. 2.1b**). We utilize a three-electrode system for cyclic voltammetry experiments (see below). A change in potential at the WE can cause a loss or gain of electrons (oxidation or reduction) resulting in current flow. In order to prevent current from flowing from the WE to the RE, the AE is used to

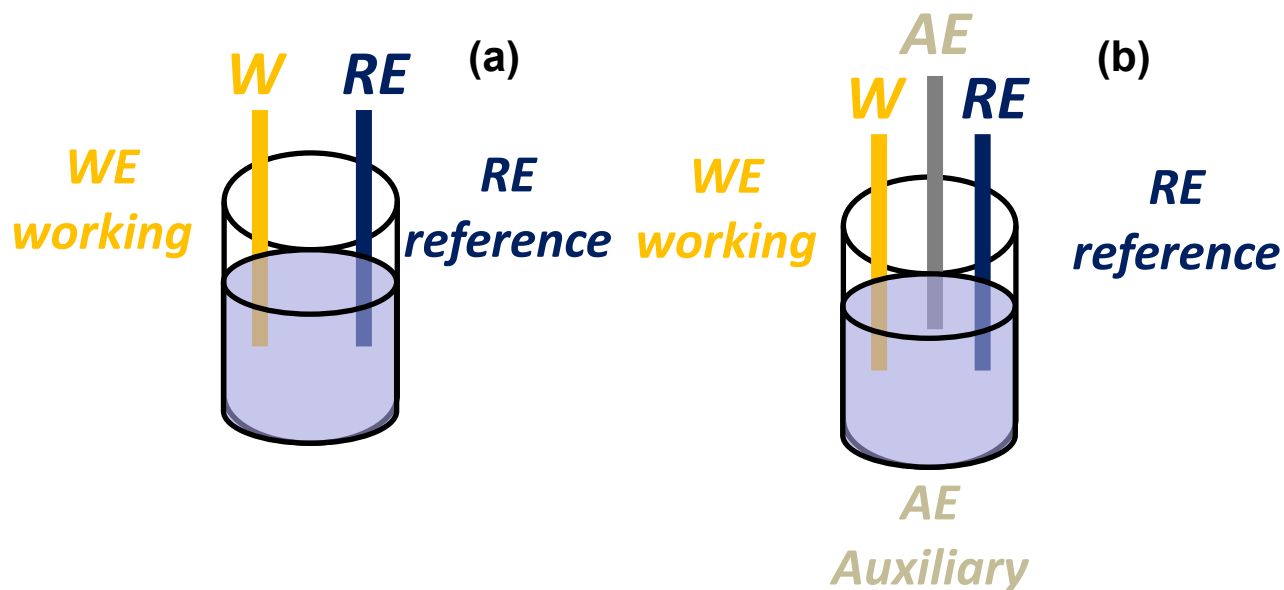


Figure 2.1. Cartoon representation of a standard (a) two-electrode and (b) three-electrode electrochemical cell with working electrode (**WE**), reference electrode (**RE**) and auxiliary electrode (**AE**).

close the circuit and is the source of the opposite redox reaction to that of the WE.

2.2.1. Cyclic Voltammetry

Cyclic voltammetry (CV) is a very popular electroanalytical technique that is used extensively.¹⁻³ In a typical CV experiment the voltage applied to the working electrode is changed, whether positively or negatively, over time from an initial potential (E_i) to a certain point (E_f) at which time the potential reverses direction back to the initial potential (**Fig. 2.2a**). In a solution that lacks redox active molecules (only electrolyte), only non-Faradaic current flows,

and the resultant CV has a rectangular shape. The current measured is the charging current that flows due to the restructuring of the double layer region at the electrode solution interface. The electrode behaves as a capacitor because no electrons are being transferred. Plotting the non-Faradaic charging current (i_c) versus scan rate (v) can be used to find the double layer capacitance (C_{dl}) if the electrode area (A) is known (**Eq. 2.2**).

$$i_c = A C_{dl} v \quad (2.2)$$

When a redox active molecule is present as a diffusing species in solution, the shape of the CV curve is very different (**Fig. 2.2b**). Typically, a peak(s) can be observed near the point at which the redox species is reduced and oxidized. In **Fig 2.2b**, a change in current for the forward, anodic scan (when oxidation occurs) and the reverse, cathodic scan (when reduction occurs) is seen. The forward and reverse peaks shown in the figure represent the reversible

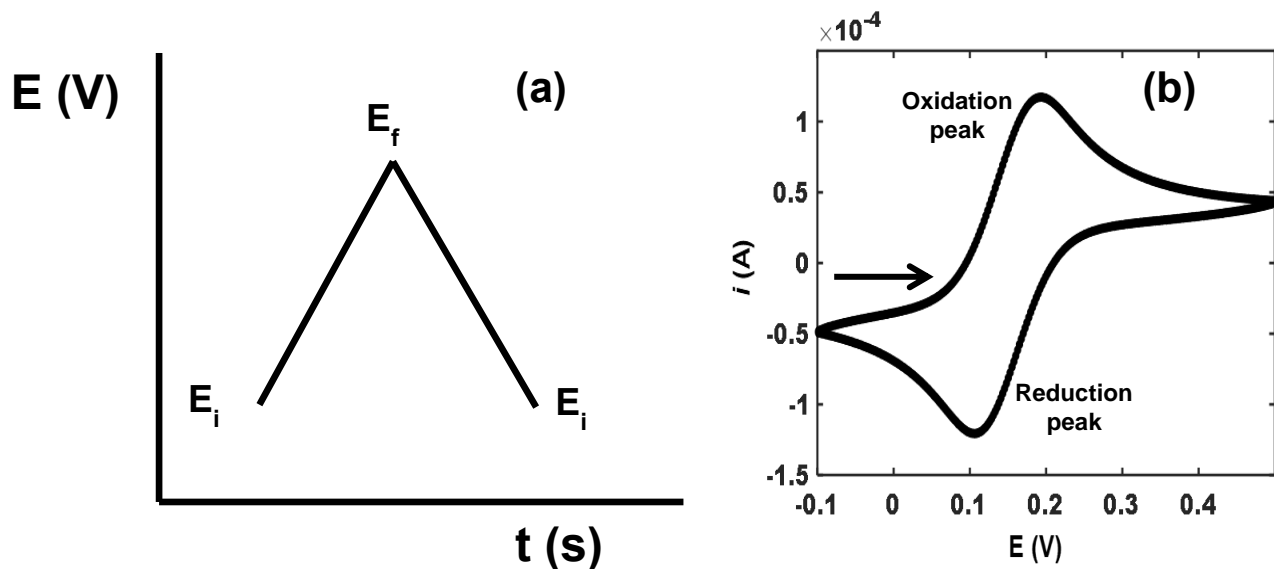


Figure 2.2. (a) Waveform for cyclic voltammetry showing the potential change from the initial potential (E_i) to a final potential (E_f) and back to initial. (b) Corresponding voltammogram of the forward, anodic scan and the reverse, cathodic scan of an ideal reversible redox reaction where E is the potential in volts and i is current in amps. Arrow denotes scan direction.

oxidation and subsequent reduction of a redox molecule that can undergo one-electron transfer. The difference in peak potential between the two peaks (ΔE_{peak}) is an indicator of the reversibility of the redox molecule. If the difference in the potentials is $59.2 \text{ mV} / n$, where n is the number of electrons transferred, then the redox reaction is said to be reversible. For an irreversible reaction, only one peak (oxidation or reduction) will be seen and a quasi-reversible reaction will show a larger ($> 59.2 \text{ mV} / n$) difference in peak potentials.^{3,4}

When the redox species is adsorbed to the electrode, the CV curve is very different from that observed for a diffusing species. Instead of a peak shaped, the CV is typically symmetrical and Gaussian shaped. For a reversible, well-behaved redox system, the peak separation (ΔE_{peak}) is equal to zero. A plot of peak current vs. scan rate will be linear in contrast to that obtained for a diffusing system where the peak current is proportional to the square root of scan rate (for an electrochemically reversible redox system).

The formation of gold oxide on the surface of a gold electrode has been exploited to provide valuable electrode information. When immersed in $0.5 \text{ M H}_2\text{SO}_4$, the potential is swept in the positive direction producing a monolayer of oxide on the gold surface. The subsequent negative sweep reduces the gold oxide (**Fig. 2.3a**) and the area beneath the curve represents the charge (Coulombs) passed over the electrode.² Since the oxide that formed was a monolayer, the charge is proportional to the electrode surface area (cm^2). Using the standard charge per unit area of crystalline gold of $390 \text{ } \mu\text{C}/\text{cm}^2$, the charge can be converted to indicate the electroactive surface area (EASA) of gold.⁵ Platinum, on the other hand does not form an oxide, but instead adsorbs hydrogen. Similar to gold oxide formation, a monolayer of hydrogen adsorbs to the platinum electrode surface during the anodic sweep and the desorption of this monolayer occurs in the subsequent cathodic sweep.² The area under the curve (**Fig. 2.3b**) can be converted to

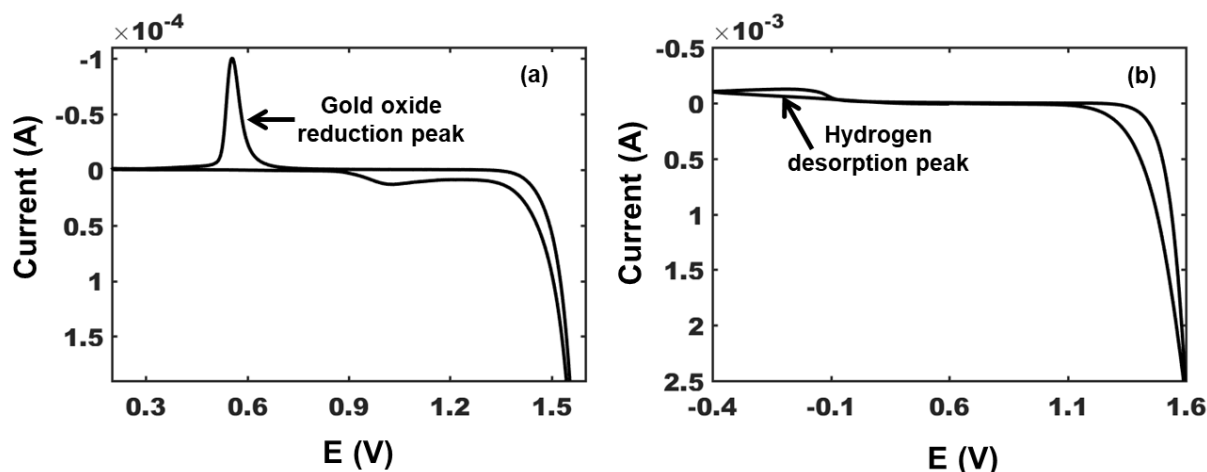


Figure 2.3. Cyclic voltammetry used to determine the electroactive surface area (EASA) of electrodes using (a) reduction of gold oxide peak and (b) desorption of hydrogen on platinum. The area under the curve represents the charge passed over the electrode and can be converted to area using the standard charge per unit area for gold ($390 \mu\text{C}/\text{cm}^2$) and platinum ($210 \mu\text{C}/\text{cm}^2$), respectively.

electroactive surface area of platinum from the integrated charge of the hydrogen desorption peak ($210 \mu\text{C}/\text{cm}^2$).⁶

2.2.2. Chronoamperometry

Chronoamperometry is also a method that uses potential to induce the flow of current. However, instead of changing the potential linearly with time, the potential is stepped and held at a constant value for either oxidation or reduction to take place while the current is measured. **Figure 2.4** denotes the potential being held at an initial potential (a) and the resultant change in current over time. Depending on the redox molecule in solution along with the applied potential, the current can flow either to or from the electrode. When electrons are transferred across the electrode-solution interface causing oxidation or reduction, the process is said to be Faradaic. Alternatively, a non-Faradaic process occurs when charge does not cross the interface, but external current can flow when potential, electrode area, or solution composition changes. The

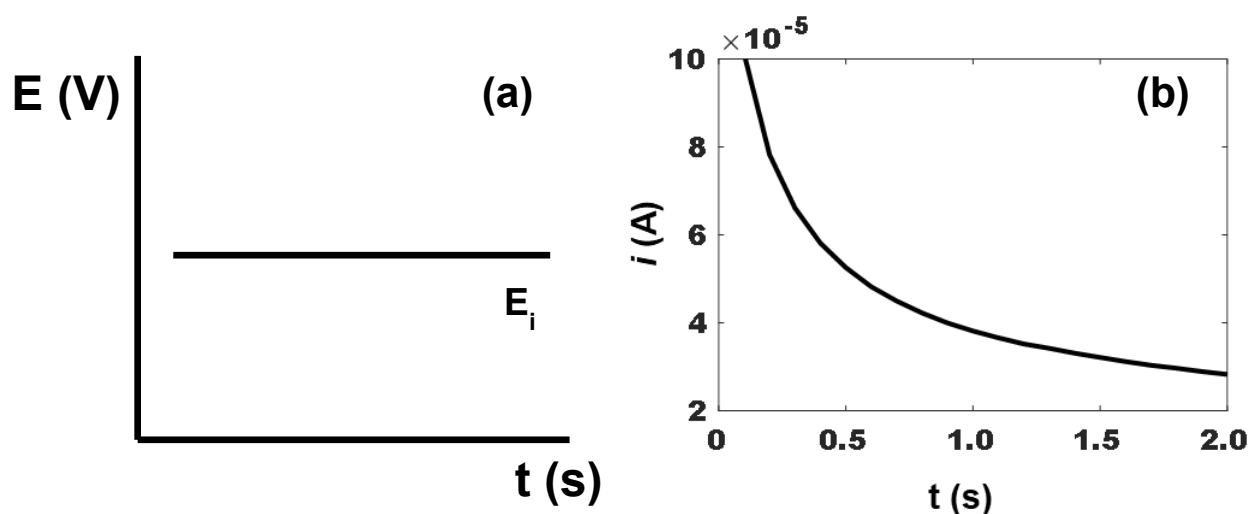


Figure 2.4. (a) Waveform for chronoamperometry showing no change in the potential from the initial potential (E_i). (b) Corresponding response of current over time.

non-Faradaic current decreases exponentially with time while the Faradaic current decays with respect to the square root of time. The Faradaic current is initially large and drops as the redox species in solution is oxidized or reduced. The rapid oxidation or reduction occurs faster than the molecules can diffuse from bulk solution to the electrode surface. As the concentration is reduced, so does the current required to maintain the oxidized or reduced state of the molecules at the surface. In this work, chronoamperometry is used as an electrodeposition technique. A negative potential is applied to the working electrode and held for a very short period. A metal salt in solution is reduced to form metal on the electrode surface. To limit the amount of deposition, low concentrations of the metal salt was used along with a short period of electrodeposition.

2.2.3. Potentiometry

Potentiometry is the measurement of the potential over time in the absence of current flow. In the present work, the open-circuit or rest potential (OCP) of the electrode is measured

under potentiometric conditions (no current flow). Unlike CV and chronoamperometry, which induce either an oxidation or a reduction reaction, the measuring of OCP is a passive technique where the concentration does not change because there is no external potential guiding electron exchange. A way in which to relate the measured potential to the concentration is through the Nernst equation (**Eq. 2.3**), where E is the measured potential (with respect to a reference), E^0 is

$$E = E^0 - \left(\frac{RT}{nF} \right) \ln \left(\frac{C_{\text{Red}}}{C_{\text{Ox}}} \right) \quad (2.3)$$

the standard reduction potential of the redox couple, R is the gas constant, F is Faraday's constant, n is the number of electrons transferred, and C_{Red} and C_{Ox} are the concentrations of the reduced and oxidized forms of the redox pair, respectively.⁴ A change in the concentration of a redox molecule will elicit a change in potential. A Nernst plot is obtained by plotting potential vs log of the ratio of the reduced/oxidized species in solution. At 25 °C, the slope of the linear fit should equal 59.2 mV over number of electrons transferred (n). The y-intercept should reflect the redox potential of the redox system. In a one-electron transfer system, the expected slope would equal 59.2 mV. A significant deviation from this value can suggest an issue with electrode fabrication, electrode passivation, and/or a decrease in electrode sensitivity. This technique is used extensively in this work and more detail will be provided as the data is presented.

2.3. Scanning Electron Microscopy

In order to characterize nanomaterials, scanning electron microscopy (SEM) is of vital importance. This technique has the ability to resolve images in the nanoscale, which can provide information about the surface of a material. An electron gun produces a beam of electrons that will interact with the surface of a sample and provide topographic data based on how the

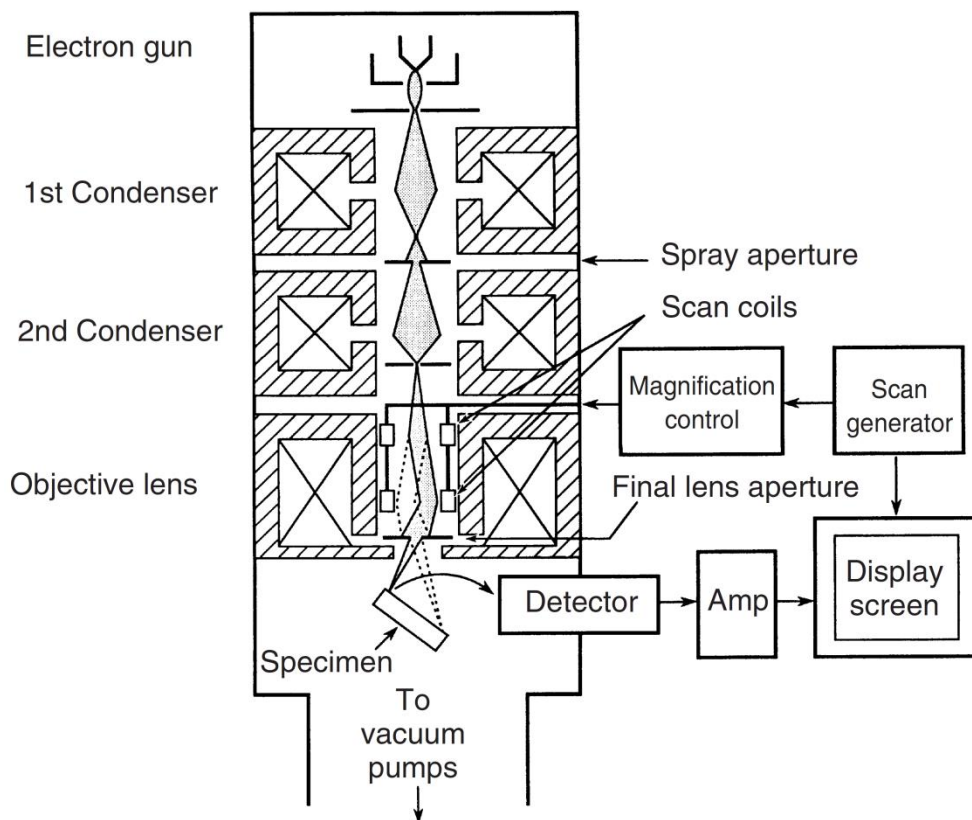


Figure 2.5. Structure of a scanning electron microscope (SEM). Reprinted with permission from ref. 7.

electrons bounce off the sample. The beam travels through a series of condenser lenses to focus the electrons to reduce the crossover diameter. The objective lens is used to concentrate the electrons into a probe that can interact with a sample (**Fig. 2.5**). The sample is scanned line-by-line, where electrons that are emitted from the sample are detected and used to recreate the image. The deflection of electrons provides information of composition and topography.

Two main types of electrons that are emitted from the sample and are essential to SEM imaging are back-scattered electrons (BSE) and secondary electrons (SE). BSEs are produced via elastic scattering after electrons contact the sample. Electrons are scattered by the different atoms making up a sample and heavier atoms will develop as lighter regions in the image than do

lighter atoms allowing the visualization of contrast. Since these electrons are incident electrons that originate from the electron gun, they have a high energy and have large angles of deflection. Alternatively, inelastic scattering is responsible for producing SEs. These electrons have a much lower energy and generally have smaller angles of deflection due to the electrons originating from sample atoms and not the incident SEM beam like BSEs. Elastic scattering does not transfer kinetic energy from the incident electrons to those in sample atoms, which is responsible for the higher energy of these electrons. SEs come from a kinetic energy transfer from the incident beam to sample electrons. Both BSEs and SEs travel to the detector and the electrons are accelerated by a scintillator converting the electrons into photons, which then travel through a photomultiplier tube (PMT) to amplify the signal in order to produce an image. The angles of deflection of SEs and how they are received by the detector is used to display the contours of the sample surface.^{7,8} **Figure 2.6** shows the distribution of BSEs and SEs as well as how deep the

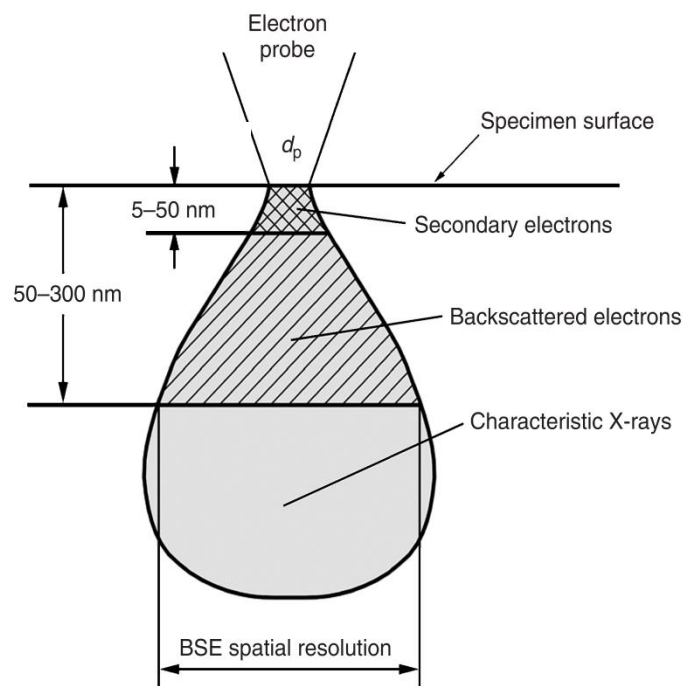


Figure 2.6. The interaction zone of electrons and specimen atoms below a specimen surface. Adapted from ref. 7.

incident electrons travel in the sample. The X-rays that are also produced can be used in Energy-Dispersive X-ray Spectroscopy (EDS) to shed light on bulk composition of a sample; however, this technique was not used in this work.

2.4. X-ray Photoelectron Spectroscopy

After acquiring topographical data on a sample, it is important to determine the composition of the sample as well. The use of X-ray Photoelectron Spectroscopy (XPS) allows for the compositional analysis of a sample down through the top layers, 3-10 nm. XPS uses a similar method to SEM in that a sample interacts with an incident beam and these interactions can be used to elucidate surface information. Under a very high vacuum, monochromatic X-rays ($\text{Al K}\alpha$) are directed towards a sample. An X-ray then transfers energy to a core-level electron

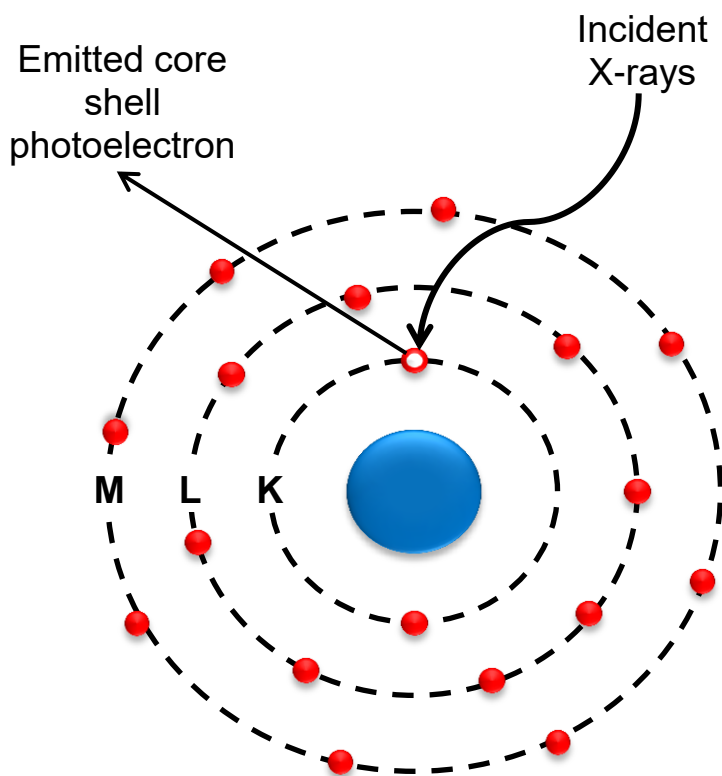


Figure 2.7. Cartoon representation of the excitation of emitted core shell photoelectrons due to kinetic energy transfer from incident X-rays.

and, if it has gained enough kinetic energy, it is ejected (**Fig. 2.7**). The kinetic energy of this photoelectron will depend on the incident beam as well as the binding energy of the electron. Binding energies (E_{binding}) are calculated using the difference in the energy of incident photon (E_{photon}), the kinetic energy of the ejected photoelectron (E_{kinetic}), and a work function (W) for the concentric hemispherical electron energy analyzer (CHA) specific to the instrument that

$$E_{\text{binding}} = E_{\text{photon}} - E_{\text{kinetic}} - W \quad (2.4)$$

calculates E_{kinetic} . This relationship is shown in **Equation. 2.4**.⁹ The calculated E_{binding} for a sample is what allows for the identification of atom type, state, and composition.

Once a spectrum is obtained, each peak is identified using their respective binding energies. A shift in the binding energy of a type of atom from the standard is suggestive of a change in chemical state, like the formation of metal oxides, on the sample surface. When comparing samples with multiple metals, a shift in the binding energy can be seen depending on the percent composition of each metal as well as the structure. Additionally, compositional information is determined with the use of relative sensitivity factors (RSF). These are used scale the measured peak area of the identified peaks. Peak analysis software, such as CASA or Advantage, contains RSF libraries for elemental peaks. The area of each element peak is then converted into a percentage of the element on the sample surface.

2.5. References

1. Wipf, D. O., Kristensen, E. W., Deakin, M. R. and Wightman, R. M. Fast-scan cyclic voltammetry as a method to measure rapid heterogeneous electron-transfer kinetics. *Anal. Chem.* **60**, 306–310 (1988).
2. Hoare, J. P. A Cyclic Voltammetric Study of the Gold-Oxygen System. *J. Electrochem. Soc.* **131**, 1808–1815 (1984).
3. Ching, S., Dudek, R. and Tabet, E. Cyclic Voltammetry with Ultramicroelectrodes. *J. Chem. Educ.* **71**, 602 (1994).
4. Bard, A. J. and Faulkner, L. R. *Electrochemical Methods: Fundamentals and Applications*. (John Wiley and Sons, Inc., 1980).
5. Siepenkoetter, T., Salaj-Kosla, U., Xiao, X., Belochapkin, S. and Magner, E. Nanoporous Gold Electrodes with Tuneable Pore Sizes for Bioelectrochemical Applications. *Electroanalysis* **28**, 2415–2423 (2016).
6. Miller, T. S., Macpherson, J. V. and Unwin, P. R. Dual-electrode measurements in a meniscus microcapillary electrochemical cell using a high aspect ratio carbon fibre ultramicroelectrode. *J. Electroanal. Chem.* **729**, 80–86 (2014).
7. Leng, Y. Scanning Electron Microscopy. in *Materials Characterization* 127–161 (Wiley, 2013).
8. Reimschuessel, A. C. Scanning Electron Microscopy-part 1. *Chem. Instrum.* **49**, A413–A419 (1972).
9. Bell, D. and Garratt-Reed, A. *Energy Dispersive X-ray Analysis in the Electron Microscope*. (Garland Science, 2003).

Chapter 3

Electrochemical Comparison of Nanoporous Gold (NPG) to Planar Gold (PG) in the Presence of Biofouling Solutions

Reproduced with permission from *J. Electrochem. Soc.*, **163**(4), H3083–H3087. Copyright 2016. The Electrochemical Society.¹

3.1. Introduction

Potentiometry is a technologically simple and inexpensive approach to obtain important information about the redox state of a system and/or the concentration of ions in solution.^{2,3} The measurement itself is simple in that all that is needed is a high impedance voltmeter, a stable reference electrode, and a suitable indicating electrode. In contrast to voltammetric measurements, no current flows, and the concentration of the redox species in solution does not change nor does the indicating electrode surface become altered as a potential is not applied. The most popular potentiometric measurement is the measurement of pH using an ion-selective electrode that incorporates a thin membrane responsive to the activity of protons in solution.⁴

For the work described herein, the indicating electrode is an inert metallic redox electrode that is purposely designed to be *nonselective* and will ‘ideally’ respond to all redox active species in solution able to exchange electrons with the metallic surface.^{2, 3} When the indicator electrode is immersed in solution, it will equilibrate electrochemically with the dissolved redox species and a potential will develop at its surface. The measured potential is governed by factors such as (1) the redox species present, (2) their concentrations (activities), and (3) the rate of electron exchange with the electrode.^{3, 5, 6} Such redox measurements have been used to characterize the redox state of solutions with a complex matrix including milk, cheese, sludge, water and biological systems.⁷⁻¹⁴

An important and often neglected factor in the measurement of redox potential is the nature of the electrode surface, particularly the presence and extent of modification, contamination, and fouling/poisoning, as these variables can significantly reduce electron exchange rates. Natural systems, which often contain many redox species with varying electron exchange rates, are particularly challenging to study^{5, 15} It is possible that the measured redox

potential is governed by one species, particularly if its concentration and electron exchange rate is significantly higher than other species present in solution.^{6, 15} To increase the quantitative usefulness of redox potential measurements in complex environments, it's necessary to design electrodes that will minimize the impact of contamination on the electrode response and facilitate electron exchange with as many redox species as possible.³

In this work, we closely examined two electrodes - planar gold and nanoporous gold¹⁶⁻¹⁸ and evaluated their potentiometric redox response in solutions of increasing biological complexity. Nanoporous gold (NPG), in particular, has been shown to minimize the effect of biofouling on an electrochemical response via a biosieving-like mechanism¹⁹⁻²¹ and facilitate charge transfer via nanoconfinement.²² In this work, the potentiometric response of nanoporous and planar gold electrodes previously exposed to a known biofouling agent was examined. First, a solution containing low concentrations of both forms of a redox couple with relatively fast electron transfer kinetics was studied. These experiments were then followed by experiments using a biologically relevant redox species, ascorbic acid. The redox potential of plasma and blood was then measured for the first time at NPG electrodes. We show that the concentration of the redox species is crucial in evaluating the sensitivity of the electrode in biofouling solutions and, furthermore, we show that nanoporous gold electrodes can be advantageous to use in solutions that contain a complex matrix.

3.2. Experimental

3.2.1. Electrode Preparation

Planar gold slides were prepared by sonicating gold mirror slides (EMF Corporation) in ethanol followed by washing with DI water for 10 minutes each. After drying with a stream of nitrogen gas, the gold slides were plasma cleaned (Southbay, 18 W) for 5 minutes and further

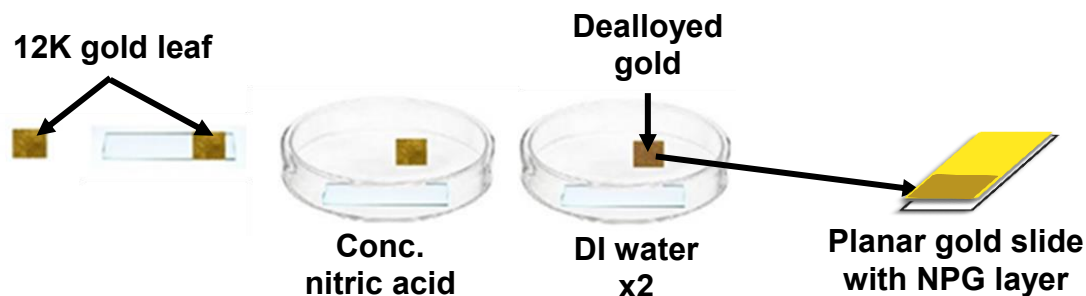


Figure 3.1. Schematic representation of nanoporous gold (NPG) preparation in nitric acid for 13 minutes and rinsed in DI water. Electrode is fabricated by capturing dealloyed square onto a cut planar gold slide.

cleaned by placing them under UV radiation (20 W) for at least six hours. Nanoporous gold (NPG) was prepared by dealloying 12 Karat gold leaf (Manetti, Fine Art Store) in concentrated nitric acid for 13 minutes (Caution: Nitric acid is dangerous).²¹ The etched leaf was transferred to a large petri dish filled with DI water, and left to sit in the water for at least 10 minutes. Using tweezers, a small clean planar gold slide was used to gently pick up the fragile gold leaf (**Figure 3.1**). The NPG electrode was dried with nitrogen gas and then left under UV radiation for at least 6 hours. The thickness of the nanoporous gold leaf is ~ 110 nm as measured from cross-sectional scanning electron microscope images (SEM, Hitachi SU-70). The electrode area was defined by a 1/8 inch circle hand punched into a piece of tape (HYDE), which was carefully placed on the electrode surface just prior to use. The surface area of the NPG electrodes was measured in 0.5 M sulfuric acid as previously described^{21, 23} and was ~ 17 times larger than the geometric area.

3.2.2. Electrochemical Procedures

Stock solutions of potassium ferri/ferrocyanide or ascorbic acid were prepared in pH 7.4 phosphate buffer (0.1 M in 0.1 M KCl), unless otherwise noted. To biofoul the surfaces, the electrodes were first vertically placed in 1 mg/mL of fibrinogen (bovine, MP biomedical) in phosphate buffer. After soaking for several hours, the electrodes were removed and gently rinsed

with DI water. The potentiometric experiments were initiated by pipetting a known volume of potassium ferricyanide $[\text{Fe}(\text{CN})_6]^{3-}$ into a 10 mL glass beaker. The open circuit potential (OCP; also referred to as a rest potential or equilibrium potential) was potentiometrically measured using a CHI potentiostat against a AgCl coated Ag wire reference electrode. After 10 minutes, aliquots of potassium ferrocyanide $[\text{Fe}(\text{CN})_6]^{4-}$ were added every ~5 minutes while the solution gently stirred and the OCP measured. Upon completion of the potentiometric experiment, a CV was acquired at 50 mV/s. In this case, a Pt auxiliary electrode was also used. For the ascorbic acid experiments, a known volume of buffer was added to a 10-mL beaker and aliquots of 5 mM ascorbic acid were added while the OCP was measured. Fresh heparinized waste blood was obtained from the apheresis clinic at VCU, centrifuged and the plasma stored at -4°C and was used the following day.

3.3. Results and Discussion

3.3.1. Background

Potentiometric experiments are simple and inexpensive to implement and hold considerable promise as a tool to probe redox chemistry in unconventional solutions. Recent work by others have also indicated that potentiometry is less sensitive to the effects of biofouling as compared to cyclic voltammetry²⁴ - at least at high concentrations - and perhaps lending itself well to probe redox chemistry in biological solutions. However, careful attention needs to be given to the electrode surface and the role it plays in the observed response, particularly in solutions that contain low concentrations of redox molecules such as those found in many natural systems that may contaminate/modify the electrode surface.^{15, 25} To evaluate the impact of biofouling in more detail, we examined the potentiometric and voltammetric response of dilute solutions of a poised redox system consisting of potassium ferri/ferrocyanide (0.2, 0.1, 0.075

mM) at both planar gold and nanoporous gold electrodes purposely biofouled by exposure to fibrinogen.^{21, 24} The potentiometric response was also examined using an unpoised redox system containing only ascorbic acid. In both cases, comparisons were made to clean electrodes not exposed to fibrinogen. Previous work has shown that albumin, fibrinogen, and other proteins adsorb very quickly on planar electrode surfaces.²⁶⁻²⁹

3.3.2 Potentiometry of $[\text{Fe}(\text{CN})_6]^{3-}/[\text{Fe}(\text{CN})_6]^{4-}$

Figure 3.2a shows a representative OCP vs. time trace obtained at a planar gold electrode, previously soaked in fibrinogen for 1.5 hours. The solution contained 0.2 mM $[\text{Fe}(\text{CN})_6]^{3-}$ to which aliquots of $[\text{Fe}(\text{CN})_6]^{4-}$ were added. With each addition of $[\text{Fe}(\text{CN})_6]^{4-}$ the potential decreased as the ratio of $[\text{Fe}(\text{CN})_6]^{4-}/[\text{Fe}(\text{CN})_6]^{3-}$ in solution increased. A Nernst plot can be obtained by plotting the OCP vs. $\log [\text{Fe}(\text{CN})_6]^{4-}/[\text{Fe}(\text{CN})_6]^{3-}$. As shown in **Figure 3.2b**, a linear plot was obtained yielding a slope of -59.8 mV, a y-intercept of 153 mV, and a linear regression coefficient of 0.997. The experimentally determined slope is nearly identical to the expected value of -59.2 mV for this one-electron redox couple at both planar and NPG electrodes. The y-intercept is near the expected value of the formal potential of 142 mV (vs. Ag/AgCl in 0.1 M KCl).²⁵ Nearly identical results were also obtained at NPG previously soaked in fibrinogen.

A cyclic voltammogram (CV) acquired at the end of the potentiometric experiments, however, shows a very different result for the two electrodes, **Figure 2c**. On NPG, a characteristic CV with a peak splitting of 70 mV and a ratio of the peak Faradaic current of 1.0 was observed; indicative of a kinetically fast and well-behaved redox system even after the electrode was exposed to fibrinogen. However, on planar gold, no Faradaic response for the ferri/ferrocyanide redox couple was observed. Fibrinogen adsorbs on planar gold electrodes

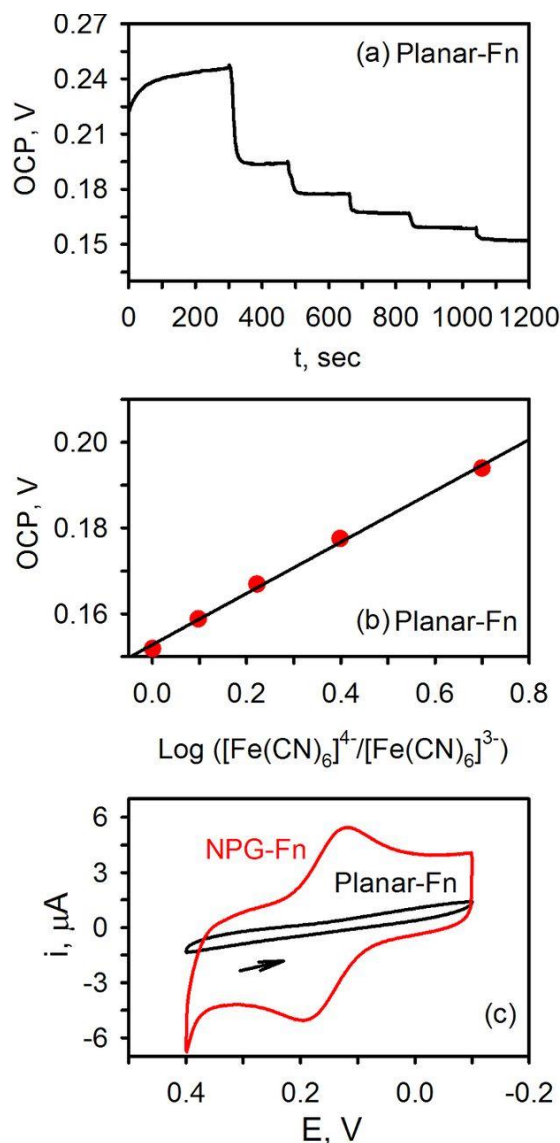


Figure 3.2. Reprinted with permission from reference 1. Copyright 2016, The Electrochemical Society. (a) OCP- time traces acquired at a biofouled planar gold electrode in 0.20 mM $[\text{Fe}(\text{CN})_6]^{3-}$ in pH 7.4 phosphate buffer following successive additions of $[\text{Fe}(\text{CN})_6]^{4-}$ (b) Corresponding Nernst plot. The solid line is the linear regression fit to the data points: $y = -0.0598x + 0.153$; $R^2 = 0.997$. (c) CV acquired at the end of the potentiometric experiment, 50 mV/s. The final concentrations of ferri/ferrocyanide in solution were 0.18/0.22 mM.

fairly rapidly and blocks electron transfer, thus giving rise to a CV showing only capacitive current.²¹ On NPG, protein adsorption also takes place. However, because of the electrode's pore morphology (**Figure 3.3**) and biosieving capabilities, fast electron transfer can still be

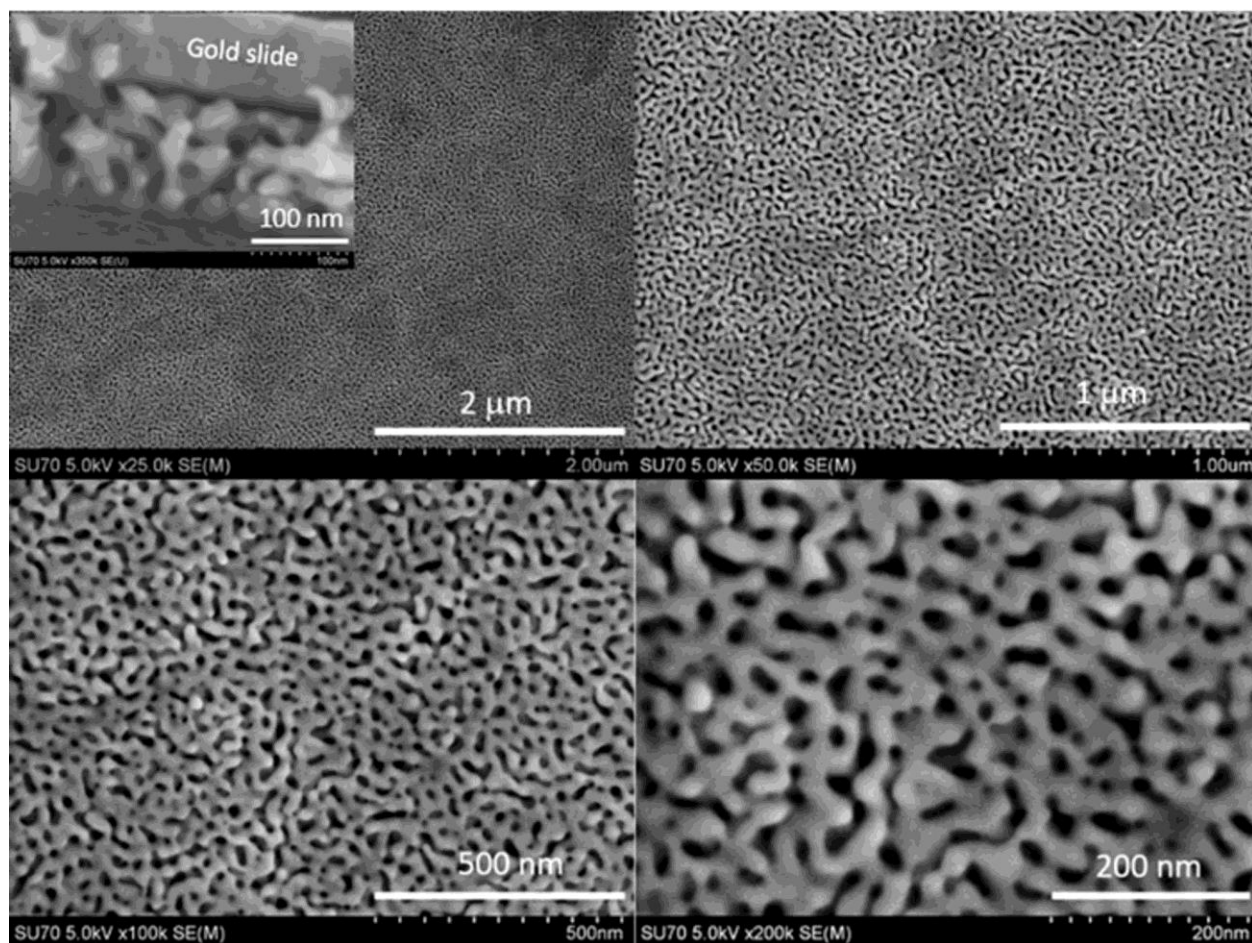


Figure 3.3. Reprinted with permission from reference 1. Copyright 2016, The Electrochemical Society. SEM images of nanoporous gold (NPG) at four different magnifications. Inset shows cross-sectional image.

achieved.²¹ In this case, because the nano-sized pores are similar in size to fibrinogen molecules, the inner surface stays ‘clean’ providing a pristine surface for much smaller redox species (e.g., ferricyanide) to freely exchange electrons.²¹ What is interesting, however, is that at this concentration, the potentiometric response at the two electrodes is nearly identical even though CV shows significant differences as previously noted.²⁴

To evaluate the response of the electrodes at low concentrations, the experiments were repeated using 0.1 mM and 0.075 mM $[\text{Fe}(\text{CN})_6]^{3-}$ solutions. Again, both biofouled and non-biofouled electrodes were examined. OCP-time traces similar to those shown in **Figure 3.2** were

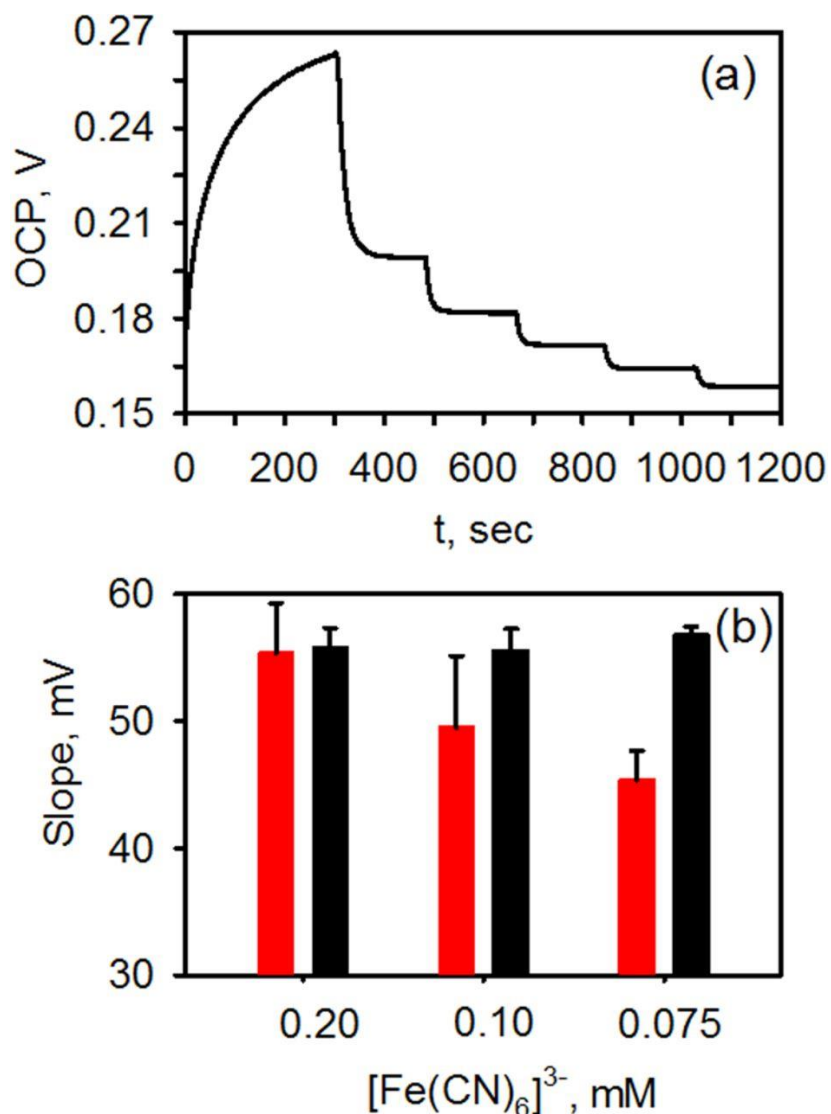


Figure 3.4. Reprinted with permission from reference 1. Copyright 2016, The Electrochemical Society. (a) OCP-time traces acquired at NPG after exposure to fibrinogen. The solution initially contained in 0.1 mM potassium ferricyanide in pH 7.4 phosphate buffer to which increments of potassium ferrocyanide were added. (b) Nernst slope (absolute value) obtained at biofouled planar gold (red) and nanoporous gold (black) electrodes at three different concentrations. Error bars represent the standard deviations from six electrodes made on different days.

observed, **Figure 3.4a**. From these results, Nernst plots were generated and the slopes determined by fitting the data via a linear regression analysis. **Figure 3.4b** shows the Nernst slope obtained at the three different concentrations examined. Error bars represent the standard deviation acquired from six electrodes made on different days. What can be seen is that for

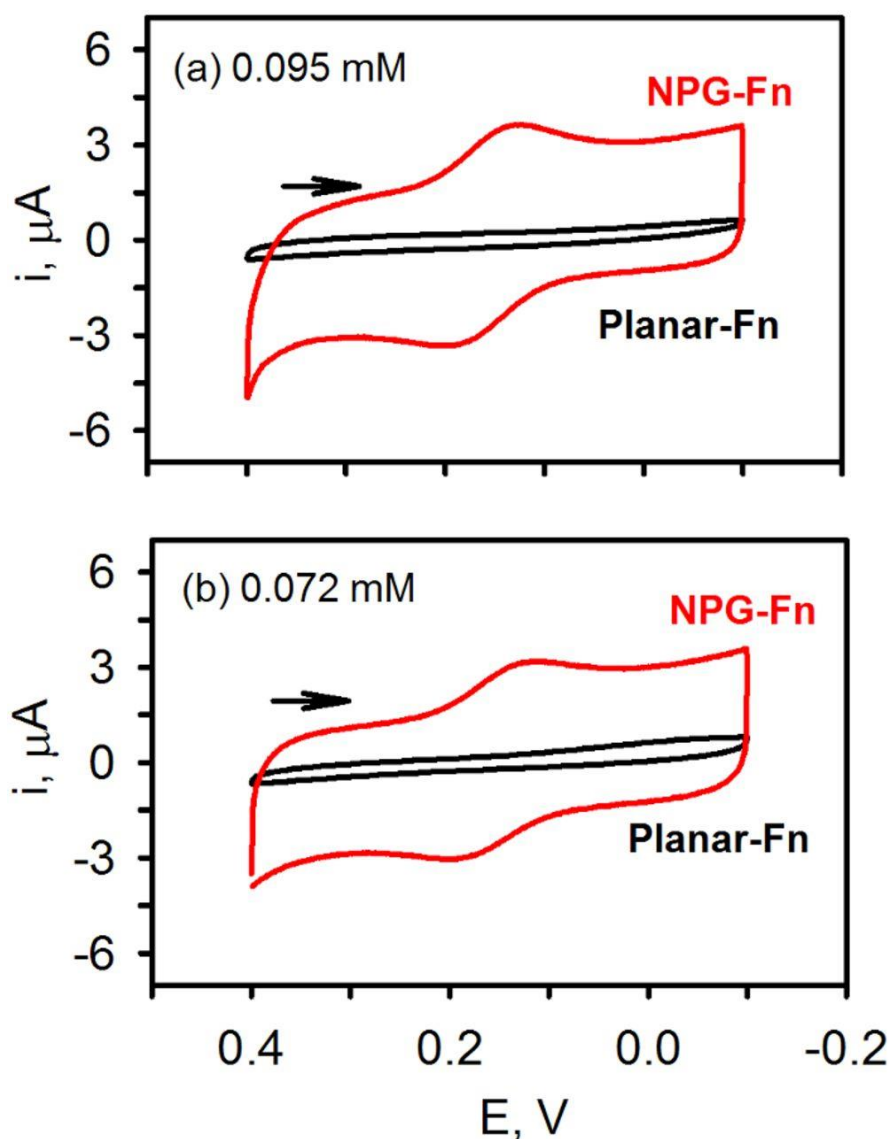


Figure 3.5. Reprinted with permission from reference 1. Copyright 2016, The Electrochemical Society. CVs acquired at the end of the potentiometric experiment, 50 mV/s, at nanoporous gold (NPG) and planar gold. The final concentrations of ferri/ferrocyanide were 0.095/0.095 (top) or 0.072/0.075 mM (bottom) in pH 7.4 phosphate buffer. The electrodes were soaked in 1 mg/mL fibrinogen for several hours prior to the potentiometric experiments.

biofouled planar gold electrodes, the absolute value of the slope drops from -56 ± 4 mV to -45.4 ± 2 mV ($N = 6$) as the concentration of the redox molecules decreases from ~ 0.2 mM to 0.075 mM. In contrast, at a clean planar gold electrode not exposed to fibrinogen, the slope is Nernstian. This result suggests that the potentiometric response is indeed affected by the

presence of a layer of fibrinogen on the electrode surface. While the electrode still functions, there is ~20% loss in its sensitivity. This result indicates that potentiometric measurements are perhaps much more sensitive to the effects of biofouling than what was first suggested.²⁴ On NPG, however, the slope does not decrease and no loss in sensitivity was observed. The slope is in agreement with the theoretical value of -59.2 mV, regardless of the concentration of the redox molecules in solution.

Cyclic voltammograms collected at the end of the potentiometric experiments are shown in **Figure 3.5**. As expected, on NPG, the voltammetric response of potassium ferri/ferrocyanide is nearly ideal. Distinct Faradaic peaks can be seen on top of a large capacitive current (because of the larger electrode area) with an observed peak splitting of ~ 75 mV. On planar gold, however, no Faradaic response was observed. These results indicate that nanoporous gold is a more efficient electrode to use when making both potentiometric and cyclic voltammetric measurements, particularly in complex solutions containing relatively low concentrations of redox molecules where electrode fouling may take place.

3.3.3. Potentiometry of Ascorbic Acid: An Unpoised System

We have also examined the potentiometric and cyclic voltammetric response of ascorbic acid, a biochemically important antioxidant, using biofouled NPG and planar gold electrodes. Comparisons were once again made to the pristine electrodes. Since only one form of the redox couple is present, this system is unpoised unlike that of ferri/ferrocyanide. In addition, the oxidation of ascorbic acid is also more complicated and involves $2e^-$ and $2H^+$ and an electro-inactive product.³⁰ The results from the voltammetric and potentiometric experiments are shown in **Figure 3.6**. At clean planar and NPG electrode, the background subtracted CV of 0.27 mM ascorbic acid depicts a single Faradaic peak at ~ 0.2 V corresponding to the oxidation of ascorbic

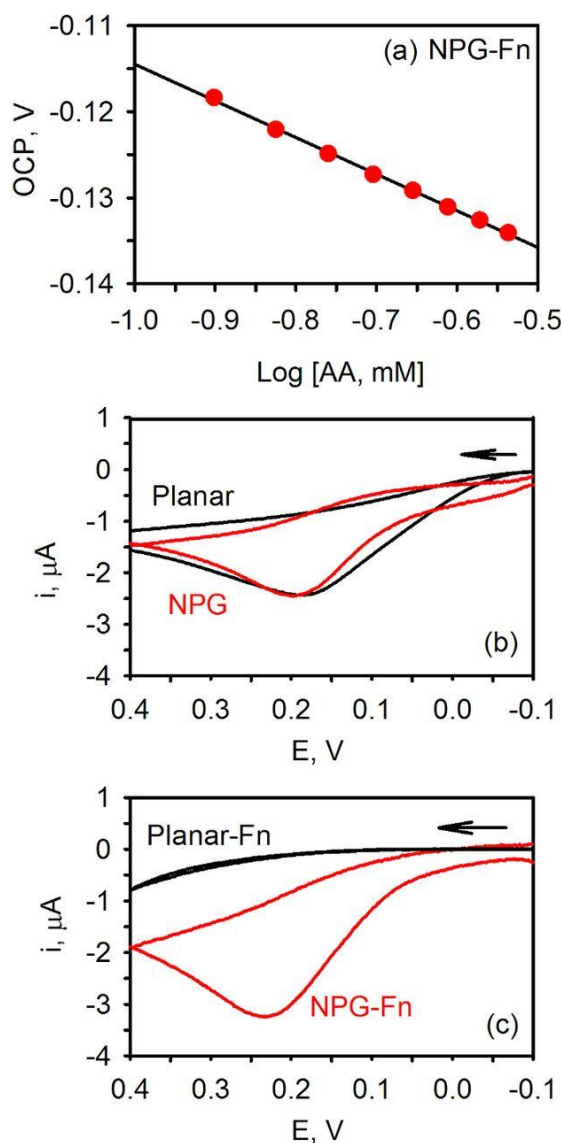


Figure 3.6. Reprinted with permission from reference 1. Copyright 2016, The Electrochemical Society. (a) Nernst plot for the addition of ascorbic acid to pH 7.4 phosphate buffer. The solid line is the linear regression fit to the data points: slope = -42.5 mV , $R^2 = 0.999$. (b) Background subtracted CVs of 0.27 mM ascorbic acid in buffer at 50 mV/s at nanoporous gold (NPG) and planar gold electrodes. (c) Background subtracted CVs of ascorbic acid after modification of the electrodes with 1 mg/mL fibrinogen for several hours.

acid (**Figure 3.6b**). In contrast, when the electrodes were exposed to fibrinogen for two hours, the Faradaic peak disappears at planar gold but remains on NPG (**Figure 3.6c**). These results are similar to that described for ferri/ferrocyanide where the voltammetry is very sensitive to the presence of surface contamination on planar gold while significantly less so on NPG.

Nernst plots were obtained by measuring the OCP of the electrode immersed in phosphate buffer upon addition of successive aliquots of ascorbic acid while stirring. On unmodified NPG, a slope of -30.0 ± 2.1 mV ($N = 4$) was obtained consistent with a $2e^-$ process. On planar gold, however, much more variability in the measured slope was observed: -32.2 ± 13.9 mV ($N = 7$). For several of the tested electrodes, the data was only linear at low concentrations, which suggests that the observed variability could be related to surface adsorption of ascorbic acid. After the electrodes were exposed to fibrinogen, Nernst plots were once again obtained, a representative example of which is shown in **Figure 3.6a**. A slope of -40.8 ± 5.3 mV ($N = 8$) for NPG was obtained, which is a slightly higher than the expected slope of -30 mV. In contrast, planar gold modified with fibrinogen ($N = 6$), were found to be insensitive to changes in the ascorbic acid concentration and no Nernst plots could be obtained. Collectively these results indicate that NPG electrodes are less sensitive to surface contamination than planar gold electrodes.

3.3.4. Blood Redox Potential

One example where potentiometric measurements of redox potential may be valuable is in blood and plasma as they contain low concentrations of redox molecules (ascorbic acid, ~ 0.080 mM; uric acid, ~ 0.2 mM) in a complex, biofouling matrix. Blood (or plasma) redox potential has been measured using commercial meters, typically with a planar platinum electrode. Investigations have evaluated changes in redox potential observed during exercise, in trauma patients, or in rabbits subjected to hemorrhagic shock.³¹⁻³³ Potential variations were not large (10–20 mV). In one case, the biofouling issue was addressed by using an electrochemical pretreatment to desorb the adsorbed proteins just prior to measurement of OCP.³⁴ Most other

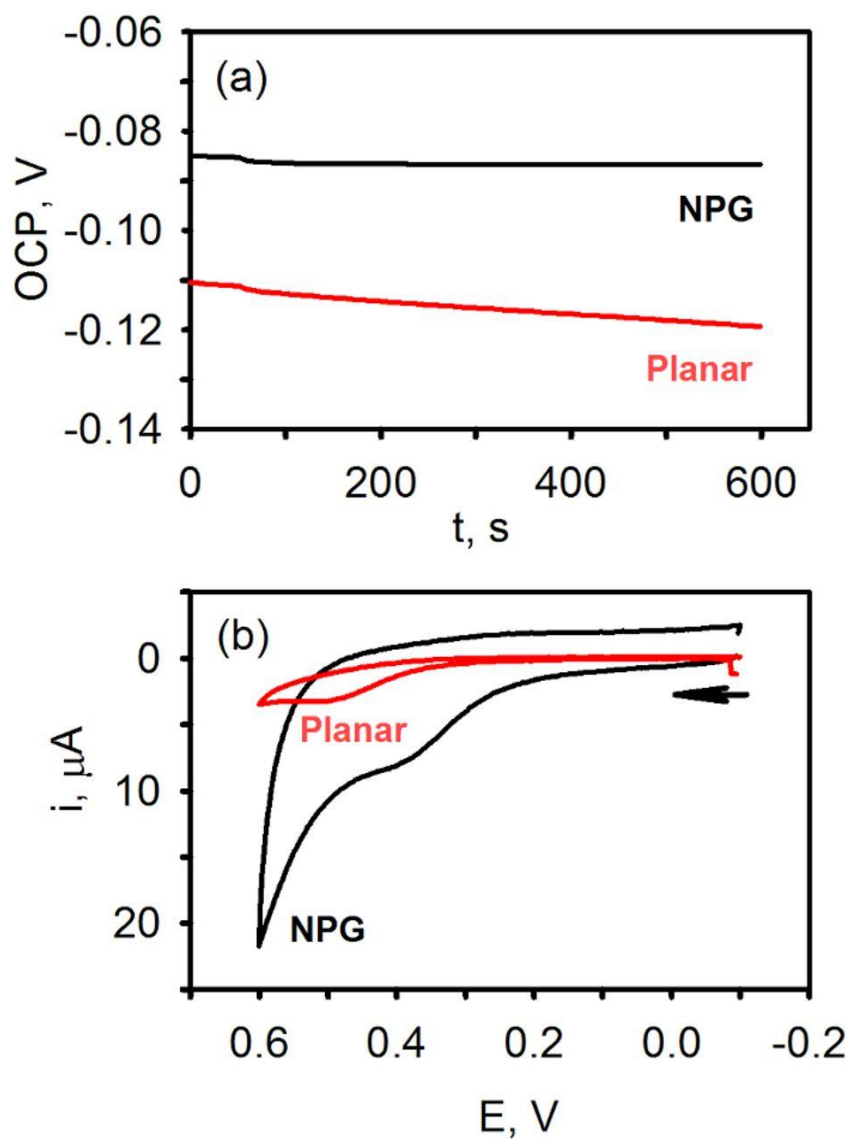


Figure 3.7. Reprinted with permission from reference 1. Copyright 2016, The Electrochemical Society. (a) Continuous OCP-time traces acquired at unmodified nanoporous gold (NPG) and planar gold in heparinized human plasma (b) CVs acquired at the end of the potentiometric experiments, 50 mV/s.

work does not address this problem and the impact it may have on the observed potentiometric response. Given the results described above, a better alternative may involve the use of NPG.

Figure 3.7 shows the continuous measurement of the redox potential of waste human plasma (heparinized) using unmodified NPG and planar gold for a time period of 10 min. As can be seen, the OCP reaches a near steady-state value quicker at NPG than at planar gold and the value

of OCP recorded at 10 min is more positive at NPG vs. planar: -86 vs. -119 mV for this particular data set. The CVs acquired at 50 mV/s after the OCP measurements are shown in Figure 7b. A small Faradaic response is observed at ~ 0.35 V on NPG and ~ 0.5 V on planar gold. This peak results from the oxidation of uric acid, ascorbic acid and quite possibly other antioxidants found in blood.^{35, 36} Additional experimentation is necessary to understand what gives rise to the voltammetric peak and then to explain the origin of the peak shift observed on NPG vs. planar gold.

As can be noted, there are significant differences in the value of OCP of human plasma obtained at NPG and planar gold. We also noted such differences in waste heparinized animal blood as well. For example, pig blood OCP measurements at NPG and planar gold electrodes yielded values of -108 ± 7 vs. -151 ± 2 mV ($N = 3$), respectively. In rabbit blood, OCP using NPG and planar gold were -119 ± 4 vs. -155 ± 4 mV ($N = 3$), respectively.³⁷ These differences likely reflect differences in the interfacial interactions between the different surfaces and redox molecules in blood. Planar gold will have a layer of adsorbed, likely denatured proteins on its surface, which will impede electron exchange, decrease the response rate, and reduce its sensitivity toward the OCP measurements. This undesired chemical modification of the electrode surface could also bias the value measured. On the other hand, NPG contains a trace amount of silver, has a much higher surface area, and a very different microscopic structure than planar gold. The presence of appropriately sized nanopores and nanopore architecture also ensures that there are plenty of places for electron exchange to take place with multiple redox species present in blood, even those that traditionally have slow rates of electron exchange.^{16, 22} Additional work is needed to tease out these differences and the effect they have on blood redox potential measurements.

3.4. Conclusions

Both potentiometric and voltammetric measurements can be used to obtain valuable information about the redox chemistry taking place in solutions of varying complexity, particularly when careful attention is given to proper electrode design. When the concentrations are low and the matrix complex, nanoporous gold electrodes formed by dealloying gold leaf outperform planar gold electrodes. Faradaic peaks for the reduction/oxidation of potassium ferri/ferrocyanide via cyclic voltammetry are unperturbed on nanoporous gold exposed to fibrinogen while they are non-existent on planar gold also exposed to fibrinogen. Similar results were observed for ascorbic acid. In the potentiometric experiments, such biofouling effects are most prominent at low concentrations (e.g., 0.1 mM for potassium ferri/ferrocyanide) on planar gold whereas no biofouling effects and Nernstian responses were found using nanoporous gold. In plasma and blood, differences were also noted in both the potentiometric and cyclic voltammetric experiments undertaken at planar and nanoporous gold electrodes. In future work, we plan to further study and understand these differences with the goal of improving and expanding our ability to make electrochemical measurements in chemically complex biological solutions.

3.5. References

1. Farghaly, A.A., Lam, M., Freeman, C. J., Uppalapati, B., and Collinson, M. M. (2016). Potentiometric Measurements in Biofouling Solutions: Comparison of Nanoporous Gold to Planar Gold. *J. Electrochem. Soc.*, **163**(4), H3083–H3087.
2. Bakker E., in *Environmental Analysis by Electrochemical Sensors and Biosensors*, Moretto L. and Kalcher K., Editors, p. 193–238 (2014), Potentiometric Sensors 10.1.
3. Noyhouzer T., Valdinger I., and Mandler D., Enhanced potentiometry by metallic nanoparticles, *Anal. Chem.*, **85**, 8347 (2013).
4. Bakker E. and Pretsch E., Modern potentiometry, *Angew. Chemie - Int. Ed.*, **46**, 5660(2007).
5. Kolling M., Ebert M., and Schulz H. D., A Novel Approach to the Presentation of pe/pH-Diagrams, *Redox Fundam. Process. Appl.*, 55 (1999).
6. Peiffer S., Klemm O., Pecher K., and Hollerung R., Redox measurements in aqueous solutions — A theoretical approach to data interpretation, based on electrode kinetics, *J. Contam. Hydrol.*, **10**, 1 (1992).
7. Caldeo V. and McSweeney P. L. H., Changes in oxidation-reduction potential during the simulated manufacture of different cheese varieties, *Int. Dairy J.*, **25**, 16 (2012).
8. Copeland A. and Lytle D., Measuring the oxidation–reduction potential of important oxidants in drinking water, *J. Am. Water Work. Assoc.*, **106**, E10 (2014).
9. Fiedler S., Vepraskas M. J. and Richardson J. L., Soil redox potential: importance, field measurements, and observations, *Adv. Agron.*, Vol. **94**, 1 (2007).
10. Goldin M. M. and Blanchard G. J., Redox Potential Measurement in Aqueous Solutions and Biological Media, *ECS Trans.*, **11**, 39 (2008).
11. Goncharuk V. V., Bagrii V. A., Mel'nik L. A., Chebotareva R. D. and Bashtan S. Y., The use of redox potential in water treatment processes, *J. Water Chem. Technol.*, **32**, 1(2010).
12. Jang A., Lee J. H., Bhadri P. R., Kumar S. A., Timmons W., Beyette F. R., Papautsky I. and Bishop P. L., Miniaturized redox potential probe for in situ environmental monitoring, *Environ. Sci. Technol.*, **39**, 6191 (2005).
13. Noyhouzer T., Kohen R. and Mandler D., A new approach for measuring the redox state and redox capacity in milk, *Anal. Methods*, **1**, 93 (2009).
14. Zelada-Guillén G. A., Bhosale S. V., Riu J. and Rius F. X., Real-time potentiometric detection of bacteria in complex samples, *Anal. Chem.*, **82**, 9254 (2010).
15. Carlsson T. and Muurinen A., Practical and Theoretical Basis for Redox-measurements in Compacted Bentonite. A Literature Survey, 1 (2008).
16. Collinson M. M., Nanoporous Gold Electrodes and Their Applications in Analytical Chemistry, *ISRN Anal. Chem.*, **2013**, 1 (2013).
17. Seker E., Reed M. L. and Begley M. R., Nanoporous gold: Fabrication, characterization, and applications, *Materials (Basel)*, **2**, 2188 (2009).

18. Wittstock A., Biener J. and Bäumer M., Nanoporous gold: a new material for catalytic and sensor applications, *Phys. Chem. Chem. Phys.*, **12**, 12919 (2010).
19. Saraf S., Neal C., Park S., Das S. and Barkam S., Electrochemical study of nanoporous gold revealing anti-biofouling properties, *RSC Adv*, **5**, 46501 (2015).
20. Daggumati P., Matharu Z., Wang L. and Seker E., Biofouling-Resilient Nanoporous Gold Electrodes for DNA Sensing, *Anal. Chem.*, **87**, 8618 (2015).
21. Patel J., Radhakrishnan L., Zhao B., Uppalapati B., Daniels R. C., Ward K. R. and Collinson M. M., Electrochemical properties of nanostructured porous gold electrodes in biofouling solutions, *Anal. Chem.*, **85**, 11610 (2013).
22. Park S., Kim H. C. and Chung T. D., Electrochemical analysis based on nanoporous structures, *Analyst*, **137**, 3891 (2012).
23. Farghaly A. A. and Collinson M. M., Electroassisted codeposition of sol-gel derived silica nanocomposite directs the fabrication of coral-like nanostructured porous gold, *Langmuir*, **30**, 5276 (2014).
24. Kuhlmann J., Dzogan L. C. and Heineman W. R., Comparison of the Effects of Biofouling on Voltammetric and Potentiometric Measurements, *Electroanalysis*, **24**, 1732 (2012).
25. Teasdale P. R., Minett A. I., Dixon K. and Lewis T. W., Batley G. E., Practical improvements for redox potential (E(H)) measurements and the application of a multiple-electrode redox probe (MERP) for characterising sediment in situ, *Anal. Chim. Acta*, **367**, 201 (1998).
26. Barfidokht A. and Gooding J. J., Approaches Toward Allowing Electroanalytical Devices to be Used in Biological Fluids, *Electroanalysis*, **26**, 1182 (2014).
27. Moulton S. E., Barisci J. N., Bath A., Stella R. and Wallace G. G., Investigation of protein adsorption and electrochemical behavior at a gold electrode, *J. Colloid Interface Sci.*, **261**, 312 (2003).
28. Moulton S. E., Barisci J. N., Bath A., Stella R. and Wallace G. G., Studies of double layer capacitance and electron transfer at a gold electrode exposed to protein solutions, *Electrochim. Acta*, **49**, 4223 (2004).
29. Ying P., Viana A. S., Abrantes L. M. and Jin G., Adsorption of human serum albumin onto gold: A combined electrochemical and ellipsometric study, *J. Colloid Interface Sci.*, **279**, 95 (2004).
30. Pisoschi A. M., Pop A., Serban A. I. and Fafaneata C., Electrochemical methods for ascorbic acid determination, *Electrochim. Acta*, **121**, 443 (2014).
31. Khubutiya M., Goldin M., Romasenko M., Volkov A., Hall P., Evseev A., Levina O., Aleschenko E. and Krylov V., Redox Potentials of Blood Serum in Patients with Acute Cerebral Pathology, *ECS Trans.*, **25**, 63 (2010).
32. Bernard C., Gallinet J. P., Conde C., Girardot J. J. and Massonie J. P., Interrelation between the blood redox potential and exercise induced variations of the biochemical characteristics of blood, *Bioelectrochemistry Bioenerg.*, **25**, 45 (1991).

33. Rael L. T., Bar-Or R., Mains C. W., Slone D. S., Levy A. S. and Bar-Or D., Plasma oxidation-reduction potential and protein oxidation in traumatic brain injury, *J. Neurotrauma*, **26**, 1203 (2009).
34. Khubutiya M. S., Evseev A. K., Kolesnikov V. A., Goldin M. M., Davydov A. D., Volkov A. and Stepanov A. A., Measurements of platinum electrode potential in blood and blood plasma and serum, *Russ. J. Electrochem.*, **46**, 537 (2010).
35. Mittal A., Göke F., Flint R., Loveday B. P. T., Thompson N., Delahunt B., Kilmartin P. a, Cooper G. J. S., MacDonald J., Hickey A., Windsor J. A. and Phillips A. R. J., The redox status of experimental hemorrhagic shock as measured by cyclic voltammetry, *Shock*, **33**, 460 (2010).
36. Chevion S., Roberts M. A. and Chevion M., The use of cyclic voltammetry for the evaluation of antioxidant capacity, *Free Radic. Biol. Med.*, **28**, 860 (2000).
37. Uppalapati B., *thesis, Virginia Commonwealth University*, (2014), Fabrication of Nanoporous Gold and Biological Applications.

Chapter 4

Fabrication of Microdroplet Nanoporous Gold (MDNPG) Electrodes and Performance of Potentiometric Measurements in Ultra-Small Volumes

Reproduced with permission from *Anal.Chem.*, 88(7), 3768–3774 (2016). Copyright 2016. American Chemical Society.¹

4.1. Introduction

Electrochemistry in ultrasmall volumes is valuable as it enables electrochemical measurements to be made when only minute amounts of liquid (e.g., from a biological sample) are available for testing.^{2–5} It also allows for higher throughput sensing and multiplexing, single cell analysis, and ease of integration into microfluidic devices and platforms.^{2–5} Small volume electrochemistry has been achieved using a number of strategies^{6–22} that include microfabrication of ultrasmall vials with and without embedded electrodes as well as creating the electrochemical cell from a single drop of solution.^{3,4,6–13,16,17,20,23} In the latter studies, the droplet is placed on a surface and the reference, counter, and working electrodes are inserted^{13,20} Alternatively, the droplet can be placed on the working electrode and the remaining two electrodes inserted in the solution.¹⁸ Also possible is the case when an array of oil droplets is placed on an electrode, which is then immersed in an aqueous (and thus immiscible) solution containing the reference and counter electrodes.^{14,15} In this study, we report potentiometric redox measurements in subnanoliter droplets of solution using optically transparent metallic redox electrodes (e.g., nanoporous gold electrodes) fabricated on glass microscope coverslips. Such measurements provide a rapid and highly efficient route to determine the oxidation–reduction potential (ORP) of an aqueous solution, which has been used as an indicator of water quality and the redox state of milk, cheese, soil, and blood products.^{24–31}

Much of the work in this field has focused on making voltammetric measurements in nanoscopic volumes whereby current flows and considerable care must be given to changes in droplet volume and hence concentration of the redox active species and to the formation of products at the counter electrode that essentially taints the solution.⁶ Two notable exceptions include the work by Tantra and Manz¹⁹ and Blaz et al.³² who have used ion selective membrane

electrodes. The former utilized a microfluidic chip design while the latter trapped a 30 μL drop of solution between a glass coverslip and the ion-selective electrode. Potentiometric redox measurements are conceptually simpler to perform compared to voltammetric measurements in that only two electrodes and a high impedance¹⁹ voltmeter are required; they operate under conditions of zero-current flow and, most importantly, can provide a simple cost-effective means to evaluate the redox state of a solution.^{33,34} The measured redox potential (E_{m}) is determined by measuring the open-circuit potential (OCP) or zero-current potential of an indicating electrode (E_{Ind}) (i.e., inert electrode such as gold or platinum) with respect to a reference electrode (E_{ref}) in a given medium using a high-impedance voltmeter, such that $E_{\text{m}} = E_{\text{Ind}} - E_{\text{ref}}$.³³ Since current does not flow, the concentration of the redox species in solution does not change.^{33,34} The measurement itself is simple and inexpensive and can be readily miniaturized as described herein to allow for its measurement in a single subnanoliter droplet of liquid.

Methods aimed at potentiometrically measuring the redox status of a solution typically employ large planar metal electrodes and/or relatively large volumes.^{33,35,36} Under such conditions, the time to reach equilibrium can be long and the electrode surfaces can become passivated, particularly by other species present in complex solutions. To address and solve these issues, our efforts have been focused on nanoporous gold electrodes^{37,38} and the use of ultrasmall volumes. Unlike planar gold electrodes, nanoporous gold electrodes can reduce the impact of protein adsorption on redox measurements through a unique biosieving mechanism^{39,40} and, furthermore, can detect redox molecules with sluggish electron transfer rates that could otherwise not be detected at a planar electrode.⁴¹ The significantly higher surface area (e.g., 10–50 \times larger than a planar electrode) also offers a greater number of sites for electron exchange to occur with as many species as possible even with some blockage of the electrode surface by

adventitious impurities. Small volumes also allow for faster equilibration, dramatically reducing analysis time and thus enabling high throughput testing. Such characteristics, for example, would be particularly valuable in the measurement of the redox potential of complex solutions such as blood or sludge products where limited volumes and/or limited waste products is a concern.

This report describes a new approach to make and validate potentiometric redox measurements in ultrasmall drops of solution and the implementation of microscopic redox titrations. The experiments begin with the construction of an optically transparent nanoporous gold electrode on a glass microscope coverslip, which is placed on the stage of an inverted microscope. Target droplets with volumes on the order of several hundred picoliters are placed on the appropriately modified gold electrode immersed in a hexadecane solution. The OCP of each individual drop one at a time is measured upon insertion of a chloridized silver wire in KCl, which serves as the reference electrode. Reagents can be precisely delivered into individual droplets; because of their small size, mixing takes place rapidly and the potential reaches equilibrium over a time scale of several milliseconds. The general applicability of this new method is demonstrated herein through a detailed study of both one- and two-electron poised redox couples as well as unpoised redox systems.

4.2. Experimental Section

4.2.1. Materials

Potassium ferricyanide, potassium ferrocyanide, ferrous ammonium sulfate, ferric ammonium sulfate, potassium phosphate dibasic, potassium phosphate monobasic, hydroquinone, benzoquinone, hexanes, concentrated nitric acid, concentrated hydrochloric acid, potassium chloride, L-ascorbic acid, ethanol (200 proof), 1-hexanethiol, and (3-mercaptopropyl)

trimethoxysilane 95% were purchased and used as received. Water (18 MΩcm) was purified using a Millipore water purification system. All reagent solutions were made fresh.

4.2.2. Nanoporous Gold (NPG) Preparation

Microscope glass coverslips (22 × 50 mm; 0.17 mm thickness) were sonicated for 10 min in ethanol followed by deionized water for 10 min and dried with N₂ gas. Coverslips were then O₂ plasma cleaned using a Southbay, PE 2000 plasma etcher at 20 W for 5 min by placing the slide face up in the stainless steel chamber. The glass coverslips were soaked with the plasma cleaned side facing upward in a 10 mM (3-mercaptopropyl)trimethoxysilane (MPTMS) in hexanes solution for 1 h in a 60 °C water bath.⁴² The coverslips were then rinsed with hexanes and left to dry. Manetti 12K gold leaf (FineArtStore, book of 25 loose leaves) was chemically dealloyed in concentrated nitric acid for 13 min and then floated on DI water twice for ~5 minutes.^{37,38} Conducting copper (Cu) tape (Ted Pella, PN 16072) was attached to the thiol modified side of the glass coverslips, which was then used to capture one dealloyed leaf. The dealloyed gold was dried with nitrogen and further cleaned by UV radiation (254 nm, 20 W) for 24 h by placing the electrode face up in a home-built box ~10 cm from the UV source. Prior to use, the microdroplet nanoporous gold (MDNPG) electrode was soaked in a ~ 0.01 mM solution of 1-hexanethiol in ethanol for 5 min and rinsed thoroughly with ethanol. Once rinsed, the nanoporous gold electrode was gently dried with nitrogen gas.

4.2.3. Droplet Formation and Mixing

Figure 4.1 shows a schematic illustration of the droplet-based potentiometric-redox measurement apparatus. A microdroplet nanoporous gold (MDNPG) electrode is fixed with PDMS (Kwik-Cast, WPI, Sarasota, FL) onto the underside of a microscope slide (1 in. × 3 in.) that has a 1 cm hole drilled through the center. This creates a small well that is then filled with

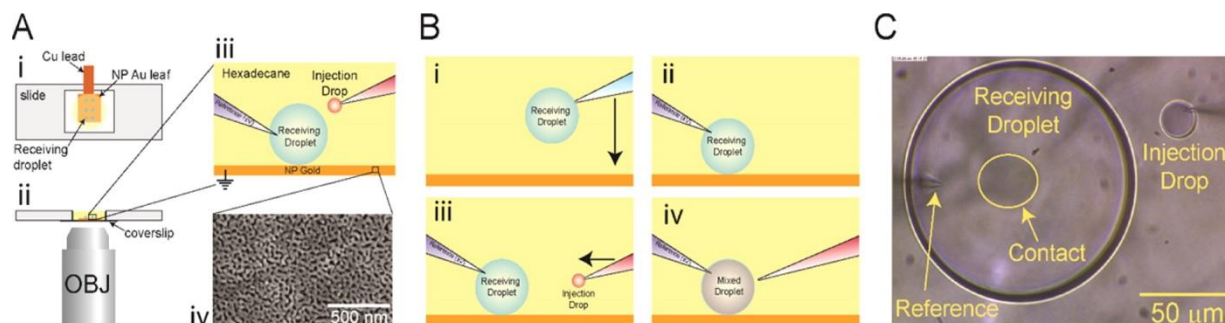


Figure 4.1. Reprinted with permission from reference 1. American Chemical Society Copyright 2016. Schematic illustration of the droplet-based OCP measurement apparatus. (A) The relevant components are mounted onto an inverted microscope with manipulation stages and a CCD camera as described in the main text. (A,i) Top down and (A,ii) side view of the microscope slide-based holder. A 1 cm hole drilled through a microscope slide is sealed from the bottom by a #1.5 glass coverslip that has a nanoporous gold leaf attached. A copper lead is attached to this gold leaf and serves as the ground reference connection. The ca. 100 μL well is filled with hexadecane solution to prevent the aqueous droplets from evaporating. (A,iii) A closer view near a single droplet shows that the receiving droplet is in contact with the nanoporous (NP) gold substrate. (A,iv) A closer look at the nanoporous electrode via an SEM scan shows the porous nature of the electrode. (B) A schematic illustration of the droplet-measurement protocol. (B,i) Backing pressure is applied to a pipet containing the receiving solution (blue), and the pipet is lowered to attach the droplet onto the NP electrode. (B,ii) The end of a micropipette containing the reference solution (purple, 0.1 M KCl) is positioned inside the receiving droplet. (B,iii) Backing pressure is applied to a second pipet containing the injection solution (red) and a small droplet is formed. This second pipet is moved toward the receiving droplet. (B,iv) Upon contact between the receiving droplet and the injection droplet, the contents are rapidly mixed. (C) A bright field image of a receiving droplet sitting on the surface of nanoporous gold with an injection droplet nearby. The receiving droplet is weakly attached to the surface as evidenced by the small contact area highlighted with the yellow ellipse near the center of the droplet.

60 μL of hexadecane (Sigma-Aldrich, St. Louis, MO). The slide is placed onto an inverted microscope (Axio Observer D, Zeiss, Germany), and the microscope is bolted to an air-floated optical table within a Faraday cage enclosure (Kinetic Systems, Boston, MA). A borosilicate glass capillary (1.0 mm OD, 0.78 mm ID with filament, Sutter Instruments, Novato, CA) is formed into a pipet tip using a laser-based pipet puller (P-2000, Sutter) and then soaked in sigmacote (Sigma) for ca. 30 s. It is backfilled with the receiving droplet solution and positioned with a motorized manipulator (MPC-275, Sutter) several hundred micrometers above the gold

electrode. A several hundred picoliter droplet of the receiving droplet solution is ejected under pressure (Femtojet, Eppendorf) from the tip, and the tip is positioned down near the gold surface so the droplet transfers from the tip onto the nanoporous gold electrode surface. A quartz capillary (1 mm OD, 0.7 mm ID with filament, Sutter) pulled into a micropipette, containing a Ag/AgCl electrode, is filled with 0.1 M KCl. This is brought down into contact with the surface-bound reference droplet. The inner diameter of the micropipet must be small (estimated to be $<0.05\ \mu\text{m}$ by the manufacturer), otherwise, the receiving droplet will be sucked into the micropipette in a matter of seconds. The Ag/AgCl electrode is formed by placing a 0.3 mm bare silver wire in full strength bleach solution (Clorox) for several minutes. Next, a second glass microcapillary (Femtotip II, Eppendorf, NY) is filled with the appropriate injection solution and positioned near the receiving droplet with a second motorized manipulator (MPC-275). A pressure pulse applied to this tip (Femtojet) ejects a droplet on the order of several picoliters that remains attached to the end of this tip. This injection drop is then brought into contact and spontaneously fuses with the receiving droplet. The contents of the two droplets rapidly mix over a period of several milliseconds.

4.2.4. Data Collection and Analysis

Redox potentials were recorded using an amplifier head stage (Axopatch 200B, Molecular Devices, Carlsbad, CA) operating in current-clamp mode. Signals were digitally sampled (Digidata 1440A, Molecular Devices) at 20 kHz and filtered with a four-pole 10 kHz low-pass Bessel filter. The data were recorded in axon binary files (.abf) with pClamp 10 software (Molecular Devices). Data analysis of the .abf files was performed using IGOR Pro 6.36 (Wavemetrics Inc. Lake Oswego, OR). To compute the volume of the droplet, a calibration slide with 100 μm spacing was used to calibrate the magnification of the microscope and the



Figure 4.2. Schematic representation of (A) glass functionalization using (3-mercaptopropyl) trimethoxysilane (MPTMS) in hexanes for 1 hour in a 60°C water bath and (B) preparation of nanoporous gold (NPG) via dealloying in concentrated nitric acid for 13 minutes, rinsing with DI water, and capture of dealloyed square on copper fitted functionalized glass slide.

diameter of the droplets was measured just prior to contact with the electrode surface. From the diameter of the spherical droplet, the drop volume was obtained.

4.2.5. Preparation of Nanoporous Gold (NPG) on Glass

A common and relatively inexpensive procedure to make nanoporous gold electrodes involves capturing a piece of gold leaf floating on an air–water interface on a conducting substrate such as a gold-coated slide.³⁷ This method is a useful and relatively inexpensive approach to fabricate a gold/silver alloy of an appropriate composition if a gold/silver sputtering system, for example, is not available.^{37,43} However, this procedure will not work with an inverted microscope because the electrode is not transparent. To circumvent this problem, we adapted a procedure by Ciesielski et al. and used a modified glass microscope coverslip as the support.⁴² Modification was accomplished using (3-mercaptopropyl) trimethoxysilane, which firmly binds the gold to the glass surface through chemisorption. An electrical connection was

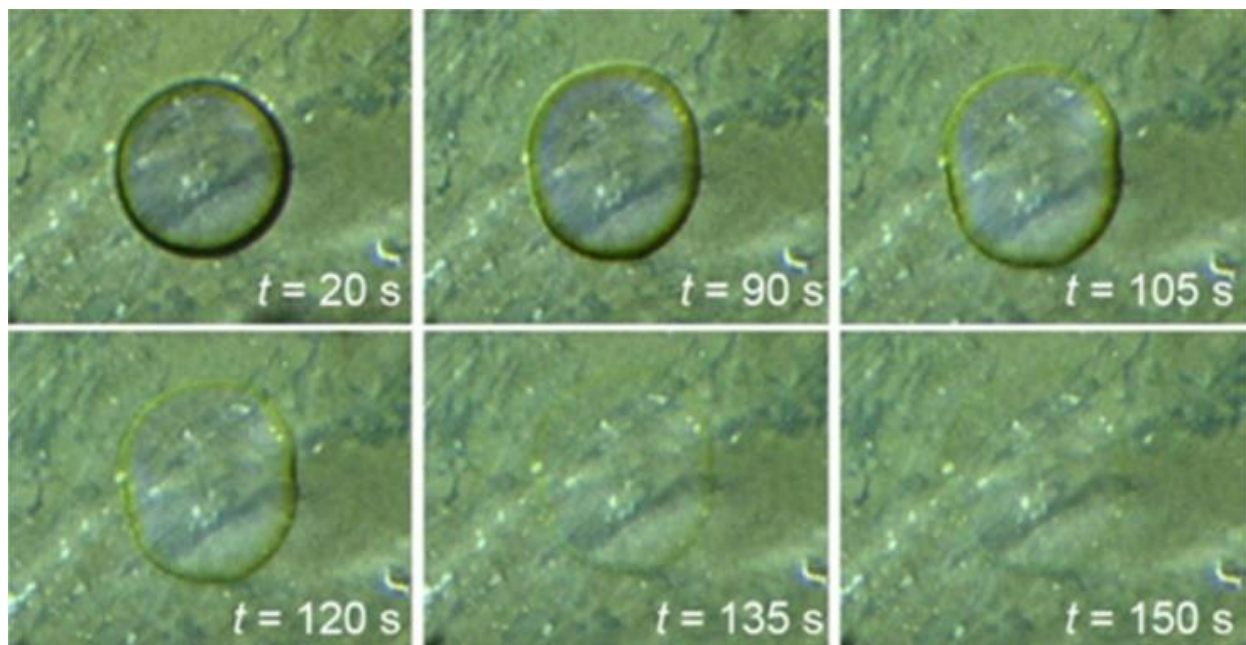


Figure 4.3. Reprinted with permission from reference 1. American Chemical Society Copyright 2016. Bright field optical microscopy images of receiving droplets on the surface of a modified nanoporous gold electrode. The desired shape of the droplet is apparent during the first ~ 20 s and begins to degrade around 90 s leading to complete loss of the droplet at 150 s. The droplet diameter in the $t = 20$ s image is ca. $90\ \mu\text{m}$.

made by first placing a piece of copper tape on the modified coverslip and then capturing a piece of nanoporous gold leaf such that it contacts the copper tape (**Fig. 4.2**). Once dried, the nanoporous gold chemisorbs onto the modified glass surface. The electrodes behave similarly to those on gold³⁹ and have real surface areas that are ~ 10 – 20 times larger than the geometric area (unpublished results). It should also be possible to use an ITO coated coverslip, but at a significantly higher cost than a simple glass microscope coverslip.

The inherent hydrophilic and porous nature of the optically transparent gold electrode, however, created issues with droplet stability. When a submicroliter drop of an aqueous solution was placed on the surface of nanoporous gold, the aqueous solution often permeated through the gold nanopores on the time scale of the experiment. An extreme example of this is illustrated in **Figure 4.3**. Initially, the drop has a well-defined shape, but over time, its shape becomes

distorted; eventually, the drop disappears from view due to permeation into the porous gold framework. The loss of sample was not due to evaporation as the electrode cell was filled with hexadecane in order to create a hydrophobic environment. In less extreme cases, considerable drift in the zero-current potential is observed. To overcome this problem, the electrodes were modified with 1-hexanethiol to increase the hydrophobicity of the gold. The immersion time of the electrode in 1-hexanethiol and its concentration in ethanol were optimized for each experiment to create a surface that was neither too hydrophobic nor too hydrophilic. This optimization often involved making a few 1-hexanethiol solutions that range in concentration from ~ 0.01 to 1 mM (**Fig. 4.4**). When the surface was too hydrophobic, the droplets moved on the surface when attempting to insert the reference electrode. This prevented contact between the reference and the droplet, thus the contact between the aqueous droplets and the electrode surface became a problem. Under these circumstances, it was difficult to obtain a stable potential. Optimal hydrophobicity allows for the receiving solution droplet to maintain a near ideal spherical shape when placed on that surface allowing for a stable potentiometric signal to be obtained. It also minimizes cross talk between individual droplets. Given the low

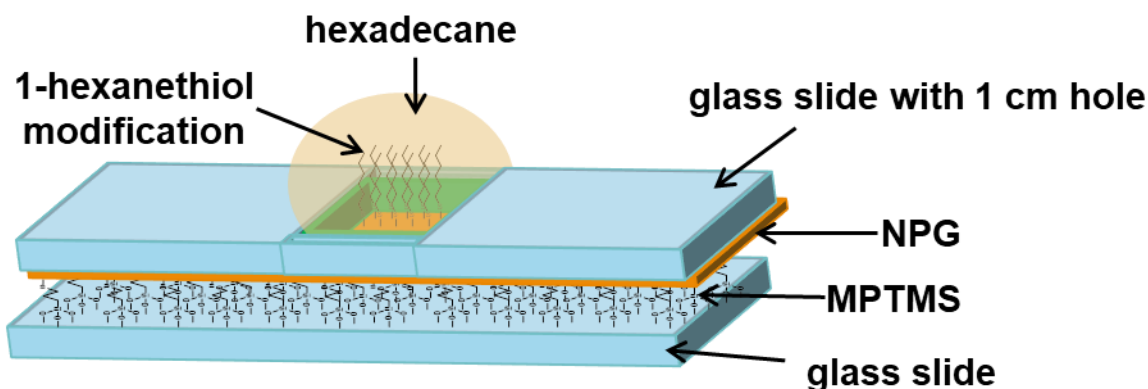


Figure 4.4. Cartoon representation of fabricated microdroplet electrode using Kwikcast to secure NPG electrode to another glass slide with 1 cm hole, modification of NPG surface with 1-hexanethiol, and placement of hexadecane in the well created.

concentration and short immersion times used, we speculate that the 1-hexanethiol partially modifies the outer surface of the nanoporous gold just enough to impart some hydrophobicity to the surface.

4.3. Results and Discussion

4.3.1. Measurement of Open-Circuit Potentials (OCP) in Subnanoliter Droplets

The experiment begins by fixing the optically transparent nanoporous gold electrode onto a UV cleaned glass coverslip and attaching this to the underside of a microscope slide with a 1 cm hole drilled in the center. This modified slide was then mounted onto an inverted microscope bolted to an air-floated optical table with dual manipulators allowing control of the receiving solution pipet and the injection solution pipet (**Figure 4.1A(i,ii)**). This allowed for visualization of subnanoliter droplet insertion and subsequent addition. To prevent evaporation of the small volume droplets, the cell was filled with hexadecane.

To generate the receiving droplet, a borosilicate capillary was formed into a micropipette tip (ID $\sim 5\ \mu\text{m}$) with a laser-based puller and fixed onto a motorized manipulator. To keep the aqueous droplet from sticking to the tip, the outside surface of the tip was pretreated with a hydrophobic coating. A droplet with diameter on the order of several hundred micrometers ($\sim 1000\ \text{pL}$) was ejected and brought down into contact with the surface of nanoporous gold where it then adhered. **Figure 4.1B(ii-iv)** depicts an ideal aqueous droplet sitting on the surface of nanoporous gold. The slightly hydrophobic gold surface ensures a near ideal sphere with a contact area defined by the solid circle shown in the figure, which in this example is $\sim 300\ \mu\text{m}^2$. The electrical circuit becomes complete once the reference electrode is inserted in the droplet via the use of the optical microscope (**Figure 4.1A(iii)**). The highly resistive hexadecane solvent and

slightly hydrophobic gold surface ensures that each droplet introduced to the electrode surface is electrically isolated from other droplets. Multiple droplets are placed on the surface, and each one is interrogated individually by moving and reinserting the reference electrode into each successive drop. Care must be taken to minimize drop-to-drop contamination by either washing the reference electrode or changing it completely.

The potentiometric measurements were undertaken once there was no visible change in the shape and size of the receiving droplet, typically within 5 min. A stable open circuit potential (OCP) of the receiving droplet was obtained after the reference electrode was inserted in the droplet. **Figure 4.5a** shows the potential–time trace after the reference electrode was inserted in a drop containing 0.5 mM potassium ferricyanide ($\text{K}_3[\text{Fe}(\text{CN})_6]$) in 0.1 M KCl and after successive additions of potassium ferrocyanide as described in the sections that follow.

To add a known amount of a reagent into the receiving droplet, a second pipet was filled with the appropriate solution and used to form the injection droplet (**Figure 4.1B(iii)**). The volume of the injection droplet was calculated by measuring the diameter of the droplet. In this manner, accurate measurements of respective species' concentrations can be determined. To add the reagents to the receiving droplet, the injection droplet was moved with a micromanipulator until it just touched the surface. The two solutions mix rapidly, and the OCP changes, ideally in accordance to the Nernst equation.

In **Figure 4.5b**, OCP–time traces for the successive addition of 50 mM $[\text{Fe}(\text{CN})_6]^{4-}$ to a 470 pL drop of 5 mM $[\text{Fe}(\text{CN})_6]^{3-}$ is shown. As can be seen, the OCP changes rapidly with each successive addition. The change in potential can be fit to a single exponential function shown by the red portion of the curve to yield a rise time of 200.4 ± 0.1 ms per addition.

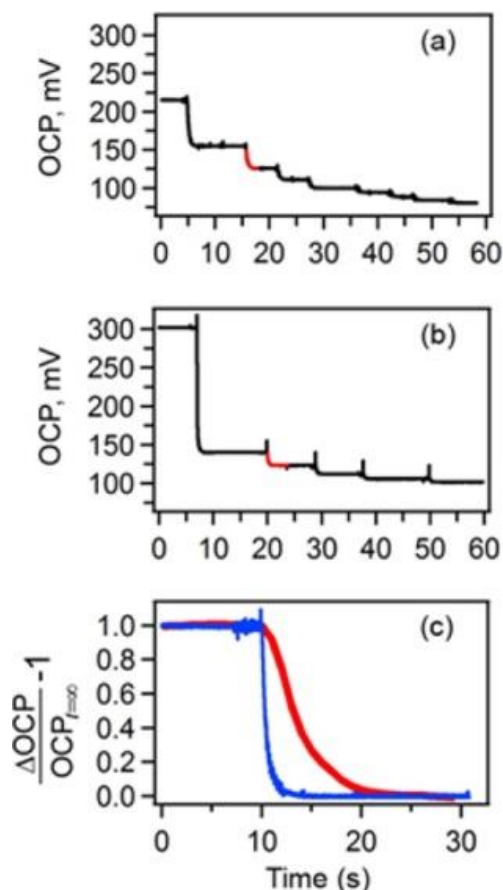


Figure 4.5. Reprinted with permission from reference 1. American Chemical Society Copyright 2016. OCP–time trace for (a) the addition of 5 mM potassium ferrocyanide to a receiving droplet containing 0.5 mM potassium ferricyanide and (b) the addition of 50 mM potassium ferrocyanide to a receiving droplet containing 5 mM potassium ferricyanide. With each addition, the voltage quickly changes and equilibrates. The red portion of both curves is a least-square fit to the data with a single exponential function with time constant $\tau = 302.1 \pm 0.2$ ms (a) and $\tau = 200.4 \pm 0.1$ ms (b). (c) The small droplets enable measurement of rapid kinetics. This is verified by comparing the time constant of the change in voltage for the droplet system (blue trace, $\tau = (0.51 \pm 0.01)$ s) and a large bulk electrode with a geometric area of 0.079 cm^2 in 17.1 mL of solution (red trace, $\tau = (4.1 \pm 0.3)$ s).

When the concentrations are small and/or when electron exchange rates are slow, equilibrium can take longer to be established.⁴⁴ However, similar behavior was observed upon addition of 5 mM $[\text{Fe}(\text{CN})_6]^{4-}$ to 0.5 mM $[\text{Fe}(\text{CN})_6]^{3-}$ in **Figure 4.5a**. In this case, the rise time increased only slightly to 302.1 ± 0.2 ms. Because of these rapid rise times (several hundred milliseconds), multiple additions can be made and an entire Nernst plot obtained over a short

period of time (<5 min). For comparison, a similar experiment was conducted using a traditional experimental system that consisted of a large electrode (geometric area = 0.079 cm²) and large volume (17 mL) of solution. The normalized OCP–time trace for the first addition (350 µL of [Fe(CN)₆]⁴⁻) to 17.1 mL of [Fe(CN)₆]³⁻ is directly compared to a similar trace recorded with the microdroplet experiment. The time constant for the large volume system is ~8× larger than that recorded using the microdroplet approach, **Figure 4.5c**. Because diffusion is involved, smaller length scales yield faster mixing times and significantly smaller time constants.⁴⁵

The feasibility of the potentiometric droplet-based system was evaluated using both one- and two-electron poised and unpoised redox reactions. The poised reaction refers to a system where both the oxidized (Ox) and reduced (Red) forms of a redox couple are present in appreciable concentrations while the unpoised reaction is a system with only the oxidized or reduced species present.⁴⁶ In both cases, the measured open-circuit potential is related to the concentration (activity) of oxidants and reductants as described by the Nernst Equation (**Eq.4.1**),

$$E = E^0 - \left(\frac{RT}{nF} \right) \ln \left(\frac{C_{\text{Red}}}{C_{\text{Ox}}} \right) \quad (4.1)$$

where E is the measured potential (with respect to a reference), E^0 is the standard reduction potential of the redox couple, R is the gas constant, F is Faraday's constant, n is the number of electrons transferred, and C_{Red} and C_{Ox} are the concentrations of the reduced and oxidized forms of the redox pair, respectively.⁴⁶ At our laboratory temperature of $T = 22$ °C, the prefactor RT/F reduces to 25.4 mV. A plot of potential vs $\log_{10}(C_{\text{red}}/C_{\text{ox}})$ should then yield a linear response with a slope of $2.303 \times 25.4 \text{ mV} = 58.6 \text{ mV}/n$ if the electrode responds in a Nernstian fashion. For a poised system, the intercept corresponds to the formal potential of the redox couple with respect to the reference electrode (in our case, Ag/AgCl in 0.10 M KCl).

4.3.2. Poised Redox Reactions

The first poised system chosen was that of $[\text{Fe}(\text{CN})_6]^{4-}/[\text{Fe}(\text{CN})_6]^{3-}$ in 0.1 M KCl as it has relatively facile electron transfer kinetics and is often used as an ORP calibrant.⁴⁷ Both high (5 mM) and low (0.5 mM) concentrations of $[\text{Fe}(\text{CN})_6]^{3-}$ were evaluated as were different receiving droplet sizes (290 to 620 pL). Once a droplet was placed on the electrode surface and the reference electrode was inserted, injection droplets in the range of 26 to 65 pL were added to the receiving droplet. The OCP–time traces (examples shown in **Figure 4.5**) were used to construct a Nernst plot and an example of which is shown in **Figure 4.6a** for receiving droplet sizes of 290, 470, and 620 pL. The rapid mixing of the droplets enables the acquisition of a Nernst plot in minutes. Plots of OCP vs $\log_{10}(C_{\text{red}}/C_{\text{ox}})$ obtained from six droplets yielded a Nernstian slope of -58.5 ± 3.8 mV with a y-intercept of 135.8 ± 12.8 mV. Slopes of these runs were all Nernstian and consistent with large volume experiments,^{34–36,48} regardless of the size of the receiving droplet or the sizes of individual injection droplets. Also, the experimental y-intercept of 423.8 ± 12.8 mV vs NHE is nearly the same as the theoretical value reported for ZoBell’s solution, a standard ORP calibrant, of 430 mV vs NHE.⁴⁷ Collectively, these results indicate that the droplet-based approach obeys the Nernst equation for the redox couple $[\text{Fe}(\text{CN})_6]^{4-}/[\text{Fe}(\text{CN})_6]^{3-}$. In addition, this approach works well for both high concentration and low concentrations. For example, a 10-fold reduction in the concentration of potassium ferri- and ferrocyanide yields an average slope of -57 mV with a correlation coefficient greater than 0.99.

To further validate this approach, another one-electron redox couple was investigated, $\text{Fe}^{2+}/\text{Fe}^{3+}$ in 0.1 M HCl. In contrast to $[\text{Fe}(\text{CN})_6]^{4-}/[\text{Fe}(\text{CN})_6]^{3-}$, the electron exchange rates are slower.⁴⁹ In this case, the receiving droplets ranging in diameter from 50 to 200 μm contained ferrous ammonium sulfate (5 mM). Injection droplets with diameters of 10–20 μm containing

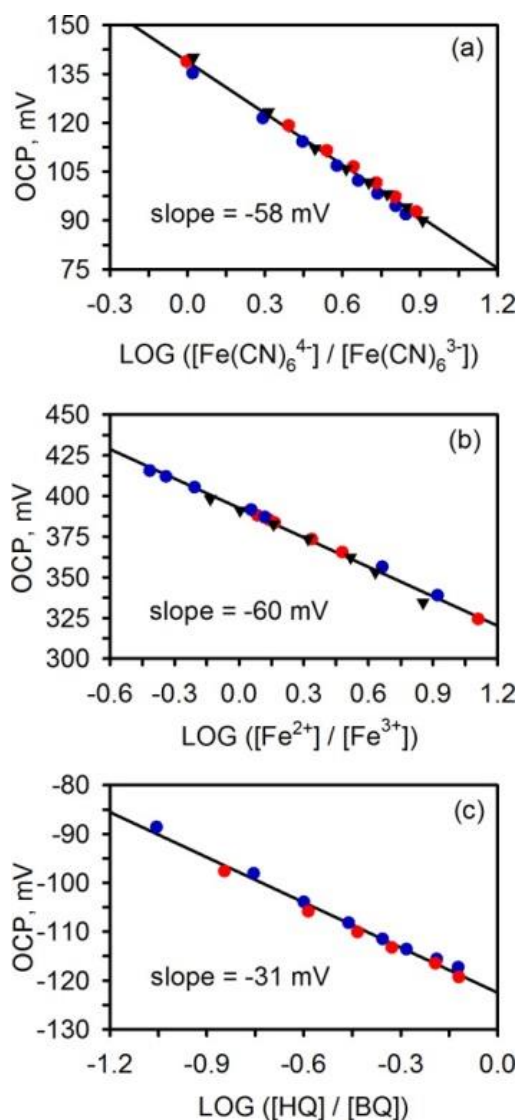


Figure 4.6. Reprinted with permission from reference 1. American Chemical Society Copyright 2016. Nernst plot for (a) potassium ferrocyanide ($[\text{Fe}(\text{CN})_6]^{4-}$) and ferricyanide ($[\text{Fe}(\text{CN})_6]^{3-}$) with receiving droplets of 290, 470, and 620 pL represented by the red circles (red ●), blue circles (blue ●), and black triangles (▼), respectively. (b) Ferrous (Fe^{2+}) and ferric (Fe^{3+}) ammonium sulfate with receiving droplets of 590, 290, and 640 pL represented by the red circles (red ●), blue circles (blue ●), and black triangles (▼), respectively, and (c) hydroquinone (HQ) and benzoquinone (BQ) with receiving droplets of 1000 pL for both run 1 (red circles, red ●) and run 2 (blue circles, blue ●). The solid line represents the linear regression fit to the data (solid points).

ferric ammonium sulfate (50 mM) were added. From OCP–time traces, a Nernst plot was generated from data collected using three separate runs. As is evident in **Figure 4.6b**, even with varying receiving droplet sizes of 280, 590, and 640 pL and a range of injection droplet sizes

($V = 2\text{--}22\text{ pL}$), all points overlap each other and follow Nernstian behavior. As with the $[\text{Fe}(\text{CN})_6]^{4-}/[\text{Fe}(\text{CN})_6]^{3-}$ redox couple, this one-electron transfer process yielded a slope of $-60.3 \pm 1.2\text{ mV}$ with a y-intercept of $392.7 \pm 0.6\text{ mV}$ and correlation coefficient of 0.992, nearly matching the expected -59.2 mV slope of an ideal Nernstian system (**Figure 4.6b**). Additionally, the individual y-intercepts for the three runs were 393, 392, and 394 mV, respectively, and are consistent with published values for Light's solution (values = 675 mV vs NHE or 387 mV vs Ag/AgCl (0.1 M KCl)), another commonly used ORP standard.⁵⁰ This further confirms that, at even very small or large droplet sizes, the modified nanoporous gold electrodes sensitively respond to changes in the concentration of the redox species in submicroliter droplets of solution. The third redox couple chosen for study was the two electron redox couple: hydroquinone and benzoquinone (HQ/BQ). This changes the value of n from 1 to 2 and should reduce the slope of the Nernstian plot by a factor of 2. In **Figure 4.6c**, a Nernst plot is shown for OCP values obtained from two different droplets, each with a volume of 1000 pL, and with injection droplets ranging from 8 to 17 pL. Consistent with a 2-electron process, a slope of $-30.8 \pm 0.9\text{ mV}$ and a y-intercept of $-122.4 \pm 0.5\text{ mV}$ with a correlation coefficient of 0.998 were obtained. Even with varying injection droplet sizes, the individual slopes and y-intercepts of each run were nearly identical.

4.3.3. Unpoised Redox Reactions

Measurement of OCPs in solutions that contain both forms of a redox couple is relatively straightforward in that equilibrium is reached rather quickly. Since most real systems do not necessarily contain both forms of a redox couple at appreciable concentrations, it is necessary to evaluate our current approach using unpoised systems where only one form of the redox couple is present in solution. In order to illustrate this, we first injected $[\text{Fe}(\text{CN})_6]^{3-}$ (5 mM in 0.1 M

KCl) droplets, ranging from 14 to 100 pL, into a 1400 pL receiving droplet of 0.1 M KCl. With each addition of $[\text{Fe}(\text{CN})_6]^{3-}$, the concentration in the receiving droplet increased, which elicited a change in the OCP. A plot of OCP vs $\log [1/[\text{Fe}(\text{CN})_6]^{3-}]$ yielded a slope of -60.6 ± 0.8 mV with a y-intercept of 202.2 ± 0.3 and a correlation coefficient of 0.999 (**Figure 4.7a**). Again, the slope of the curve is consistent with the Nernst equation and verifies the robust nature of the droplet-based technique when using only one redox active species in solution.

In order to show applicability to more biologically relevant redox couples, a 8200 pL receiving droplet of 0.1 M phosphate buffer (pH 7.4; 0.1 M KCl) was placed on the nanoporous gold electrode and injection droplets with volumes ranging between 180 and 450 pL containing 5.56 mM ascorbic acid (in pH 7.4, 0.1 M phosphate buffer) were added to it. With each addition of ascorbic acid to buffer, the OCP changed accordingly.

Figure 4.7b shows the Nernst plot constructed from this data. Unlike that observed for the previous redox couples, the Nernst plot is not linear over the entire concentration range. Rather, at low concentrations (from ~ 120 to ~ 700 μM), the data is linear with a slope of -29.1 ± 2.5 mV corresponding to a two-electron transfer process. At high concentrations, the data is also linear with a slope of -52.8 ± 0.5 mV corresponding to a one-electron transfer. The exact cut off between concentration regimes is electrode-to-electrode dependent. Out of 4 droplets, the slopes of the low and high concentration regimes were -28.8 ± 4.6 and -47.3 ± 4.5 mV, respectively. These two different slopes are not related to the microdroplet experiment as similar values were also observed using the traditional large volume experiment.³⁶ For example, with nanoporous gold using large volumes (10 mL), the slope was -30.1 ± 2.0 mV ($N = 4$) at low concentrations (100–300 μM). Planar gold had more variability with a slope of -40.8 ± 5.3 mV.³⁶ A previous potentiometric experiment on Pt reported a slope of 58.9 mV.⁵¹ The oxidation of ascorbic acid

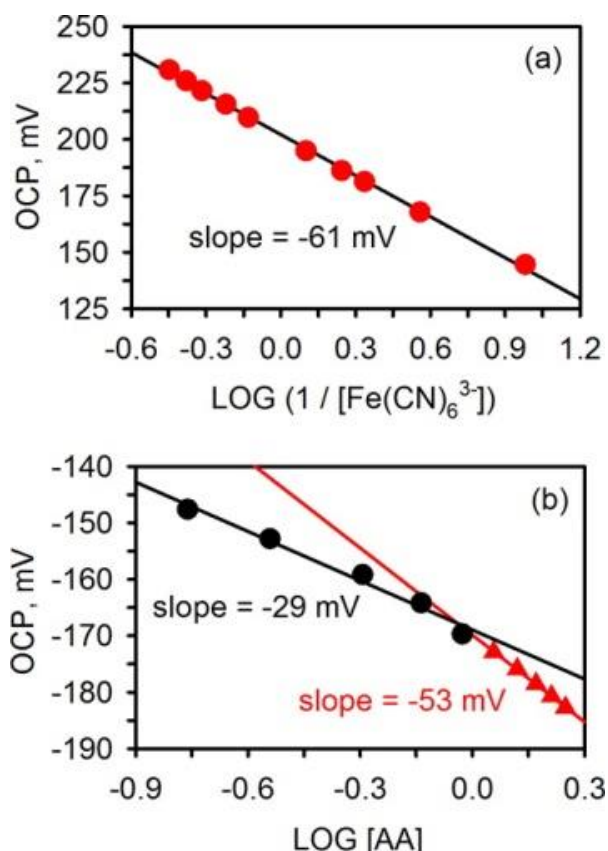


Figure 4.7. Reprinted with permission from reference 1. American Chemical Society Copyright 2016. Nernst plot for (a) potassium ferrocyanide ($[\text{Fe}(\text{CN})_6]^{4-}$) and ferricyanide ($[\text{Fe}(\text{CN})_6]^{3-}$) with receiving droplets of 290, 470, and 620 pL represented by red circles (red ●), blue circles (blue ●), and black triangles (▼), respectively. (b) Ferrous (Fe^{2+}) and ferric (Fe^{3+}) ammonium sulfate with receiving droplets of 590, 290, and 640 pL represented by the red circles (red ●), blue circles (blue ●), and black triangles (▼), respectively, and (c) hydroquinone (HQ) and benzoquinone (BQ) with receiving droplets of 1000 pL for both run 1 (red circles, red ●) and run 2 (blue circles, blue ●). The solid line represents the linear regression fit to the data (solid points).

should be a two-electron, 2H^+ reaction on gold,⁵² but it is mechanistically more complicated than that observed for potassium ferricyanide.^{52,53} Reversible surface adsorption is also known to occur on Pt and Au.^{53,54} Also, oxidation of ascorbic acid by oxygen diffusing in and out of the hexadecane layer is possible. The differences observed for the low vs higher concentration could be related to surface adsorption (which will be more problematic at high concentrations). However, we cannot rule out at the present time that a different mechanism may be operative at these two different concentration ranges.

4.4. Conclusions

The ability to make potentiometric measurements in solutions at the nanoscale have allowed for rapid, sensitive, and accurate measurements of the redox potential of solutions containing one or both forms of a redox couple. In this work, the optical transparency as well as the efficient electron transfer kinetics of modified nanoporous gold electrodes has been exploited to conduct potentiometric experiments in the solution volume range of 1400 down to 280 pL droplets. Additionally, when comparing experimental y-intercept values to those of standard ORP calibrants, these electrodes show they are near ideal and well suited for situations where only minute sample volumes are available for testing including medical, food, and environmental applications. Given the rapid equilibration time as well as the short time it takes to add an injection droplet into the receiving droplet, the ability to construct an accurate Nernst plot of these “poised” and “unpoised” systems is on the scale of less than 1 min. Once the electrode has shown to be responsive to the receiving solution of interest due to its optimal hydrophobicity, the only time determining factor is the mixing time of the injection droplet with the receiving droplet. Since this has been shown to be on the scale of ~300 ms, a series of additions (6–10) can be performed extraordinarily quickly. The fast mixing time and the ability of these electrodes to behave in a Nernstian fashion lends support to using these measurements in situations where time and limited sample volumes are of critical importance. Such examples may include microtitrations^{21,22} and measurement of redox potentials of microscopic solutions such as blood and blood products.³⁶

4.5. References

1. Freeman, C. J., Farghaly, A. A., Choudhary, H., Chavis, A. E., Brady, K. T., Reiner, J. E. and Collinson, M. M. Microdroplet-Based Potentiometric Redox Measurements on Gold Nanoporous Electrodes. *Anal. Chem.* **88**, 3768–3774 (2016).
2. Laurell, T., Nilsson, J. and Marko-Varga, G. The Quest for High- Speed and Low- Volume Bio- analysis. *Anal. Chem.* **77**, 264 A-272A (2005).
3. Li, T. and Hu, W. Electrochemistry in nanoscopic volumes. *Nanoscale* **3**, 166–76 (2011).
4. Li, C. M. and Hu, W. Electroanalysis in micro- and nano-scales. *J. Electroanal. Chem.* **688**, 20–31 (2013).
5. Petra S. Dittrich, Kaoru Tachikawa, and and Manz, A. Micro Total Analysis Systems. Latest Advancements and Trends. 3887–3908 (2006). doi:10.1021/AC0605602
6. Li, T., Su, L., Hu, W., Dong, H., Li, Y. and Mao, L. Femtoliter and attoliter electrochemical cells on chips. *Anal. Chem.* **82**, 1521–1526 (2010).
7. Nakatani, K., Sudo, M. and Kitamura, N. A study on liquid-liquid distribution based on single picoliter droplets and in situ electrochemical measurements. *Anal. Chem.* **72**, 339–342 (2000).
8. Miller, T. S., Macpherson, J. V. and Unwin, P. R. Dual-electrode measurements in a meniscus microcapillary electrochemical cell using a high aspect ratio carbon fibre ultramicroelectrode. *J. Electroanal. Chem.* **729**, 80–86 (2014).
9. Neugebauer, S., Evans, S. R., Aguilar, Z. P., Mosbach, M., Fritsch, I. and Schuhmann, W. Analysis in Ultrasmall Volumes: Microdispensing of Picoliter Droplets and Analysis without Protection from Evaporation. *Anal. Chem.* **76**, 458–463 (2004).
10. Spaine, T. W. and Baur, J. E. A positionable microcell for electrochemistry and scanning electrochemical microscopy in subnanoliter volumes. *Anal. Chem.* **73**, 930–938 (2001).
11. Sun, P. and Mirkin, M. V. Electrochemistry of individual molecules in zeptoliter volumes. *J. Am. Chem. Soc.* **130**, 8241–8250 (2008).
12. Vandaveer IV, W. R. and Fritsch, I. Measurement of ultrasmall volumes using anodic stripping voltammetry. *Anal. Chem.* **74**, 3575–3578 (2002).
13. Yum, K., Cho, H. N., Hu, J. and Yu, M. F. Individual nanotube-based needle nanopores for electrochemical studies in picoliter microenvironments. *ACS Nano* **1**, 440–448 (2007).
14. Banks, C. E., Davies, T. J., Evans, R. G., Hignett, G., Wain, A. J., Lawrence, N. S., Wadhawan, J. D., Marken, F. and Compton, R. G. Electrochemistry of immobilised redox droplets: Concepts and applications. *Phys. Chem. Chem. Phys.* **5**, 4053 (2003).
15. Davies, T. J., Wilkins, S. J. and Compton, R. G. The electrochemistry of redox systems within immobilised water droplets. *J. Electroanal. Chem.* **586**, 260–275 (2006).
16. Jimenez, A. I. P., Challier, L., Di Pisa, M., Guille-Collignon, M., Lemaître, F., Lavielle, S., Mansuy, C., Amatore, C., Labbé, E. and Buriez, O. Three-electrode analytical and preparative electrochemistry in micro-volume hanging droplets. *Electrochem. commun.* **54**, 41–45 (2015).
17. Clark, R. A., Hietpas, P. B. and Ewing, A. G. Electrochemical Analysis in Picoliter Microvials. *Anal. Chem.* **69**, 259–263 (1997).
18. Willman, K. W. and Murray, R. W. Contact Angle between Water and a Poly(vinylferrocene) Film on a Potential-Controlled Platinum Electrode. *Anal. Chem.* **55**, 1139–1142 (1983).
19. Tantra, R. and Manz, A. Integrated potentiometric detector for use in chip-based flow

- cells. *Anal. Chem.* **72**, 2875–2878 (2000).
20. Kashyap, R. and Gratzl, M. Electrochemistry in Microscopic Domains. 1. The Electrochemical Cell and Its Voltammetric and Amperometric Response. *Anal. Chem.* **70**, 1468–1476 (1998).
 21. Yi, C., Huang, D. and Gratzl, M. Complexometric determination of metal ions by microscopic diffusional titration. *Anal. Chem.* **68**, 1580–1584 (1996).
 22. Yi, C. and Gratzl, M. Diffusional Microtitration: Reagent Delivery by a Diffusional Microburet into Microscopic Samples. *Anal. Chem.* **66**, 1976–1982 (1994).
 23. Ball, J. C., Scott, D. L., Lumppp, J. K., Daunert, S., Wang, J. and Bachas, L. G. Electrochemistry in nanovials fabricated by combining screen printing and laser micromachining. *Anal. Chem.* **72**, 497–501 (2000).
 24. Caldeo, V. and McSweeney, P. L. H. Changes in oxidation-reduction potential during the simulated manufacture of different cheese varieties. *Int. Dairy J.* **25**, 16–20 (2012).
 25. Copeland, A. and Lytle, D. A. Measuring the oxidation-reduction potential of important oxidants in drinking water. *J. Am. Water Works Assoc.* **106**, E10–E20 (2014).
 26. Fiedler, S., Vepraskas, M. J. and Richardson, J. L. *Soil Redox Potential: Importance, Field Measurements, and Observations. Advances in Agronomy* **94**, (Elsevier Masson SAS, 2007).
 27. Goncharuk, V. V., Bagrii, V. A., Mel'nik, L. A., Chebotareva, R. D. and Bashtan, S. Y. The use of redox potential in water treatment processes. *J. Water Chem. Technol.* **32**, 1–9 (2010).
 28. Jang, A., Lee, J. H., Bhadri, P. R., Kumar, S. A., Timmons, W., Beyette, F. R., Papautsky, I. and Bishop, P. L. Miniaturized redox potential probe for in situ environmental monitoring. *Environ. Sci. Technol.* **39**, 6191–6197 (2005).
 29. Goldin, M. M., Romasenko, M. V., Volkov, A. G., Hall, P. J., Evseev, A. K., Levina, O. A., Aleschenko, E. I. and Krylov, V. V. Redox Potentials of Blood Serum in Patients with Acute Cerebral Pathology. *ECS Trans.* **25**, 63–71 (2010).
 30. Noyhouzer, T., Kohen, R. and Mandler, D. A new approach for measuring the redox state and redox capacity in milk. *Anal. Methods* **1**, 93 (2009).
 31. Zelada-Guillén, G. A., Bhosale, S. V., Riu, J. and Rius, F. X. Real-time potentiometric detection of bacteria in complex samples. *Anal. Chem.* **82**, 9254–9260 (2010).
 32. Blaz, T., Baś, B., Kupis, J., Migdalski, J. and Lewenstam, A. Multielectrode potentiometry in a one-drop sample. *Electrochem. commun.* **34**, 181–184 (2013).
 33. Bekker, E. *Environmental Analysis by Electrochemical Sensors and Biosensors*. (Springer Science+Business Media, 2014).
 34. Noyhouzer, T., Valdinger, I. and Mandler, D. Enhanced potentiometry by metallic nanoparticles. *Anal. Chem.* **85**, 8347–8353 (2013).
 35. Kuhlmann, J., Dzugan, L. C. and Heineman, W. R. Comparison of the Effects of Biofouling on Voltammetric and Potentiometric Measurements. *Electroanalysis* **24**, 1732–1738 (2012).
 36. Farghaly, A. a., Lam, M., Freeman, C. J., Uppalapati, B. and Collinson, M. M. Potentiometric Measurements in Biofouling Solutions: Comparison of Nanoporous Gold to Planar Gold. *J. Electrochem. Soc.* **163**, H3083–H3087 (2016).
 37. Collinson, M. M. Nanoporous Gold Electrodes and Their Applications in Analytical Chemistry. *ISRN Anal. Chem.* **2013**, 1–21 (2013).
 38. Seker, E., Reed, M. L. and Begley, M. R. Nanoporous gold: Fabrication, characterization,

- and applications. *Materials (Basel)*. **2**, 2188–2215 (2009).
39. Patel, J., Radhakrishnan, L., Zhao, B., Uppalapati, B., Daniels, R. C., Ward, K. R. and Collinson, M. M. Electrochemical properties of nanostructured porous gold electrodes in biofouling solutions. *Anal. Chem.* **85**, 11610–11618 (2013).
 40. Saraf, S., Neal, C. J., Park, S., Das, S., Barkam, S., Cho, H. J. and Seal, S. Electrochemical study of nanoporous gold revealing anti-biofouling properties. *RSC Adv.* **5**, 46501–46508 (2015).
 41. Park, S., Kim, H. C. and Chung, T. D. Electrochemical analysis based on nanoporous structures. *Analyst* **137**, 3891 (2012).
 42. Ciesielski, P. N., Scott, A. M., Faulkner, C. J., Berron, B. J., Cliffel, D. E. and Jennings, G. K. Functionalized Nanoporous Gold Leaf Photosystem I. *ACS Nano* **2**, 2465–2472 (2008).
 43. Daggumati, P., Matharu, Z., Wang, L. and Seker, E. Biofouling-Resilient Nanoporous Gold Electrodes for DNA Sensing. *Anal. Chem.* **87**, 8618–8622 (2015).
 44. Peiffer, S., Klemm, O., Pecher, K. and Hollerung, R. Redox measurements in aqueous solutions - A theoretical approach to data interpretation, based on electrode kinetics. *J. Contam. Hydrol.* **10**, 1–18 (1992).
 45. Janasek, D., Franzke, J. and Manz, A. Scaling and the design of miniaturized chemical-analysis systems. *Nature* **442**, 374–380 (2006).
 46. Bard, A. J. and Faulkner, L. R. *Electrochemical Methods: Fundamentals and Applications*. (John Wiley and Sons, Inc., 1980).
 47. Teasdale, P. R., Minett, A. I., Dixon, K., Lewis, T. W. and Batley, G. E. Practical improvements for redox potential (E(H)) measurements and the application of a multiple-electrode redox probe (MERP) for characterising sediment in situ. *Anal. Chim. Acta* **367**, 201–213 (1998).
 48. Wu, N. Y., Zang, Y. B., Gao, W. and Xu, M. T. Zero current potentiometry for measuring the interface potential at the electrode/solution interface: Theoretical and experimental study. *Electroanalysis* **25**, 2175–2180 (2013).
 49. Jia, F., Yu, C., Ai, Z. and Zhang, L. Fabrication of nanoporous gold film electrodes with ultrahigh surface area and electrochemical activity. *Chem. Mater.* **19**, 3648–3653 (2007).
 50. Light, T. S. Standard solution for redox potential measurements. *Anal. Chem.* **44**, 1038–1039 (1972).
 51. Rael, L. T., Bar-Or, R., Kelly, M. T., Carrick, M. M. and Bar-Or, D. Assessment of Oxidative Stress in Patients with an Isolated Traumatic Brain Injury Using Disposable Electrochemical Test Strips. *Electroanalysis* **27**, 2567–2573 (2015).
 52. Rueda, M., Aldaz, A. and Sanchez-Burgos, F. Oxidation of L-ascorbic acid on a gold electrode. *Electrochim. Acta* **23**, 419–424 (1978).
 53. Pisoschi, A. M., Pop, A., Serban, A. I. and Fafaneata, C. Electrochemical methods for ascorbic acid determination. *Electrochim. Acta* **121**, 443–460 (2014).
 54. Brezina, M., Koryta, J., Loucka, T., Marsikova, D. and Pradac, J. Adsorption and Kinetics of Oxidation of Ascorbic Acid At Platinum Electrodes. *J. Electroanal. Chem. Interfacial Electrochem.* **40**, 13–17 (1972).

Chapter 5

Electrochemical Applications of Fabricated Mini-Nanoporous Gold (mNPG) and Platinum-Speckled Mini-Nanoporous Gold (mNPG-Pt) Electrodes

5.1. Introduction

Potentiometry is a relatively simple measurement technique commonly used to measure the concentration of an ion in solution. The most popular potentiometric measurement is the measurement of pH using a pH electrode. Most potentiometric experiments utilize a membrane based ion selective electrode (pH electrode) specifically designed to be selective toward a given ion (H^+) in solution. A less common approach involves the use of an inert metallic indicating electrode that will respond to any redox molecule present in a high enough concentration in

$$E = E^0 - \left(\frac{RT}{nF} \right) \ln \left(\frac{C_{\text{Red}}}{C_{\text{Ox}}} \right) \quad (5.1)$$

solution that is able to exchange electrons with the electrode surface. For a simple solution that contains both forms of a redox couple, the measured potential can be equated to the Nernst equation (**Eq. 1**). In this equation, E is the measured potential (with respect to a reference electrode), E^0 is the standard reduction potential of the redox couple, R is the gas constant, F is Faraday's constant, n is the number of electrons transferred, and C_{Red} and C_{Ox} are the concentrations of the reduced and oxidized forms of the redox pair, respectively.¹ For a solution that contains several redox species, however, the measured potential is a 'mixed' potential and depends in a complex fashion on the redox molecules present in solution, their concentration, and the rates of electron transfer with the electrode surface.^{2,3} Mixed potentials can provide valuable information about the redox state of a sample and has been used to evaluate soil systems, water systems, plasma and blood.⁴⁻⁷

In order to improve the value of such redox potential measurements in real complex samples, several measurement challenges need to be addressed. These challenges include the

ability to make redox potential measurements in small volumes (microliters) and in the presence of matrix elements that may adsorb on the electrode surface and reduce the electrochemical response. Also, the sensitivity of the electrode toward multiple redox species needs to be enhanced. One means to reduce the effect of matrix elements on the electrochemical response of the electrode involves using nanoporous gold electrodes.⁸ We have recently shown that these electrodes are able to make redox potential measurements in the presence of proteins known to biofoul the electrode surface.⁹ These electrodes are able to do this by a unique biosieving like mechanism where small redox molecules can enter into the small pores of the nanoporous gold electrodes to exchange electrons whereas large proteins are not able to. The focus of the present work lies on miniaturizing and improving the response of the electrode so that redox potential measurements can be made in sub-milliliter volumes with enhanced sensitivity.

One of the most simple and cost effective approaches to prepare NPG involves the use of commercially available gold leaf and chemical dealloying it in nitric acid. Varying both the ratio of gold to silver from $\text{Ag}_{0.75}\text{Au}_{0.25}$ to $\text{Ag}_{0.25}\text{Au}_{0.75}$ (6 to 18 carat, respectively) in the gold leaf as well as the dealloying time, provides a simple method to control pore size. In this work, we will focus on 12 Karat gold leaf ($\text{Ag}_{0.50}\text{Au}_{0.50}$) that is chemically dealloyed in concentrated nitric acid whereas the silver is removed, causing the gold to restructure forming a 3D-bicontinuous framework of interconnected pores and ligaments. When the silver selectively dissolves a highly porous material that can be used as the active electrode area is created.

Typically, in the fabrication of NPG, the dealloyed gold leaf is placed on a conducting substrate (e.g., a gold coated slide) in order to make the electrode. However, the gold slides are expensive and not flexible, which limits applications. Thus, there is a strong need to incorporate other, low-cost substrates to replace the high cost gold slide electrode. One approach involves

making NPG electrodes on glass.^{10,11} To improve the adherence of gold to glass, a linker can be used. In previous work, (3-mercaptopropyl) trimethoxysilane was used as a linker to adhere the gold leaf to a microscope cover slip.¹¹ Replacing the gold substrate using glass functionalized with a thiol group (-SH) not only reduces the cost and provides optical transparency, but also has an added benefit of having an electrode support that can take on a variety of shapes such as a capillary while ensuring its durability. Reducing the geometric dimensions allows for rapid testing due to small sample volumes and multiplexing into lab-on-chip based sensing platforms. These electrodes can be used with 100 μ L solution volumes without the need for additional electrode modification or sample preparation. Analysis using microliter drop size volumes (\sim 100 μ L) supports the fabrication of low-cost materials that are sensitive to a large number of biologically relevant molecules.

In order to improve the sensitivity of the electrodes to multiple species, many groups have worked to modify the electrode surface. Adding a monolayer of ferrocene-terminated thiols,^{12,13} phenyl groups via reduction of diazonium salts,¹⁴ or immobilizing a protein, like glucose oxidase,¹⁵ can amplify the signal response in the presence target molecules. Another method to increase responsiveness of an electrode to multiple species is to incorporate another conductive material to the electrode as eloquently shown by Mandler and coworkers.³ In their work, platinum nanoparticles were deposited on a stainless steel substrate with gold nanoparticles. Gold nanoparticles showed a diminished response in the presence of two redox molecules (l-dopa and l-dopac). After platinum deposition, an increased response to these molecules was shown as a Nernstian response to a one-electron transfer system.

Platinum has received considerable attention because of its electrocatalytic properties.^{16–}

¹⁸ The deposition of platinum onto an electrode surface has been reported using a polystyrene

sphere template. The spheres are monodispersed onto a gold substrate and platinum is electrodeposited onto the voids created by the spheres producing a macroporous platinum film.¹⁹ Ding et al. used a porous substrate, nanoporous gold, in order to form a thin layer of platinum covering a nanoporous gold surface. This was accomplished with the reduction of chloroplatinic acid (H_2PtCl_6) using hydrazine vapor where the gold was placed at the interface.²⁰ Also, bulk gold that is reduced by ascorbic acid to produce a porous surface was coated with platinum via the electrodeposition of the platinum salt, potassium tetrachloroplatinate (K_2PtCl_4)²¹. Alternatively, the fabrication of Au-Pt nanoparticles using gold and platinum acid solutions,²² bimetallic Au-Pt nanocomposite films constructed via alternating Au and Pt nanoparticle layers,²³ binary Pt-Au alloys prepared by co-electrodeposition,²⁴ and electrochemical etching of Cu in Au/Pt/Cu alloys²⁵ have produced Au-Pt alloys of varying compositions. To maintain a low-cost model for electrode fabrication, the amount of platinum used needs to be kept as low as possible.

Herein, we report the fabrication of functionalized glass capillary, nanoporous gold electrodes, and the validation of these electrodes using ferricyanide and ferrocyanide as the ORP calibrant. The potentiometric response of the electrodes in the presence of ascorbic acid (AA), cysteine (Cys), and uric acid (UA) were also measured in addition to glucose and hydrogen peroxide (H_2O_2). These molecules each have different interactions with electrode materials and all contribute to overall health and well-being. The response of the electrodes in the presence of glucose and hydrogen peroxide was enhanced through the incorporation of platinum into the nanoporous gold framework using a low concentration of platinum salt and very short deposition time of 2 seconds. The three-dimensional geometry of the capillary electrodes allowed all

measurements to be conducted using a single drop of solution (100 μ L) which eliminates the need for instrumentation that is more complex or requires specialized training.

5.2. Experimental Methods

5.2.1. Materials

Potassium ferricyanide, potassium phosphate dibasic, and glucose (97%) were obtained from Sigma Aldrich (St. Louis, MO). Potassium tetrachloroplatinate (46-47% Pt) and *l*-cysteine (99%) were purchased from Acros Organics (Morris, NJ). Potassium ferrocyanide was obtained from Mallinckrodt Chemicals (Phillipsburg, NJ). Potassium phosphate monobasic, hexanes, concentrated nitric acid, potassium chloride, L-ascorbic acid, hydrogen peroxide (30% in water), concentrated sulfuric acid were purchased from Fisher Scientific (Fair Lawn, NJ). Ethanol (200 proof) was obtained from Pharma-Aaper (Shelbyville, KY). Uric acid (99%) and (3-mercaptopropyl) trimethoxysilane (95%) were purchased from Alfa Aesar (Ward Hill, MA). Potassium hydroxide was obtained from Amresco (Solon, OH). Water (18 M Ω cm) was purified using a Millipore water purification system. All reagents were used as received and reagent solutions were made fresh.

5.2.2 Capillary Tube Functionalization and Nanoporous Gold Preparation

An established method of glass functionalization and NPG preparation¹⁰ was adopted to functionalize glass capillary tubes. Glass hematocrit capillary tubes (ID 1.5 mm) were flame sealed and then sonicated for 10 min in ethanol followed by deionized water for 10 min and dried with N₂ gas. Capillary tubes were then O₂ plasma cleaned using a Southbay, PE 2000 plasma etcher at 20 W for 5 min by placing tubes into a clean glass vial with desired end face-up in the stainless steel chamber. Cleaned tubes were then soaked with the plasma cleaned side

facing down in a 10 mM (3-mercaptopropyl)trimethoxysilane (MPTMS) in hexanes solution for 1 h in a 60 °C water bath. The capillary tubes were then rinsed with hexanes and left to dry. Manetti 12K gold leaf (FineArtStore, book of 25 loose leaves) was chemically dealloyed in concentrated nitric acid for 13 min and then floated on DI water twice for ~5 minutes. Conducting copper (Cu) tape (Ted Pella, PN 16072) was attached to the tube leaving the functionalized end exposed (~5 mm), which was then used to capture one dealloyed leaf ensuring the gold contacted both the copper lead and the functionalized glass covering the rounded tip. The dealloyed gold was dried with nitrogen and further cleaned by UV radiation (254 nm, 20 W) for 24 h by placing the electrode face up in a home-built box ~10 cm from the UV source. For testing, mini-NPG (mNPG) electrodes were wrapped securely with Parafilm to expose 1.5 mm.

5.2.3. Electrochemical Measurements

Open-circuit potential (OCP) measurements were conducted using a two-electrode cell with the mNPG electrode as working electrode and AgCl coated Ag wire as the reference electrode using a CH Instruments 1200A potentiostat. Given the small volumes of the initial receiving solution (100 μ L), a 1.5 mL centrifuge tube was cut at the 0.5 mL mark (**Figure 5.1**) and used as the electrochemical cell. To decrease the effects of evaporation, the cell was covered with Parafilm.

Platinum incorporation into dealloyed nanoporous gold was first attempted using a 20 mM potassium tetrachloroplatinate salt solution in 0.5 M H₂SO₄, similar to the procedure reported by Wang and coworkers.²¹ The method involved submerging a planar gold electrode into the platinum solution and cycling the potential from -0.2 V to 0.5 V (vs Ag/AgCl) at 10 mV/s. Due to the complete coverage of the electrode after one cycle of deposition, the potential

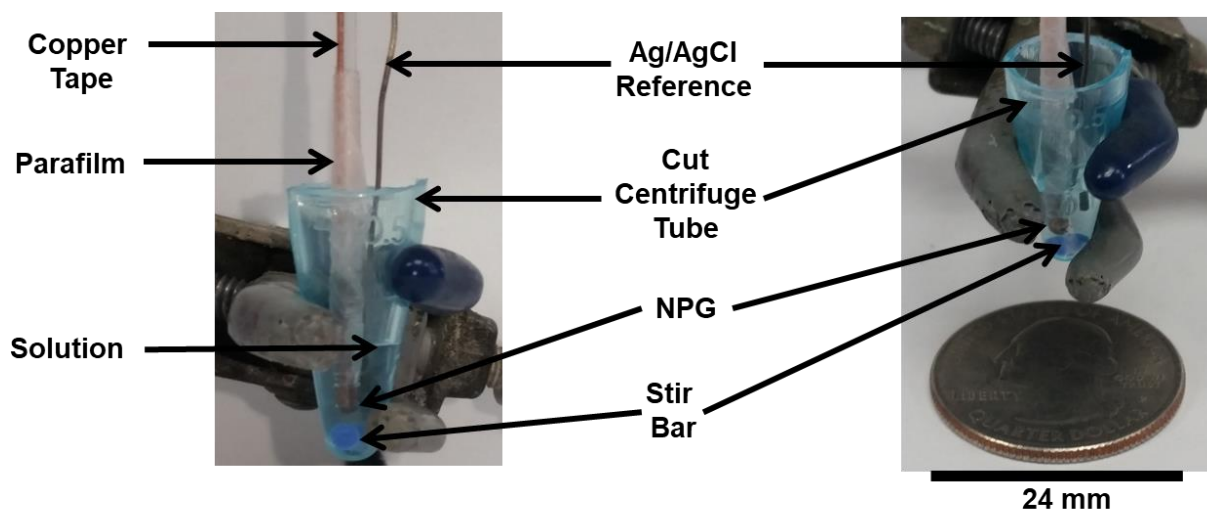


Figure 5.1. Optical images of electrochemical cell showing mNPG as working electrode and bare Ag/AgCl wire as reference electrode in a cut 1.5 mL centrifuge tube. All electrochemical measurements were conducted in a solution volume of 100 μL .

sweep method was replaced with chronoamperometric deposition. A series of optimization steps consisted first of decreasing deposition time from 120 seconds down to 2 seconds. However, even at 2 seconds of deposition, the planar gold electrode was still showing complete platinum coverage. The concentration was then decreased from 20 mM down to 0.75 mM with a 2-second deposition. The platinum deposition method was finalized at a set potential of -0.2 V for only 2 seconds using a 0.75 mM concentration of K_2PtCl_4 in 0.5 M H_2SO_4 . In this experiment, a traditional three-electrode cell was used by introducing a platinum wire as the auxiliary electrode.

5.2.4. Electrode Characterization

Surface area measurements of mNPG electrodes, before and after platinum deposition, were obtained using cyclic voltammetry (CV) in 0.5 M H_2SO_4 with a potential window of -0.2 to 1.4 V, with a scan rate of 100 mV/s, using a three-electrode cell. The surface morphology of the dealloyed nanoporous gold electrodes was investigated without and with deposited platinum using a field emission scanning electron microscope (FE-SEM, HITACHI SU-70). The

compositions of mNPG electrodes (with and without platinum) were determined using X-ray photoelectron spectroscopy (XPS) using a monochromatic Al K α (1486.68 eV) X-ray source (ThermoFisher ESCA lab 250) with a beam size of 0.5 mm, pass energy of 20 eV and step size of 0.1 eV. Samples were cleaned using Ar plasma to remove any possible contaminants. Data was analyzed using Advantage software.

5.3. Results and Discussion

5.3.1. Electrode Validation and Redox Molecule Response

In order to ensure electrodes were behaving according to the Nernst equation, mini-NPG electrodes were validated using a standard oxidation-reduction potential (ORP) calibrant redox couple: ferricyanide ($[\text{Fe}(\text{CN})_6]^{3-}$) and ferrocyanide ($[\text{Fe}(\text{CN})_6]^{4-}$). Both the mNPG working electrode and Ag/AgCl reference electrode were placed in an initial solution containing the oxidized form (5 mM $[\text{Fe}(\text{CN})_6]^{3-}$ in 0.1 M PBS with 0.1 M KCl as electrolyte) and the potential was measured. This is seen as the first step shown in **Figure 5.2a** indicated by the **blue** arrow. The potential takes a while to level out or equilibrate given that only the oxidized form is present, also known as an unpoised system. After a predetermined amount of time, 100 seconds, an aliquot of the reduced form, $[\text{Fe}(\text{CN})_6]^{4-}$ (50 mM) also in 0.1 M PBS, was added represented by the **red** arrow in **Figure 5.2a**. Upon the addition, the potential becomes more negative and quickly equilibrates. Prior to the next addition of $[\text{Fe}(\text{CN})_6]^{4-}$, an average is calculated using the potential for the last 15 seconds prior to addition. Now, both the oxidized ($[\text{Fe}(\text{CN})_6]^{3-}$) and reduced ($[\text{Fe}(\text{CN})_6]^{4-}$) forms of this redox couple are present. The system is said to be poised and has a more stable measured potential similar to the presence of a buffer solution to stabilize pH. In addition to an increase in concentration of $[\text{Fe}(\text{CN})_6]^{4-}$ with each addition, there is also a

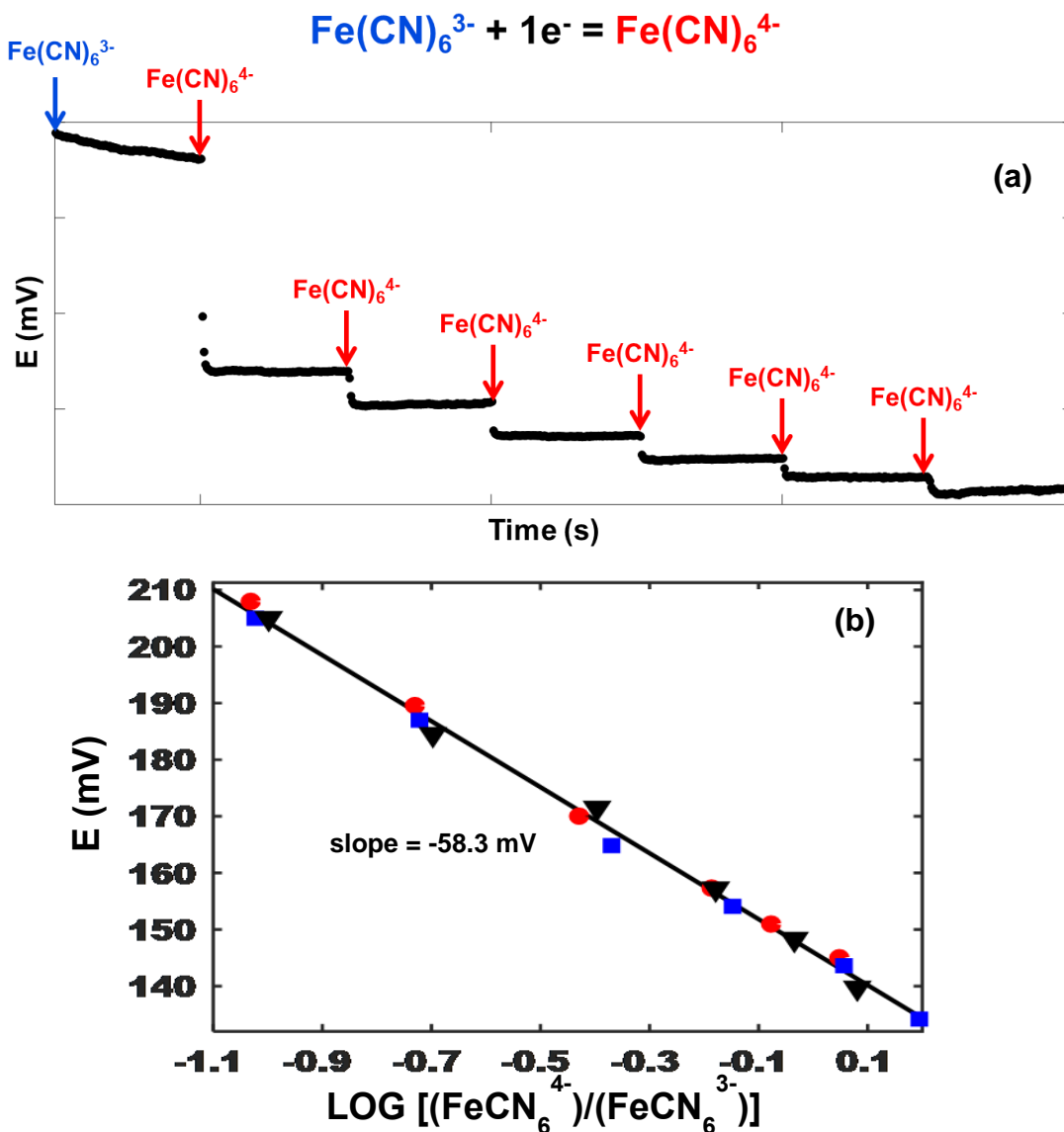


Figure 5.2. (a) Open-circuit potential (OCP) time trace of the additions of ferrocyanide to a ferricyanide receiving solution using a mini-nanoporous gold (mNPG) electrode. (b) Nernst plot constructed from time traces such as that shown in (a). Each symbol represents a separate experiment using a different mNPG electrode. A slope of -58.3 mV was obtained with a y-intercept of 146.0 mV. Correlation coefficient = 0.9965.

corresponding decrease in the $[\text{Fe(CN)}_6]^{3-}$ concentration due to dilution. Using the starting and final volumes of the receiving solution and the total volume of addition solution at each interval, the ratio of the reduced form to the oxidized form ($[\text{Fe(CN)}_6]^{4-} / [\text{Fe(CN)}_6]^{3-}$) can be determined at each potential step.

The logarithm of the ratio of the concentration of the two species was used to construct the Nernst plot shown in **Figure 5.2b**. The slope was calculated from linear regression ($R^2 = 0.9965$) on three data sets as -58.3 ± 0.8 mV with a y-intercept of 146.0 ± 0.5 mV. The slope agrees with what is expected for a one electron transfer system behaving in a Nernstian fashion (-59.2 mV). Also, the y-intercept of 146 mV vs Ag/AgCl agrees with the expected value of 142 mV for the formal potential of ferricyanide-ferrocyanide.²⁶

Once the capillary electrodes were validated, the Nernstian response of the electrodes to biologically relevant redox molecules (ascorbic acid, uric acid, and cysteine) was investigated. These systems are more complicated than those obtained for ferri- and ferrocyanide not only because the electrochemistry is more complex but also because these solutions are unpoised. This causes a larger potential change seen with each addition of redox aliquots, similar to the addition of an acid to an unbuffered solution. In open-circuit potential measurements, the redox active molecules in solution will come to an electrochemical equilibrium with the electrode. Electrons are exchanged where a small amount of the molecule will be either oxidized or reduced, then returned to its original state until a steady-state is reached. The presence of a redox pair reduces the miniscule concentration fluctuation that occurs during the steady-state. The lack of this reduction due to the system being unpoised is evidenced as a slight increase in potential variability over the course of equilibration at each step. This variability can be attributed to a combination of electron transfer kinetics of the redox species and whether the system is poised or unpoised.

Figure 5.3a shows a representative OCP time trace for the addition of ascorbic acid. An initial volume of 100 μ L of 0.1 PBS, with 0.1 M KCl as electrolyte, was pipetted into a cut

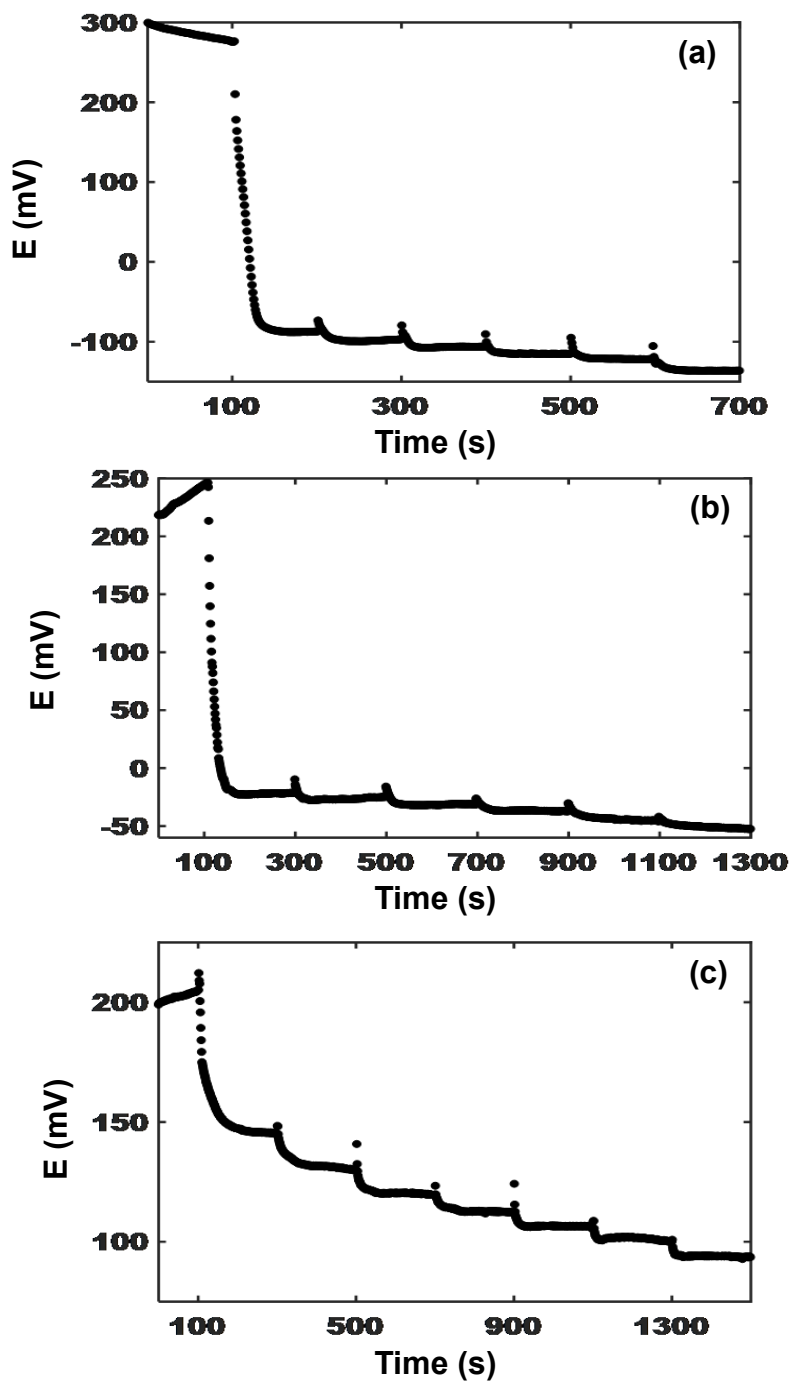


Figure 5.3. Open-circuit potential (OCP) time traces for the addition of aliquots of (a) ascorbic acid (AA) every 100 seconds, (b) cysteine (Cys) every 200 seconds, and (c) uric acid (UA) every 100 seconds, respectively, to a 100 μ L solution of 0.1 M PBS (0.1 M KCl as electrolyte, pH = 7.4) following an initial wait time of 100 seconds. Potential was measured using a mini-nanoporous gold (mNPG) electrode as the working electrode and Ag/AgCl as the reference electrode.

centrifuge tube (shown in **Fig. 5.1**) with a small stir bar. A mNPG electrode was placed into the solution and was used as the working electrode. The reference electrode (Ag/AgCl) was then inserted into the solution, ensuring both electrodes were not touching. The solution was stirred and the potential was measured. After 100 seconds, an aliquot of ascorbic acid dissolved in 0.1 M PBS was pipetted into the solution and the potential changed, seen as a large drop in potential right after 100 seconds. As the solution and electrode equilibrate, the potential levels out and shows little variation prior to the next addition. Cysteine and uric acid experiments were conducted in a similar fashion, except due to the longer equilibration times of these redox molecule, each addition was performed every 200 seconds, again following an initial wait time of 100 seconds (**Fig. 5.3b&c**). With every addition the concentration of these molecules changed and was calculated using the concentration of the aliquots, the total volume added, and the initial receiving solution volume of 100 μL .

Nernst plots were constructed using the relationship between the concentration of the added analyte and the potential measured at each step. The leveled out potential (within 1 mV) was obtained using the last 15 seconds of the time trace prior to a subsequent addition. The concentration was calculated using the the initial concentration of the addition solution, the total volume of addition solution added at each potential step, and the total volume of the initial receiving and addition solutions to account for the dilution factor for all previous additions.

The results for ascorbic acid, cysteine, and uric acid are shown in **Figures 5.4a, 5.4b, and 5.4c**, respectively. Each molecule was added to an intial receiving solution of 0.1 M PBS while the potential was measured using a mNPG (WE) and Ag/AgCl (RE) electrode. The logarithm of the change in concentration of each redox species was plotted versus the potential measured at each successive addition.

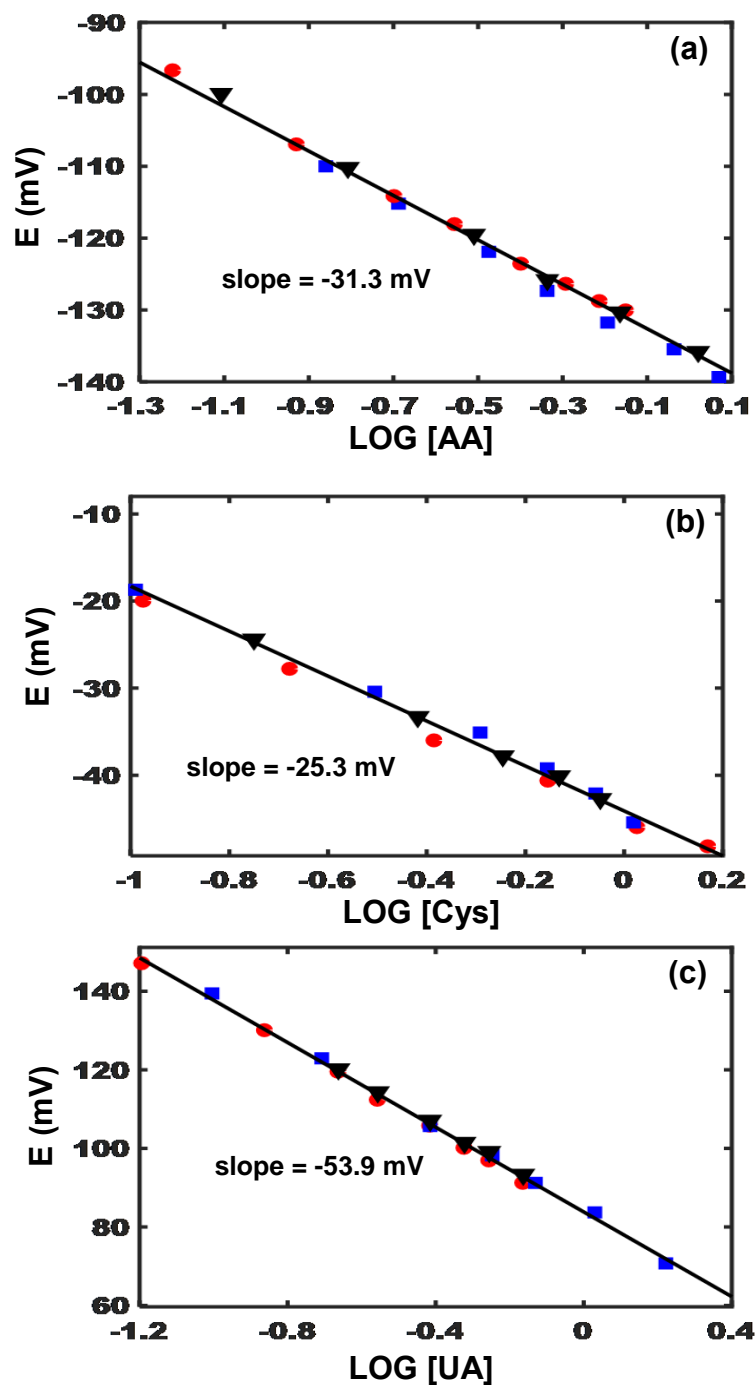


Figure 5.4. Nernst plots constructed using time trace and concentrations of (a) ascorbic acid, (b) cysteine, and (c) uric acid. The solid line represents a linear least squares regression analysis of three different data sets (represented as different symbols). The slope for each line is shown and all had correlation coefficients > 0.99 .

The slope of ascorbic acid was expected to show a two-electron transfer with a value of -

29.6 mV. The experimental slope of -31.3 ± 0.4 (N=3) was obtained showing a Nernstian response (**Fig. 5.4a**). The concentration range tested was 50 μ M to 2 mM. Ascorbic acid, at a pH of 7.4, will have already lost one proton leaving a negative charge on an oxygen molecule. The first electron transfer can occur forming a stable ascorbyl radical which allows for a second proton and electron transfer to dehydroascorbic acid, which is converted back to the radical and subsequently ascorbic acid. This transition occurs at such a small rate, that the concentration of the added ascorbic acid stays relatively the same with only an estimated conversion of less than 1 nanomolar (50,000 X smaller than lowest added concentration) of ascorbic to the redox pair dehydroascorbic acid.

The second biologically relevant redox molecule studied was cysteine and its results are shown in **Figure 5.4b**. Cysteine is an amino acid that is involved in the detoxification of free radicals in cells.²⁷ Due to its importance in healthy cell functioning the concentration of this in whole blood can be an indication of stress and disease.²⁸ The major distinguishing factor of cysteine versus other amino acids, is the presence of a thiol group (-SH). The oxidation of this group between two cysteine molecules forms a covalent sulfur-sulfur bond, called a disulfide bridge which contributes to the tertiary structure of proteins. As previously mentioned, thiol groups have been used to anchor molecules to the surface of Au electrodes. The presence of the thiol group in cysteine promotes the adsorption of cysteine onto an electrode surface.²⁹ The interaction of cysteine with the surface of the mNPG electrodes were elucidated using the potential measured after subsequent cysteine additions.

Cysteine was expected to have a similar two-electron/ two-proton transfer system similar to ascoric acid, with the exception that two cysteine molecules form a cystine molecule via a disulfide bridge. At a pH of 7.4, cysteine is in its zwitterion form where a positive charge is

localized on the amine group and a negative charge is localized on the carboxylic acid group. The thiol group remains protonated. The sulfur group then adsorbs to the electrode surface and the adsorbed species is converted to a radical adsorbed species following the loss of a proton and electron. The adsorbed species, under voltametric conditions, can be converted to cystine with the combining of two adsorbed species to form one disulfide molecule.³⁰ However, at rest potential, the concentration of cysteine will not change as an overpotential is not applied and cystine is not formed. The slope of cysteine was found to be -25.3 ± 0.8 mV (N=2) using a concentration range of 100 μ M to 1.5 mM. This agrees with the expected Nernstian slope of -29.6 for cysteine also being a two-electron transfer system (**Fig. 5.4b**).

The third biologically relevant redox molecules examined was uric acid, as it is important in metabolism and the onset of gout. In the presence of uric acid, a slope close to -29.6 mV was expected since uric acid is a two-electron transfer system as well. However, a slope of -53.9 ± 0.7 mV (N=3) was obtained for uric acid on mNPG electrodes (**Fig. 5.4c**). This suggests a one-electron transfer system based on the slope. It is possible that due to the passive nature of open-circuit potential (OCP), where the concentration of species in solution does not change by a detectable amount, that a more stable form of uric acid in the pH 7.4 solution, the urate ion, preferentially transfers one electron rather than two. Since no current is flowing and the molecules in solution come to an electrochemical equilibrium with the electrode, the stability of the redox species present at physiological pH of 7.4 plays a vital role. In voltammetry, the potential is changed in order to affect the flow of current by either oxidizing or reducing a species of interest. When subjected to an oxidizing overpotential, uric acid will lose two protons and two electrons forming the oxidized form of uric acid. This process usually occurs enzymatically in organisms, except for humans and non-human primates which do not have the ability to break

down uric acid. This enzymatic breakdown also occurs via a two proton/two electron transfer. Since there is no external force, such as an overpotential or enzyme present, the more stable urate ion comes to an equilibrium with the electrode with the minimal exchange of an electron to and from the surface.

As previously introduced above, a tell-tale sign of response in potentiometry is shown as a marked change in potential with each addition of a desired analyte. The potential will drop immediately follow the addition and will plateau over time. The plateau represents an equilibration between the solution and electrode as the solution becomes homogenous. Alternatively, a lack of a stair-step response suggests inactivity towards a molecule of interest or is a sign of very slow electron transfer kinetics, where equilibration of each step will occur in a time frame that is much larger than the desired test length. Since all three molecules (ascorbic acid, cysteine, and uric acid) showed a stair-step response in their OCP time-trace with each successive addition to the initial receiving solution, each could be evaluated and showed Nernstian responses towards the fabricated electrodes. These results supported the extension of potential measurements to other important biological redox molecules, such as glucose and hydrogen peroxide.

Given the large amount of attention that is being paid to combat diabetes, the mNPG electrodes were used to investigate the potentiometric response in the presence of glucose. Glucose sensing is the main method to determine a predisposition to diabetes or hypoglycemia.^{31,32} Cellular respiration is responsible for the production of high-energy molecules, adenosine triphosphate (ATP), where 28 ATP are formed per molecule of glucose.³³

The potential measured following a series of additions of glucose to an initial receiving solution is shown in **Figure 5.5a**. The figure shows a marked difference in the behavior of the time trace as compared to those for $[\text{Fe}(\text{CN})_6]^{4-}$ and $[\text{Fe}(\text{CN})_6]^{3-}$, AA, Cys, and UA (**Figs. 5.2a and 5.3a-c**). As described earlier, a stair step time trace is typically an indication of a good electrode response. In the presence of only electrolyte, even with additions of electrolyte solution, a stable time trace can take a long time ($>1 \text{ hr}$)² depending on the electrode and will resemble a half-life decay curve. Due to this lack of response another redox molecule of interest, H_2O_2 , was investigated instead.

The formation of radical oxygen species (ROS) occurs when the body is under stress. In an attempt to prevent these molecules from reacting with cellular materials, a series of antioxidant pathways are employed. Redox molecules like ascorbic acid and cysteine coupled with glutathione, act to reduce the ROS to H_2O_2 , which is then reduced to water in the cell by catalase (CAT) and extracellularly by glutathione peroxidase (GSHPx).²⁷ Unfortunately, the overproduction of H_2O_2 due to excessive stress can increase the concentration to a cytotoxic level ($\geq 50 \text{ } \mu\text{M}$).³⁴ The importance of physiological regulation of H_2O_2 has driven the

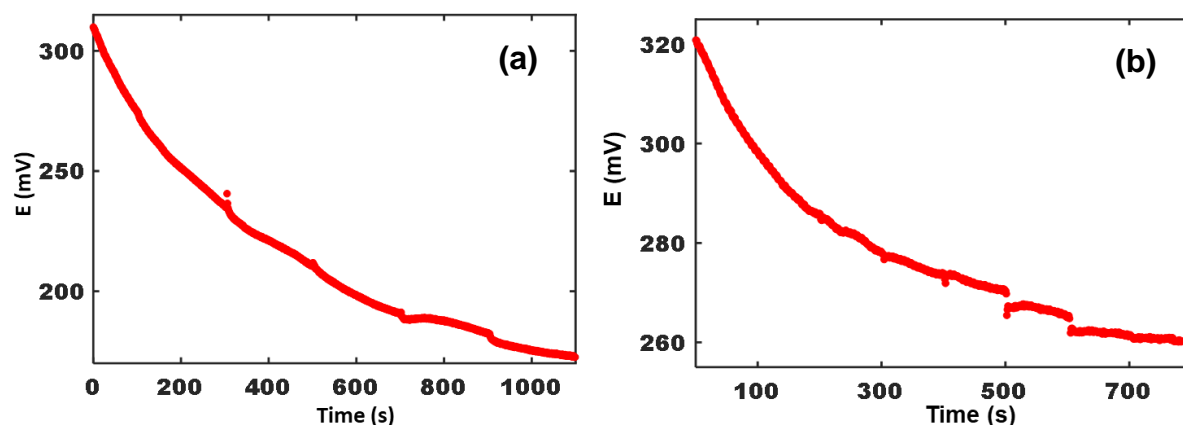


Figure 5.5. OCP time-traces showing little to no response to additions of (a) glucose and (b) hydrogen peroxide to 100 μL of 0.1 M PBS receiving solution. Breaks in the trace indicate the addition of the redox molecule of interest.

development of sensing methods.

Given the known reactivity of H_2O_2 in amperometric detection,³⁵ it was expected to behave in a Nernstian fashion like AA, Cys, and UA. To test this, H_2O_2 was added to 0.1 M PBS while the potential was measured. Interestingly, the same lack of response (**Fig. 5.5b**) was exhibited as shown for glucose. For both glucose and H_2O_2 , the large change in potential over the testing period can not be attributed simply to drift as the change due to simple electrode drift is insufficient. Rather than drift, very slow electron transfer kinetics on the mNPG surface is suggested.

Recent work described by Mandlar and coworkers³ detailed the an electrochemical sensor that used more than one electrode material to increase the response of the electrode in the presence of two redox molecules. A stainless steel electrode was used as a platform to study the impact additional materials have on the sensing of several redox molecules including 3-(3,4)-dihydroxyphenyl-L-alanine (l-dopa) and 3,4-dihydroxyphenylactic acid (dopac). Stainless steel was used as a control electrode and three additional electrodes were fabricated. The first was fabricated through the reduction of a platinum salt (PtCl_4) with ascorbic acid producing dispersed platinum (Pt) nanoparticles (NPs). The second was comprised of gold (Au) NPs electrodeposited onto the substrate surface using chloroauric acid in a buffered solution. Finally, a combination of these methods was used to fabricate a dual metal NP electrode beginning with Pt NPs deposition followed by Au NP electrodeposition.³ It was found that the Au NP electrode had a limited response to l-dopa. Pt NPs, however, showed fast electron transfer kinetics and a Nernstian response using potentiometric measurements. The Au-Pt NP electrode also showed a Nernstian response showing an improvement in sensing ability of Au with Pt. Also, the incremental increase of deposition time of Pt NPs to the stainless steel electrode displayed an enhancement to

Nerstian behavior in the presence of dopac, where no such behavior was seen on bare stainless steel.

In the present work, we explored the approach of adding platinum nanoparticles into the NPG framework of mNPG electrodes in order to increase the kinetics of electron transfer of glucose and H_2O_2 at NPG. Platinum was chosen because it is well known that the electron transfer kinetics of glucose and hydrogen peroxide are faster on platinum compared to gold.^{35–37}

5.3.2. Incorporation of Platinum into mNPG Electrodes

An amperometric method was used to speckle the surface of the nanostructured mNPG layer. The mNPG electrode was submerged in a 0.75 mM solution of K_2PtCl_4 in 0.5 M H_2SO_4 . A Ag/AgCl reference electrode and platinum wire auxiliary electrode were placed in the solution and a potential of -0.2 V was held for a period of 2 seconds. The fabricated platinum-speckled mini-nanoporous gold (mNPG-Pt) electrodes were rinsed with DI and dried with a stream of nitrogen.

Scanning electron microscopy (SEM) is a characterization technique used to provide topographical surface information and was used to characterize the surface of mNPG and mNPG-Pt electrodes. **Figure 5.6** shows the SEM images of the nanostructure of the NPG of both mNPG (A-C) and mNPG-Pt (D-F). As can be seen, the nanostructure of the NPG consists of a 3-dimensional network of interconnected pores and ligaments. Pore sizes range from 5 to 20 nm with ligaments between 10 and 100 nm, characteristic of previously described dealloyed NPG.^{9,10} Upon comparison of **Figures 5.6 A-C** with **D-F**, it can be seen that the addition of Pt does not change the nanostructure of NPG. It is not possible to see Pt nanoparticles in the NPG framework because of the similar atomic mass of Au and Pt, which would show a similar grayscale in SEM images, as well as the very small deposition of Pt onto the NPG surface

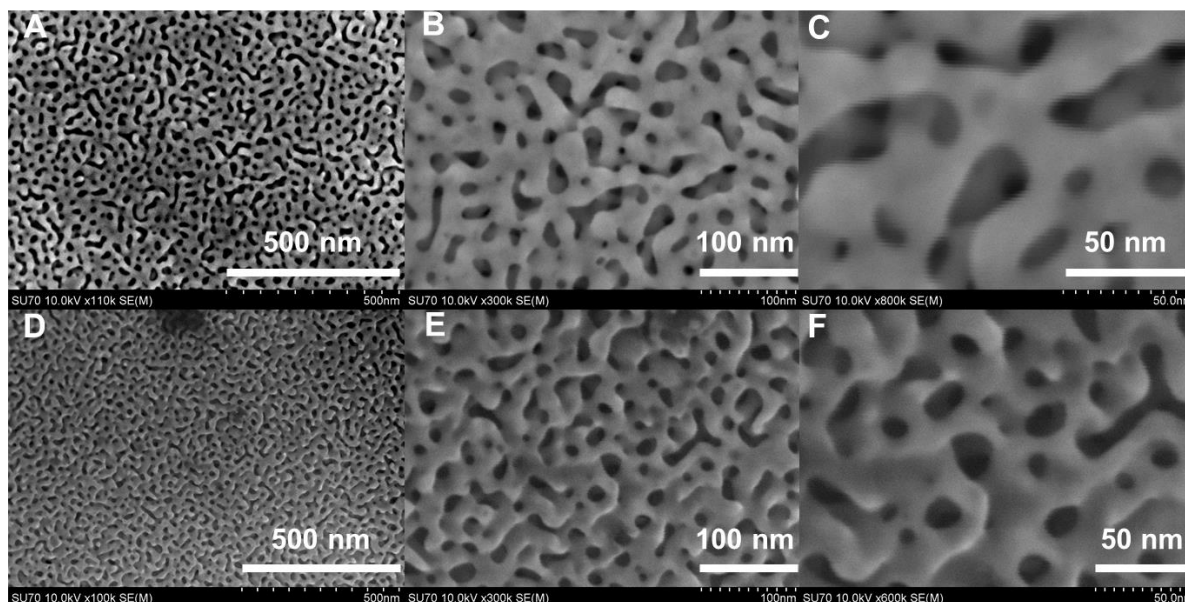


Figure 5.6. SEM images of (A-C) mNPG and (D-F) mNPG-Pt surfaces at increasing magnifications. Pores range from 5 to 20 nm.

preventing the differentiation of particles. Additionally, the presence of platinum could not be conclusively confirmed using Energy Dispersive X-ray Spectroscopy (EDS) as this method cannot adequately distinguish Pt from Au since the two peaks overlap (a platinum peak at 2.048 keV and a gold peak present at 2.120 keV).

In order to confirm the presence of platinum in the nanoporous structure of the electrodes following deposition, cyclic voltammetry was used. Gold has characteristic peaks in the presence of H_2SO_4 , where a peak is shown during the anodic sweep, which represents the formation of gold oxide on the surface. Once the potential is reversed, the anodically formed gold oxide is reduced to gold showing a large cathodic reduction peak. Platinum is known to adsorb hydrogen by forming a layer on the platinum surface. The adsorption occurs during the anodic sweep and the desorption is shown as a cathodic peak near 0 V or lower.³⁸ To calculate the electroactive surface area (EASA) the gold cathodic peak (Coulombs) which represents the charge passed over the electrode during reduction was converted to surface area of gold (cm^2) using the standard

charge per unit area of bulk crystalline gold ($390 \mu\text{C}/\text{cm}^2$).³⁹ A similar calculation was performed using the charged passed over the electrode during desorption of hydrogen and converted using the charge per unit area of platinum ($210 \mu\text{C}/\text{cm}^2$).⁴⁰

A potential window of -0.4 to 1.4 V with a 100 mV/s scan rate (Ag/AgCl reference and Pt wire auxiliary electrodes) was used to obtain voltammograms of mNPG and Pt-speckled mNPG (mNPG-Pt) electrodes in 0.5 M H_2SO_4 (**Fig. 5.7**) before (dashed -) and after (solid -) platinum deposition. The characteristic hydrogen desorption peak at -0.1 V indicative of platinum being present, was only shown on the mNPG-Pt electrodes and not the mNPG which was expected. Given the framework of both electrodes are NPG, the characteristic gold anodic

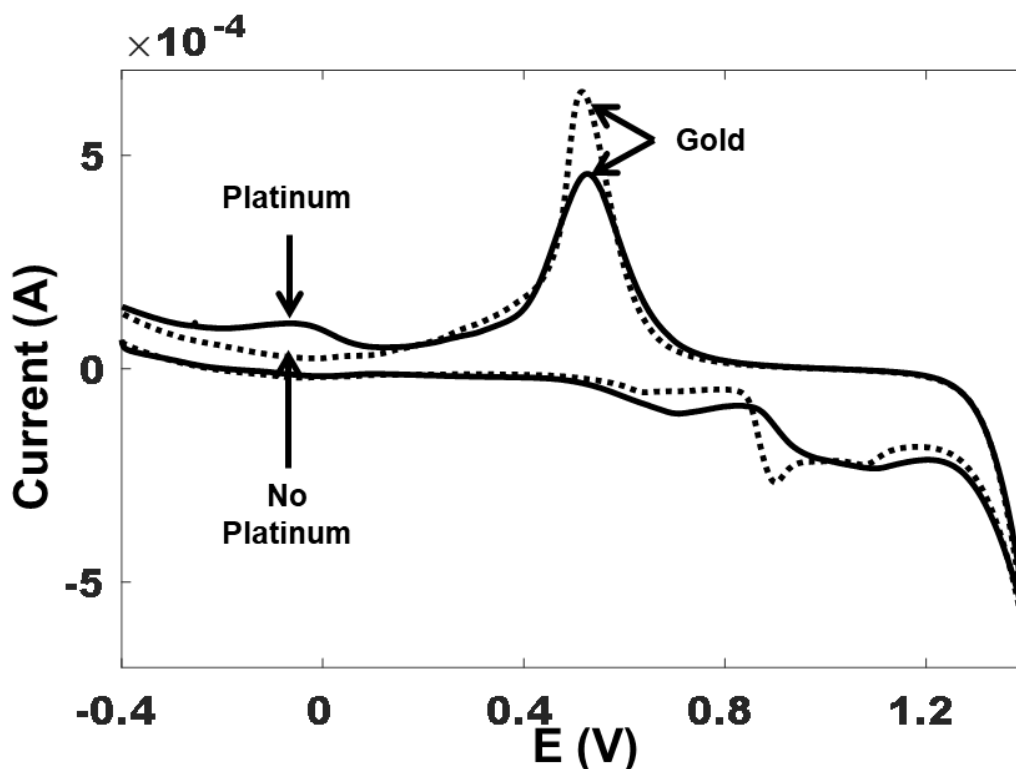


Figure 5.7. Cyclic voltammograms of a NPG electrode before (dashed -) and after (solid -) platinum deposition using a potential window of -0.4 to 1.4 V, in 0.5 M H_2SO_4 at a scan rate 100 mV/s. The gold oxide reduction peak at 0.5 V decreases and the hydrogen desorption peak of platinum at -0.1 V appears following deposition.

oxidation peak at 1.4 V and corresponding cathodic reduction peak at 0.5 V were seen in both mNPG and mNPG-Pt electrodes. When comparing mNPG electrodes whose surface area was speckled with platinum, the characteristic cathodic gold reduction peak at around 0.5 V was seen to decrease following Pt deposition. This makes sense, as the platinum would decrease the surface area of exposed gold sites. Additionally, the oxidation of platinum was seen as a small peak at 0.7 V, which was not seen in the mNPG sample. The prominence of the gold oxidation peaks were decreased in the mNPG-Pt electrodes when compared to mNPG electrodes.

In order to obtain compositional data of the mNPG-Pt to elucidate platinum loading, X-ray photoelectron spectroscopy (XPS) was employed. XPS allows for the determination of sample atomic percent from the top surface (2-10 nm). The sample surface is bombarded with an X-ray beam that transfers kinetic energy to sample atoms which are ejected. The kinetic energy of the ejected atoms is used in conjunction with the incident beam energy to calculate binding energy (E_{binding}). Samples of nanoporous gold and platinum speckled nanoporous gold were characterized using this technique.

Analysis was completed using Advantage software (ThermoFisher). All binding energy values for Au, Ag, and Pt were first normalized using the C1s peak. The background was subtracted using the Smart background feature, which models a Shirley type background with the added parameter that the background should not be of greater intensity than the data throughout the spectrum. A Shirley background uses an algorithm continuously determining the background

$$S(E) = I_2 + \kappa \frac{A_2(E)}{A_1(E) + A_2(E)} \quad (5.2)$$

defined by the two areas of a doublet pair (A_1 and A_2) (Eq. 5.2).⁴¹ The background is calculated using these areas (A_1 and A_2), the start point intensity (I_1), the end point intensity (I_2), the difference between I_1 and I_2 (κ), and the binding energy at each point in the defined range.

Following background determination, the peaks are fitted using a mixture of Gaussian and Lorentzian peak models. The software sets the initial mixture of 30 % Lorentzian to Gaussian, however if the peaks were not fit sufficiently, the peaks were manually adjusted to reduce incorrect area measurement. The peak areas were then used to calculate the percent composition of each element using Wagner relative sensitivity factors (Au 4f 4.95, Ag 3d 5.2, and Pt 4f 4.4) for each doublet pair. The calculated areas of the combined doublet pairs were used to obtain percent composition. The peak area of each element is divided by its respective RSF and this value is divided by the sum of all element peak areas that divided by their respective RSFs.

Figure 5.8 shows a comparison of NPG (**red**) to that of NPG-Pt (**blue**). The presence of gold is expected in both samples due to the previously described dealloying of 12 K gold leaf to prepare NPG along with residual silver. Comparing electrodes before (NPG) and after platinum deposition (NPG-Pt) shows 5/2 and 7/2 4f Au peaks with binding energies of 87.3 / 83.6 eV as well as 87.9 / 84.2 eV, respectively (**Fig. 5.8 a, d**). The 7/2 4f values agrees very close to the literature of metallic gold of 84.0 eV for both electrodes.⁴² In addition, the expected spin-orbit component separation of 3.7 eV was calculated. Residual Ag was also present and represented as 3/2 and 5/2 3d peaks with binding energies of 373.9 / 367.9 eV for NPG and 374.2 / 368.2 eV for NPG-Pt(**Fig. 5.8 b, e**). Again, these values suggest metallic silver which has a 3d 5/2 binding energy of 368.2 and the separated spin-orbit components matched the expected value of 6.0 eV.⁴² The incorporation of platinum was seen in the appearance of platinum 5/2 and 7/2 4f peaks at 74.7 / 71.5 eV for NPG-Pt electrodes (**Fig. 5.8 f**) confirming metallic platinum (4f 7/2 binding energy of 71.0).⁴² The spin-orbit separation was close to the expected value of 3.35 eV with 3.2 eV calculated. No platinum was seen on the NPG electrodes prior to deposition (**Fig. 5.8 c**). The areas of each peak pair for Au, Ag, and Pt, were used to calculate material composition using the

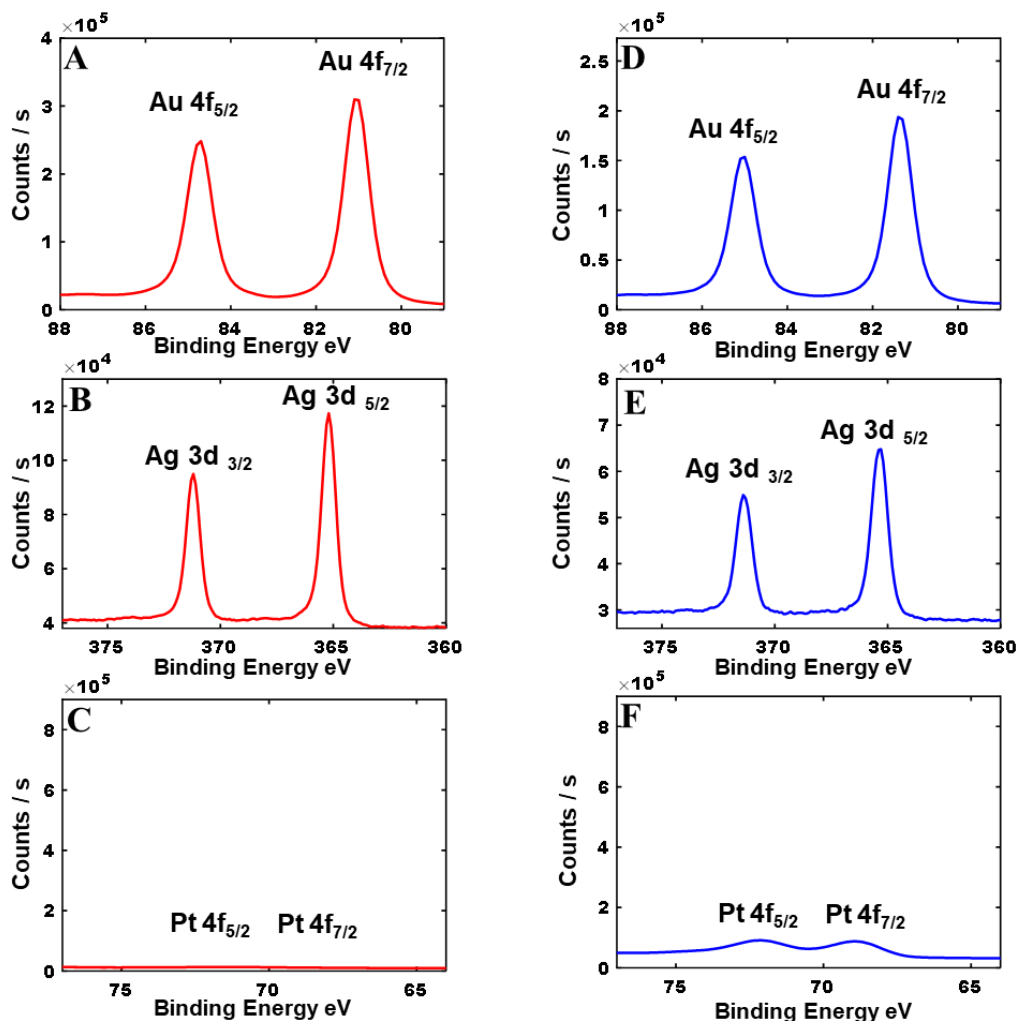


Figure 5.8. XPS spectra of NPG without platinum deposition showing (a) Au 4f 5/2 and 7/2 peaks at 87.3 and 83.6 eV, respectively, (b) Ag 3d 3/2 and 5/2 at 373.9 and 367.9 eV, respectively, and (c) lack of Pt 4f 5/2 and 7/2 peaks. Following the deposition of platinum into the NPG framework (d) Au 4f 5/2 and 7/2 peaks at 87.9 and 84.2 eV, respectively, (e) Ag 3d 3/2 and 5/2 at 374.2 and 368.2 eV, respectively, and (f) presence of Pt 4f 5/2 and 7/2 peaks at 74.7 and 71.5 eV, respectively. Raw data shown. Binding energies were normalized using obtained C1s peak (not shown). Composition of NPG and NPG-Pt were calculated as Au_{0.839}, Ag_{0.161}, Pt_{0.0} and Au_{0.793}, Ag_{0.164}, Pt_{0.043}, respectively.

standard relative sensitivity factor (RSF) for doublet pairs. Relative sensitivity factors for Au, Ag, and Pt were used to scale the doublet peaks to calculate each metal's contribution to the sample structure. Compositions of Au_{0.839} and Au_{0.793}, Ag_{0.161} and Ag_{0.164}, and Pt_{0.0} and Pt_{0.043} for NPG and NPG-Pt samples, respectively, were obtained. There is a normal variation in Ag content seen in the dealloying process.⁴³ The electrochemical deposition of platinum will occur

on the surface of the NPG due to available high energy sites of the kinks and turns seen in the ligaments and pores of the 3D-structure.⁴⁴

5.3.3. Comparison of mNPG to mNPG-Pt Electrodes and Investigation of Response Enhancement

After deposition of platinum into mNPG, the mNPG-Pt electrode response in the presence of ferri-ferrocyanide was first established. As described above, the change in potential with time following the addition of concentrated aliquots of ferrocyanide (0.1 M PBS) to a solution containing 100 μ L of 5 mM ferricyanide (0.1 M PBS). **Figure 5.9a** shows the OCP time trace and **Figure 5.10a** shows the corresponding Nernst plot. The slope of ferri-ferrocyanide on mNPG-Pt electrodes was found as -56.9 ± 0.7 mV with a y-intercept of 147.4 ± 0.4 mV (N=3), which is very close to the expected Nernstian slope of -59.2 as well as to the slope of mNPG electrodes. Again, for a poised system the y-intercept represents the standard reduction potential of the redox couple. In this case, it agrees with the theoretical value of 142 mV.²⁶

Once the platinum incorporated electrodes were validated using ferri-ferrocyanide (**Fig. 5.9a**), a comparison to mNPG electrodes in the presence of the previously mentioned redox molecules (AA, Cys, and UA) was completed. The time-traces for ascorbic acid, cysteine, and uric acid (**Figs 5.9b-d**, respectively) all showed a stair-step response to additions of molecule aliquots to 100 μ L initial receiving solution of 0.1 M PBS and were used, along with their concentration, to construct corresponding Nernst plots. The response of ascorbic acid was also similar to mNPG on mNPG-Pt at -32.1 ± 0.7 (N=3) (**Fig. 5.10b**). Cysteine, with a slope of -29.1 ± 0.6 mV (N=3) on mNPG-Pt(**Fig. 5.10c**), was similar to mNPG electrodes in which both

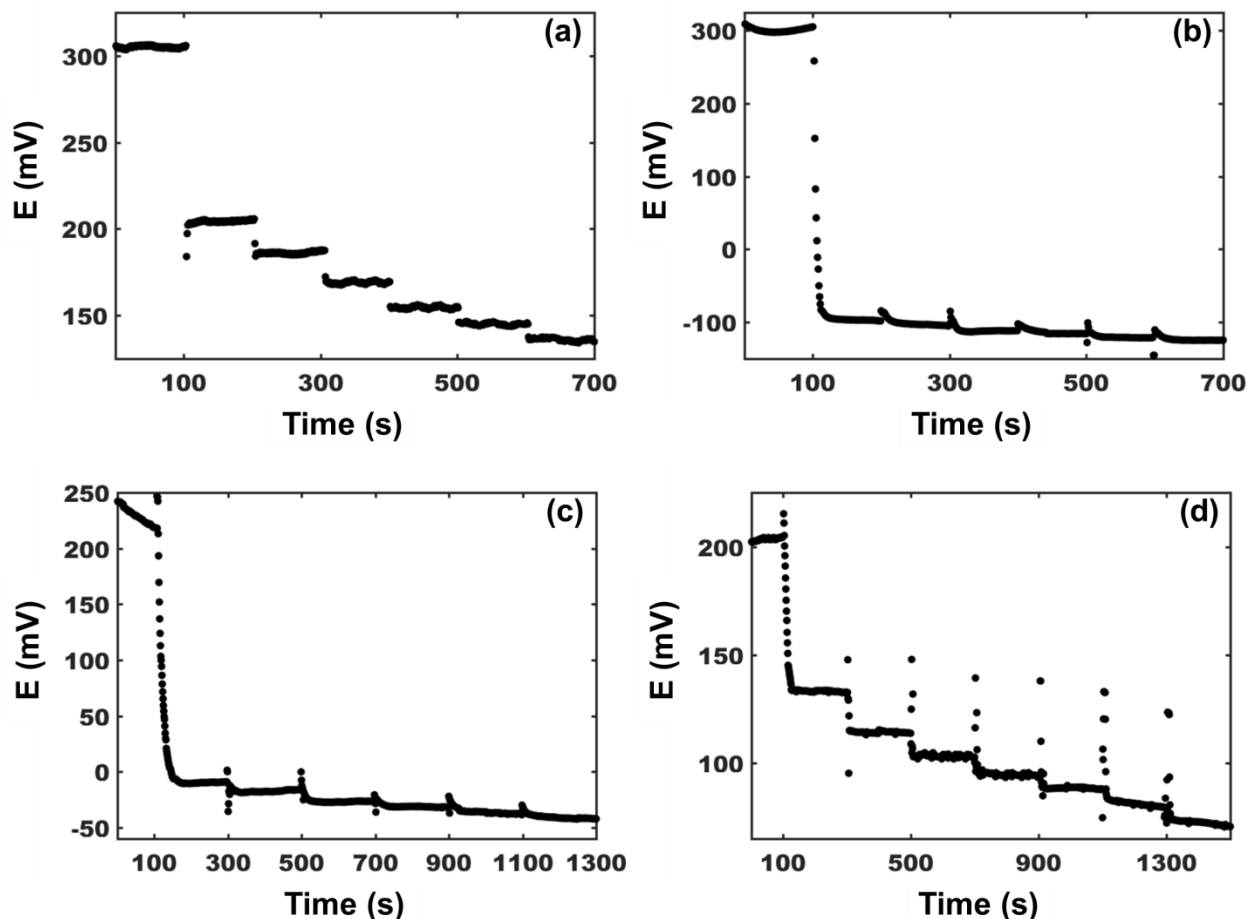


Figure 5.9. Open-circuit potential (OCP) time traces for the addition of aliquots of (a) ferrocyanide every 100 seconds to a receiving solution of ferricyanide in 0.1 M PBS as well as the time-traces for (b) ascorbic acid (AA) every 100 seconds, (c) cysteine (Cys) every 200 seconds, and (d) uric acid (UA) every 200 seconds, respectively, to a 100 μ L solution of 0.1 M PBS (0.1 M KCl as electrolyte, pH = 7.4) following an initial wait time of 100 seconds. Potential was measured using a Pt-speckled mini-nanoporous gold (mNPG-Pt) electrode as the working electrode and Ag/AgCl as the reference electrode.

were Nerstian. The last comparison was of uric acid on both mNPG and mNPG-Pt electrodes with a comparable slope of -53.4 ± 0.9 mV (N=3) (**Fig. 5.10d**) following platinum incorporation, also showing a one-electron response even though uric acid is traditionally a two-electron system.

The incorporation of platinum was theorized to enhance the response of the mNPG electrodes to hydrogen peroxide and glucose. As compared with the time-trace in **Figure 5.5a**

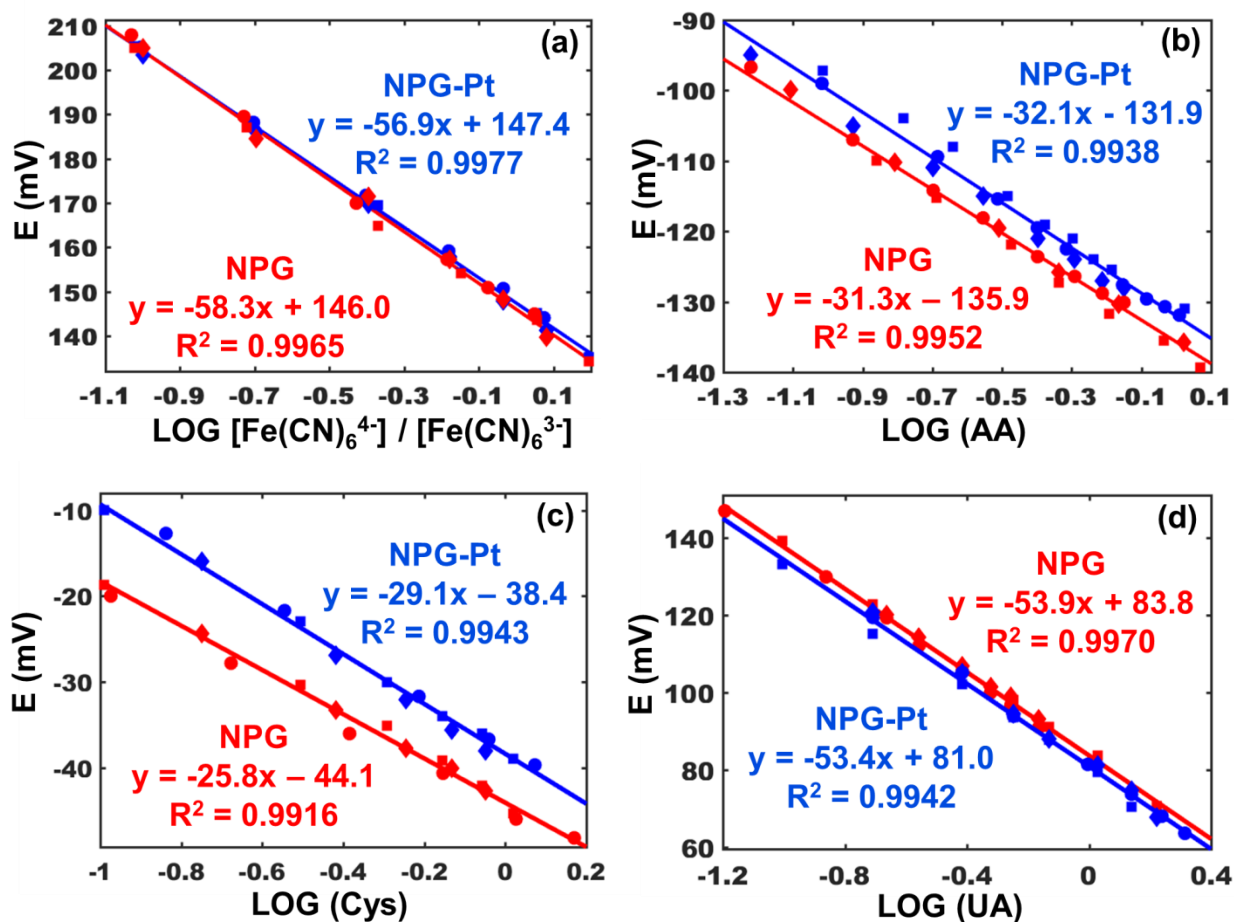


Figure 5.10. Nernst plots comparing the response of mNPG-Pt (blue) and mNPG (red) electrodes to the addition of (a) ferrocyanide to ferricyanide in 0.1 M PBS and the addition of (b) ascorbic acid, (c) cysteine, and (d) uric acid to 0.1 M PBS, respectively. All equations show the calculated slopes and y-intercepts of each plot with correlation coefficients all >0.99 . Different shapes of each color represent a separate set of data.

which lacked a defined stair-step with additions, **Figure 5.11a** shows a decreasing potential with every addition of glucose. The time-trace was used to construct a Nernst plot and displayed an expected slope close to -29.2 mV of -27.2 ± 0.7 mV ($N=2$) (**Fig. 5.12a**), indicative of a two-electron-transfer system with the addition of glucose to the receiving solution. A similar stair-step response was seen with the addition of hydrogen peroxide to a receiving solution (**Fig. 5.11b**) except that the potential increases with each addition, whereas every other system shows

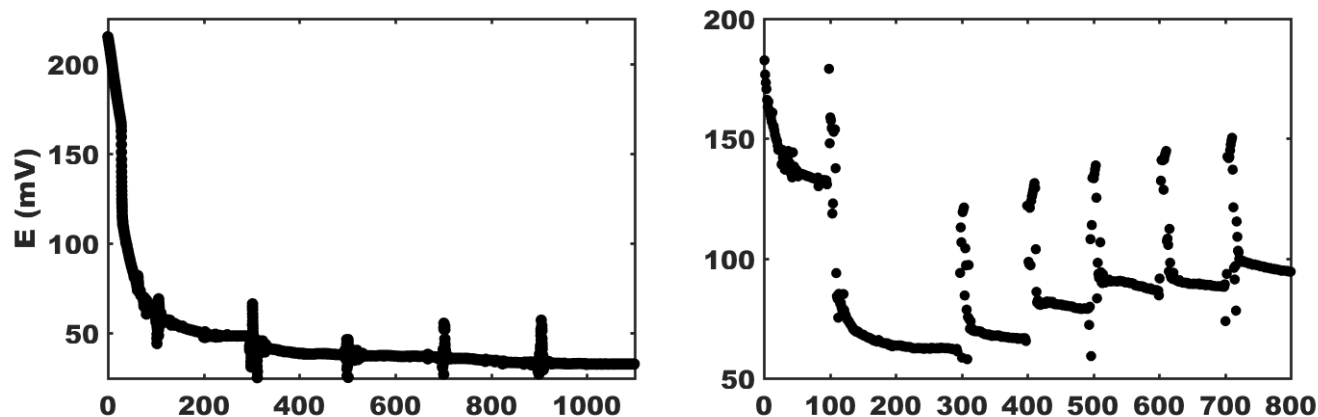


Figure 5.11. Open-circuit potential (OCP) time-traces showing a characteristic stair-step with additions of (a) glucose every 200 seconds (after an initial wait time of 100 seconds) or (b) hydrogen peroxide (after a 100 second initial wait time) with difference in time between the first and second addition was 200 seconds and subsequent addition was every 100 seconds to separate 100 μ L initial receiving solutions of 0.1 M PBS (0.1 M KCl as electrolyte pH = 7.4).

a decrease in potential. This is due to fact that H_2O_2 is the oxidized species and ferrocyanide, AA, Cys, UA, and glucose are all the reduced species in their respective redox equations. This behavior is similar to that of unpoised ferricyanide when aliquots were added to a receiving solution of 0.1 M KCl.¹⁰ A Nernst plot was constructed and showed a slope of -32.0 ± 0.5 mV

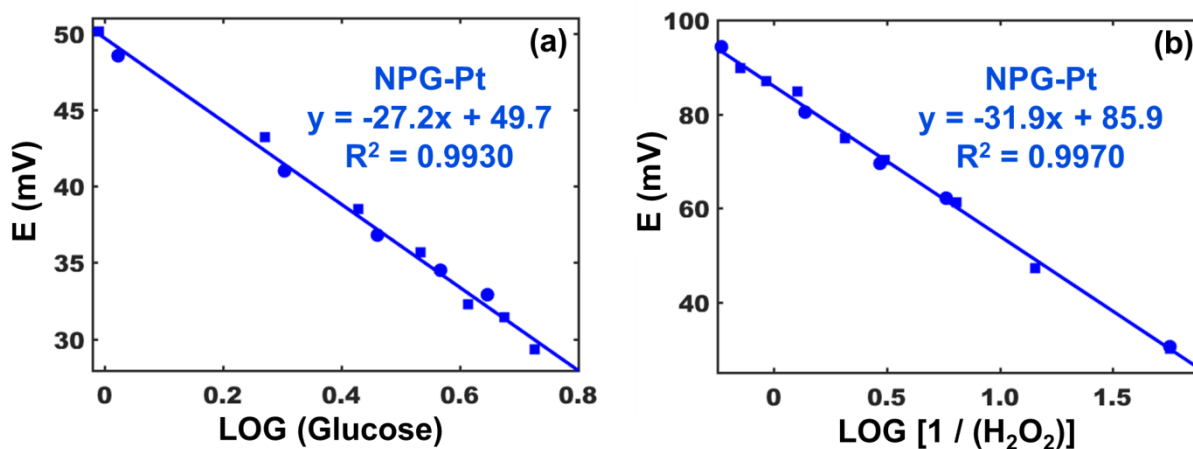


Figure 5.12. Nernst plots showing the response of mNPG-Pt electrodes to the addition of (a) glucose and (b) hydrogen peroxide. The solid line represents a linear least squares regression analysis of different data sets (represented as different symbols). The slope for each line is shown and all had correlation coefficients > 0.99 .

(N=2) in the concentration range of 10 μM to 1.7 mM (**Fig. 5.12b**). These measurements show that the response of the NPG electrodes was enhanced to the presence of glucose and hydrogen peroxide with the deposition of platinum into the porous framework.

5.3.4. Response of Cysteine in the Presence of Multiple Species at Physiological Concentrations

The contribution of redox species in complex solutions, such as blood or food products, can make potentiometric measurements difficult as each species comes to equilibrium at the electrode surface after coming to an equilibrium with each other. Given biological systems rarely have only a single redox species present, it was necessary to initially investigate the response of changing the concentration of a redox species, cysteine, in the presence of other redox species, ascorbic and uric acid. Cysteine was added to a solution of 50 μM ascorbic acid and 300 μM uric acid in 0.1 M PBS while the potential was measured. These concentrations were chosen because

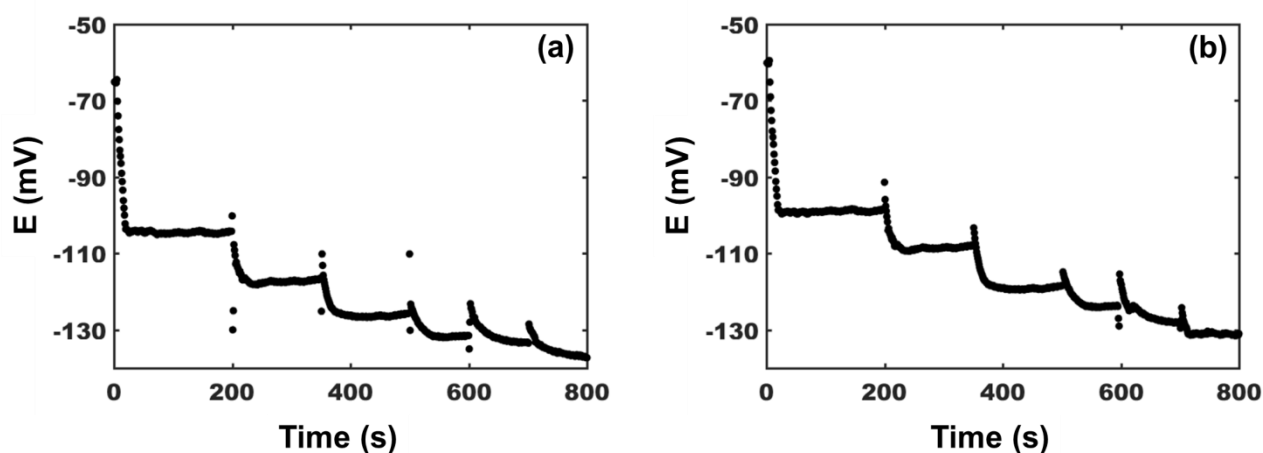


Figure 5.13. Open-circuit potential (OCP) time traces for the addition of aliquots of cysteine (Cys) in 0.1 PBS solution containing 50 μM AA and 300 μM UA to an initial receiving solution of 0.1 M PBS also containing 50 μM AA and 300 μM UA. The time-traces were obtained simultaneously using (a) mNPG and (b) mNPG-Pt electrodes. The first addition of cysteine occurred at ~5 seconds causing a large drop in initial potential.

the physiological concentrations of AA and UA in whole blood are 50 μM and 300 μM , respectively. An initial receiving solution of 50 μM AA and 300 μM UA were prepared in 0.1 M PBS. The addition of concentrated aliquots of Cys, prepared in a separate solution of 50 μM AA and 300 μM UA were prepared in 0.1 M PBS were added to ensure a constant concentration of AA and UA while the concentration of Cys was increased with each addition. The OCP time-trace (**Fig. 5.13**) and concentration of cysteine was used to construct a Nernst plot (**Fig. 5.14**) with a slopes of -33.5 ± 0.8 mV and -34.8 ± 0.9 mV for mNPG and mNPG-Pt electrodes, respectively. Both electrodes were tested simultaneously in the one solution of PBS with ascorbic and uric acids during additions of cysteine. The similar response to additions of cysteine in the presence of physiological ascorbic and uric acids can be seen through the difference in the

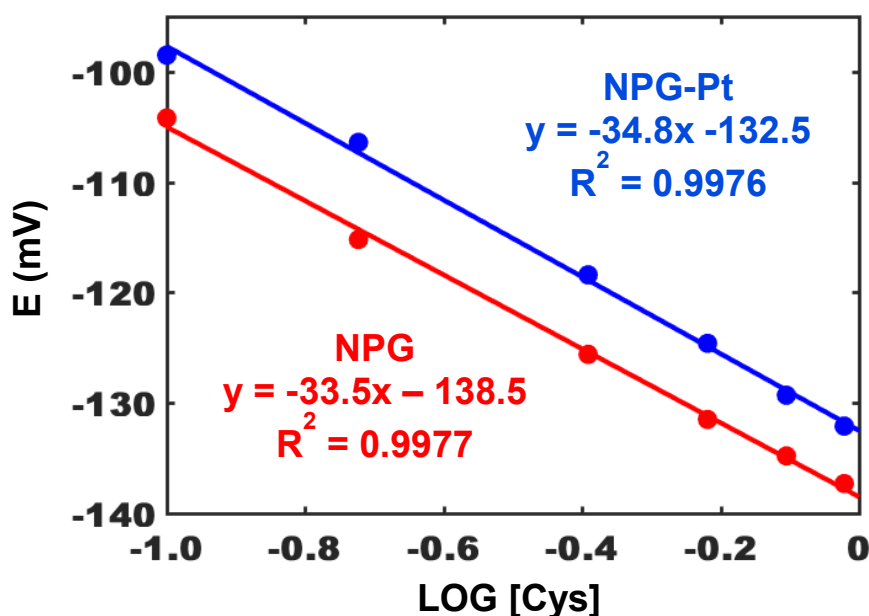


Figure 5.14. Nernst plot showing the response of mNPG-Pt (**blue**) and mNPG (**red**) electrodes to the addition of cysteine to 0.1 M PBS containing physiological concentrations of ascorbic acid (50 μM) and uric acid (300 μM). Potential measurements were obtained simultaneously.

initial potential after the first addition. A measured potential of around -60 mV was obtained during the first 5 seconds which was attributed to the presence of AA and UA in PBS (**Fig.5.13**). The potential stabilized at a negative potential of around -100 mV after the first addition of cysteine in the presence of additional redox species (AA and UA), whereas the potential was measured around 80 mV more positive with only cysteine being present in buffer solution after the first addition (**Fig. 5.3b and Fig. 5.9c** for mNPG and mNPG-Pt electrodes, respectively). This illustrates the cumulative effect of multiple redox species in solution on establishing the open-circuit potential.

5.4. Conclusion

The performance of capillary nanoporous gold (mNPG) electrodes was investigated following validation with a known electrode calibrant, the ferri-ferrocyanide redox couple. The response of several biologically relevant redox molecules was measured and showed a Nernstian response in the presence of ascorbic acid, cysteine, and uric acid. However, when exposed to glucose and hydrogen peroxide the electrodes responded with such slow electron transfer kinetics as to exceed the desirable experiment time of less than 20 minutes. In order to enhance the response of these electrodes, a minimal amount of platinum (~4%) was incorporated into the porous structure of the electrodes. Nernstian behavior was seen when the electrodes were in the presence of both glucose and hydrogen peroxide, respectively, showing the increased response of electrodes to additional redox molecules while keeping costs down. Additionally, using a very small solution volume of 100 μ L bodes well in future testing where only small sample volumes are available.

5.5. References

1. Bard, A. J. & Faulkner, L. R. *Electrochemical Methods: Fundamentals and Applications*. (John Wiley and Sons, Inc., 1980).
2. Percival, S. J. & Bard, A. J. Ultra-Sensitive Potentiometric Measurements of Dilute Redox Molecule Solutions and Determination of Sensitivity Factors at Platinum Ultramicroelectrodes. *Anal. Chem.* **89**, 9843–9849 (2017).
3. Noyhouzer, T., Valdinger, I. & Mandler, D. Enhanced potentiometry by metallic nanoparticles. *Anal. Chem.* **85**, 8347–8353 (2013).
4. Fiedler, S., Vepraskas, M. J. & Richardson, J. L. *Soil Redox Potential: Importance, Field Measurements, and Observations. Advances in Agronomy* **94**, (Elsevier Masson SAS, 2007).
5. Goncharuk, V. V., Bagrii, V. A., Mel'nik, L. A., Chebotareva, R. D. & Bashtan, S. Y. The use of redox potential in water treatment processes. *J. Water Chem. Technol.* **32**, 1–9 (2010).
6. Tessutti, L. S., Macedo, D. V., Kubota, L. T. & Alves, A. A. Measuring the antioxidant capacity of blood plasma using potentiometry. *Anal. Biochem.* **441**, 109–114 (2013).
7. Romero, M. R., Ahumada, F., Garay, F. & Baruzzi, A. M. Amperometric biosensor for direct blood lactate detection. *Anal. Chem.* **82**, 5568–5572 (2010).
8. Patel, J., Radhakrishnan, L., Zhao, B., Uppalapati, B., Daniels, R. C., Ward, K. R. & Collinson, M. M. Electrochemical properties of nanostructured porous gold electrodes in biofouling solutions. *Anal. Chem.* **85**, 11610–11618 (2013).
9. Farghaly, A. a., Lam, M., Freeman, C. J., Uppalapati, B. & Collinson, M. M. Potentiometric Measurements in Biofouling Solutions: Comparison of Nanoporous Gold to Planar Gold. *J. Electrochem. Soc.* **163**, H3083–H3087 (2016).
10. Freeman, C. J., Farghaly, A. A., Choudhary, H., Chavis, A. E., Brady, K. T., Reiner, J. E. & Collinson, M. M. Microdroplet-Based Potentiometric Redox Measurements on Gold Nanoporous Electrodes. *Anal. Chem.* **88**, 3768–3774 (2016).
11. Ciesielski, P. N., Scott, A. M., Faulkner, C. J., Berron, B. J., Cliffel, D. E. & Jennings, G. K. Functionalized Nanoporous Gold Leaf Photosystem I. *ACS Nano* **2**, 2465–2472 (2008).
12. Rudnev, A. V., Yoshida, K. & Wandlowski, T. Electrochemical characterization of self-assembled ferrocene-terminated alkanethiol monolayers on low-index gold single crystal electrodes. *Electrochim. Acta* **87**, 770–778 (2013).
13. Rudnev, A. V., Zhumaev, U., Utsunomiya, T., Fan, C., Yokota, Y., Fukui, K. I. & Wandlowski, T. Ferrocene-terminated alkanethiol self-assembled monolayers: An electrochemical and in situ surface-enhanced infra-red absorption spectroscopy study. *Electrochim. Acta* **107**, 33–44 (2013).
14. Laforgue, A., Addou, T. & Bélanger, D. Characterization of the deposition of organic molecules at the surface of gold by the electrochemical reduction of aryldiazonium cations. *Langmuir* **21**, 6855–6865 (2005).
15. Collinson, M. M. Nanoporous Gold Electrodes and Their Applications in Analytical Chemistry. *ISRN Anal. Chem.* **2013**, 1–21 (2013).
16. Kumar, S. & Zou, S. Electrooxidation of Carbon Monoxide and Methanol on Platinum-Overlayer-Coated Gold Nanoparticles: Effects of Film Thickness. *Langmuir* **23**, 7365–7371 (2007).
17. Tian, N., Zhou, Z. Y. & Sun, S. G. Platinum metal catalysts of high-index surfaces: from

- single-crystal planes to electrochemically shape-controlled nanoparticles. *J. Phys. Chem. C* **112**, 19801–19817 (2008).
18. Chhetri, M., Rana, M., Loukya, B., Patil, P. K., Datta, R. & Gautam, U. K. Mechanochemical Synthesis of Free-Standing Platinum Nanosheets and Their Electrocatalytic Properties. *Adv. Mater.* **27**, 4430–4437 (2015).
 19. Bartlett, P. N., Baumberg, J. J., Birkin, P. R., Ghanem, M. a. & Netti, M. C. Highly ordered macroporous gold and platinum films formed by electrochemical deposition through templates assembled from submicron diameter monodisperse polystyrene spheres. *Chem. Mater.* **14**, 2199–2208 (2002).
 20. Ge, X., Wang, R., Liu, P. & Ding, Y. Platinum-decorated nanoporous gold leaf for methanol electrooxidation. *Chem. Mater.* **19**, 5827–5829 (2007).
 21. Jia, J., Cao, L. & Wang, Z. Platinum-Coated Gold Nanoporous Film Surface : Electrodeposition and Enhanced Electrocatalytic Activity for Methanol Oxidation Platinum-Coated Gold Nanoporous Film Surface : Electrodeposition and Enhanced Electrocatalytic Activity for Methanol Oxidation. 8097–8101 (2008). doi:10.1021/la800163f
 22. Banerjee, I., Kumaran, V. & Santhanam, V. Synthesis and characterization of Au@Pt nanoparticles with ultrathin platinum overlayers. *J. Phys. Chem. C* **119**, 5982–5987 (2015).
 23. Han, C., Percival, S. J. & Zhang, B. Electrochemical Characterization of Ultrathin Cross-Linked Metal Nanoparticle Films. *Langmuir* **32**, 8783–8792 (2016).
 24. Yamauchi, Y., Tonegawa, A., Komatsu, M., Wang, H., Wang, L., Nemoto, Y., Suzuki, N. & Kuroda, K. Electrochemical Synthesis of Mesoporous Pt – Au Binary Alloys with Tunable Compositions for Enhancement of Electrochemical Performance. (2012).
 25. Xu, C., Wang, R., Chen, M., Zhang, Y. & Ding, Y. Dealloying to nanoporous Au/Pt alloys and their structure sensitive electrocatalytic properties. *Phys. Chem. Chem. Phys.* **12**, 239–246 (2010).
 26. Teasdale, P. R., Minett, A. I., Dixon, K., Lewis, T. W. & Batley, G. E. Practical improvements for redox potential (E(H)) measurements and the application of a multiple-electrode redox probe (MERP) for characterising sediment in situ. *Anal. Chim. Acta* **367**, 201–213 (1998).
 27. Nimse, S. B. & Pal, D. Free radicals, natural antioxidants, and their reaction mechanisms. *RSC Adv.* **5**, 27986–28006 (2015).
 28. Grunwell, J. R., Gillespie, S. E., Ward, J. M., Fitzpatrick, A. M., Brown, L. A., Gauthier, T. W. & Hebbar, K. B. Comparison of Glutathione, Cysteine, and Their Redox Potentials in the Plasma of Critically Ill and Healthy Children. *Front. Pediatr.* **3**, 3–8 (2015).
 29. Hager, G. & Brolo, A. G. Adsorption/desorption behaviour of cysteine and cystine in neutral and basic media: Electrochemical evidence for differing thiol and disulfide adsorption to a Au(1 1 1) single crystal electrode. *J. Electroanal. Chem.* **550–551**, 291–301 (2003).
 30. Ralph, T. R., Hitchman, M. L., Millington, J. P. & Walsh, F. C. The electrochemistry of l-cystine and l-cysteine. Part 1: Thermodynamic and kinetic studies. *J. Electroanal. Chem.* **375**, 1–15 (1994).
 31. Park, S., Boo, H. & Chung, T. D. Electrochemical non-enzymatic glucose sensors. *Anal. Chim. Acta* **556**, 46–57 (2006).
 32. Parwaiz, M., Lunt, H., Florkowski, C. M., Logan, F. J., Irons, L., Perwick, C., Frampton,

- C. M. A. & Moore, M. P. Assessment of glucose meter performance at the antenatal diabetes clinic: Exploration of patient-related and pre-analytical factors. *Ann. Clin. Biochem.* **51**, 47–53 (2014).
33. Shinawi, T. F., Kimmel, D. W. & Cliffel, D. E. Multianalyte microphysiometry reveals changes in cellular bioenergetics upon exposure to fluorescent dyes. *Anal. Chem.* **85**, 11677–11680 (2013).
 34. Halliwell, B., Veronique, M. & Hua, L. Hydrogen peroxide in the human body. *FEBS Lett.* **486**, 14–17 (2000).
 35. Yan, Z., Zhao, J., Qin, L., Mu, F., Wang, P. & Feng, X. Non-enzymatic hydrogen peroxide sensor based on a gold electrode modified with granular cuprous oxide nanowires. *Microchim. Acta* **180**, 145–150 (2012).
 36. Wang, G., He, X., Wang, L., Gu, A., Huang, Y., Fang, B., Geng, B. & Zhang, X. Non-enzymatic electrochemical sensing of glucose. *Microchim. Acta* **180**, 161–186 (2013).
 37. Lee, Y. J., Park, D. J., Park, J. Y. & Kim, Y. Fabrication and optimization of a nanoporous platinum electrode and a non-enzymatic glucose micro-sensor on silicon. *Sensors* **8**, 6154–6164 (2008).
 38. Hoare, J. P. A Cyclic Voltammetric Study of the Gold-Oxygen System. *J. Electrochem. Soc.* **131**, 1808–1815 (1984).
 39. Siepenkoetter, T., Salaj-Kosla, U., Xiao, X., Belochapkin, S. & Magner, E. Nanoporous Gold Electrodes with Tuneable Pore Sizes for Bioelectrochemical Applications. *Electroanalysis* **28**, 2415–2423 (2016).
 40. Miller, T. S., Macpherson, J. V. & Unwin, P. R. Dual-electrode measurements in a meniscus microcapillary electrochemical cell using a high aspect ratio carbon fibre ultramicroelectrode. *J. Electroanal. Chem.* **729**, 80–86 (2014).
 41. Carney, T. Basic and Advanced Processing. *Thermo Fisher Scientific*.
 42. Thermo Scientific XPS: Knowledge Base. Available at: <https://xpssimplified.com/periodictable.php>. (Accessed: 10th May 2018)
 43. McCue, I., Benn, E., Gaskey, B. & Erlebacher, J. Dealloying and Dealloyed Materials. *Annu. Rev. Mater. Res.* **46**, 263–286 (2016).
 44. Krajčí, M., Kameoka, S. & Tsai, A. P. Understanding the catalytic activity of nanoporous gold: Role of twinning in fcc lattice. *J. Chem. Phys.* **147**, (2017).

Chapter 6

Electrocatalytic Applications of Platinum-Speckled Nanoporous Gold (NPG-Pt) Electrodes Fabricated on a Functionalized, Low-Cost Glass Substrate

6.1. Introduction

The current and progressively worsening concentration of greenhouse gases accumulating in the atmosphere have greatly increased the interest in alternative energy models over the last 10 years. Specifically, the reliance on fossil fuels and the impact the usage of these fuels have on the environment have pushed the need for materials that can efficiently catalyze the reaction of alternative fuels while keeping the cost of fabrication feasible for large-scale production. Direct fuel cells have long been considered to be an important potential power source as the energy obtained from the cell is devoid of greenhouse gas emissions, producing only water through a series of electrochemical reactions, and the cells provide an efficient and

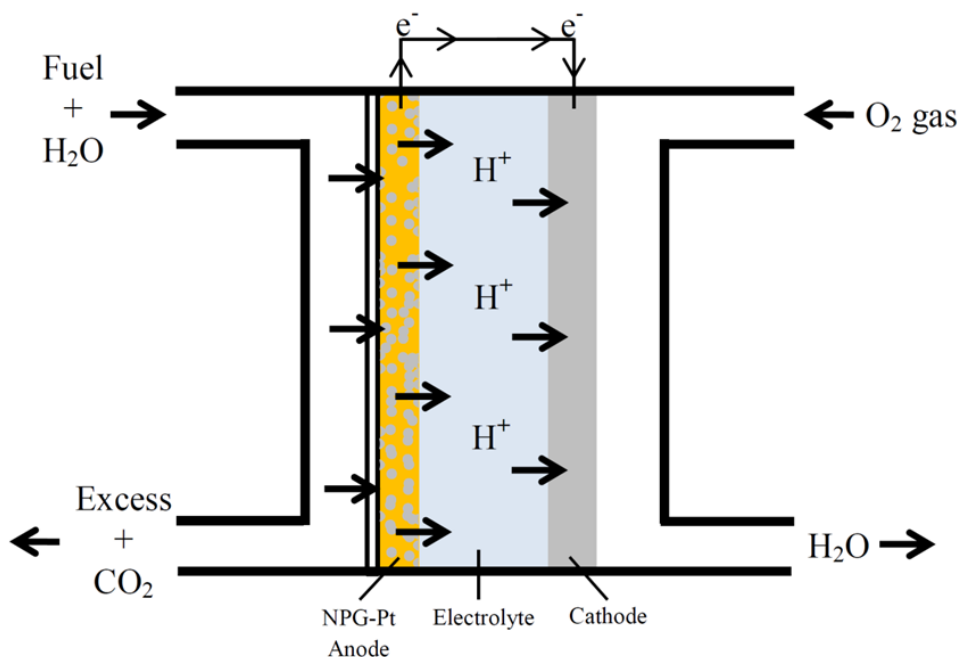


Figure 6.1. Illustrated representation of a fuel cell with a platinum-speckled nanoporous gold (NPG-Pt) anode, traditional platinum cathode, and acidic media as the electrolyte. Fuel is oxidized at the anode to form protons and electrodes, protons diffuse across the electrolyte to the cathode where, in the presence of oxygen, protons are reduced to water.

cell via very small and light tanks¹, thus this technology would provide a continuous output and significantly extended lifespan. There is a growing market for long lasting, durable, and

environmentally friendly sources of energy to power portable electronic devices and automobiles, with more attention being placed on developing more cost effective fuel cells.

A hydrogen fuel cell is characterized as a green energy source by converting chemical energy to direct current energy by utilizing hydrogen to reduce oxygen at the anode, creating water as a bi-product. Fuels cells using alcohols or acids as the oxidized species at the anode, produces protons (with carbon dioxide as a bi-product in methanol) that diffuse across the electrolyte layer where they are reduced in the presence of oxygen to produce water (**Fig. 6.1**). Direct Fuel cells utilize either acid or alkaline electrolytes (media).² Regardless, the electrolyte needs to have high ionic conductivity and cause no poisoning effects or detrimental side reactions.^{3,4} This process requires a catalyst to increase the conversion, platinum being the preferred and most effective material.⁵⁻⁷ Platinum is a good oxidation catalyst, able to withstand the acidic environment inside the cell, unreactive to bi-products, durable and stable.⁸⁻¹⁰ However, platinum is limited in availability, and this scarcity makes it an expensive material, making commercial applications of fuel cells utilizing platinum cost prohibitive. Alternative materials have been investigated to overcome the limitations of using platinum, including mixing with low cost palladium, and highly active rhodium or ruthenium.^{11,12} These alternatives also have downsides; palladium is sensitive to poisoning and is best managed in alkaline mediums, while rhodium is characterized by very high cost.¹³ This article aims to provide an alternative to the full coating of platinum and the current Pd, Rh and or Ru constructs.^{11,12}

The utilization of an open pore network structured nanoporous gold as electrode material has been used in electrodes to increase surface area, conductivity, diffusion, electron transport kinetics, and sensitivity in electrochemical testing.^{14,15} Gold has an endothermic oxygen chemisorption energy, does not bind oxygen and is inert towards oxidation reactions.¹⁶ The non-

uniform, random concave and convex curvatures present in nanoporous gold (NPG) structures have an intrinsic strain due to varied concentrations of high and low coordination gold particles.¹⁷ This strain enhances the electrochemical activity and reactivity of the metal surface and redox molecules. NPG has been used as an alternative to Pt, Pd, and Rh as a carbon monoxide (CO) oxidation catalyst.¹⁸ In the presence of molecular oxygen, CO is oxidized to CO₂ when interacting with the porous gold framework, whereas this reaction does not occur on bulk gold. A major downside is the need for increased reaction temperatures (> 60°C). The oxidation of select alcohols has shown promising results using NPG as an anode material for direct oxidation fuel cells. Methanol has shown an increase in oxidation capability when using a porous gold structure as compared to a bulk gold material.^{19,20} This catalyst does also require an increased reaction temperature to enhance the oxidation capability. Alternatively, the direct oxidation of formic acid has been reported on NPG at lower temperatures.²¹ Given the inherent increase in catalytic activity of NPG to a variety of potential fuels, like methanol and formic acid, capitalizing on this high oxidation reactivity has been reported via the introduction of platinum onto the NPG framework.

The high surface area that is produced when preparing NPG, has allowed for the incorporation of a more catalytic material onto this substrate to improve ease of synthesis. The electrodeposition of platinum layers onto a porous surface has allowed for the production of nanoporous platinum materials with high catalytic activity. Dealloyed gold leaf was decorated with Pt by floating a NPG thin film on a solution of chloroplatinic acid (1g/L) and introducing the vapor of hydrazine hydrate (85%). The film surface was coated with a layer of Pt nanoislands and greatly increased the catalytic activity towards methanol oxidation.²² A more cost effective method was developed using potassium tetrachloroplatinate in 0.5 M H₂SO₄. The NPG

electrodes were submerged in a 20 mM solution and the potential was cycled 5 times from -0.2 V to 0.5 V. This allowed for the complete coverage of the porous gold surface with platinum and led to the enhancement of methanol oxidation.²³ The use of Pt has improved not only the oxidation of methanol,^{24–26} but ethanol,^{27–29} and formic acid^{30–32} as well. The desire to produce a highly active catalyst for direct oxidation fuel cells while reducing cost has driven the development for the minimal incorporation of Pt into a low-cost NPG electrode.

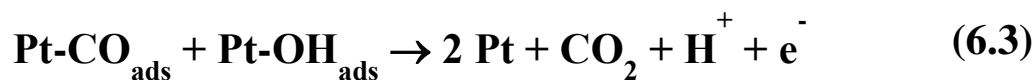
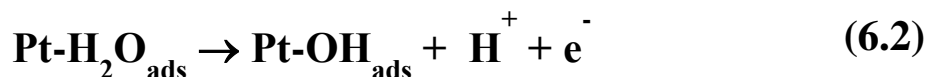
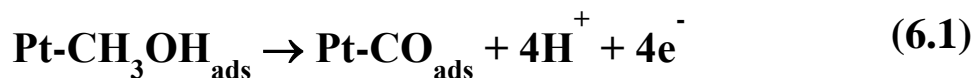
We have produced a low-cost, easily fabricated platinum-speckled nanoporous gold (NPG-Pt) electrode material fashioned on a glass substrate. This material uses an extremely small amount of platinum while still optimizing catalytic activity using the organization of this sparsely dispersed platinum throughout the nanoporous gold framework. Instead of coating the entirety of the NPG 3D framework, the platinum was speckled onto the NPG scaffold using a 2 second deposition cycling technique. By using a low concentration of platinum, a speckled effect was achieved throughout the pores of the NPG structure. The pairing of the NPG and platinum oxidative catalytic properties was shown to be as effective as a commercial planar platinum electrode in the electro-oxidation of methanol, ethanol and formic acid as potential fuels. Additionally, the NPG framework was positioned on a functionalized glass capillary tube, allowing for further cost reduction as well as a complete 360° oxidative surface and potential customization to fit in a functioning fuel cell.

6.2. Experimental Methods and Electrode Characterization

Experimental methods and electrode characterization were previously described in Chapter 5.

6.3. Electro-oxidation of Fuel Possibilities

To show catalytic activity of electrodes in the presence of methanol, NPG and NPG-Pt electrodes were first placed in a 0.5 H₂SO₄ solution, which was bubbled with N₂ for 15 minutes, and cyclic voltammetry was used to obtain a background plot. Once background scans were obtained, methanol was added to give a concentration of 1 M methanol and subsequent scans were obtained. The potential window for these scans was -0.1 to +0.7 V with a scan rate of 50 mV/s. The NPG electrodes showed an anodic peak around characteristic of the oxidation of residual silver remaining after the dealloying process. There was also an anodic peak at 1.4 V showing the formation of gold oxide in the forward scan and the corresponding cathodic gold reduction peak at 0.7 V (**Fig. 6.2**). There was a shown response following the addition of methanol. When compared to a planar platinum electrode, the NPG response shows an increase due to the responsive nature of gold to methanol in acidic media. The increase in the current shown can be attributed to the nanoporous nature of the gold by increasing the area exposed that can catalyze the oxidation of methanol. The Pt-speckled NPG electrodes, showed an even larger methanol oxidation peak 0.39 V in the forward scan and a second peak around 0.19 V in the reverse scan due to the presence of platinum in the porous framework and the increased activity of platinum versus gold in the electrooxidation of methanol. These peaks correspond to the oxidation of adsorbed methanol to adsorbed carbon monoxide in the forward scan and the further



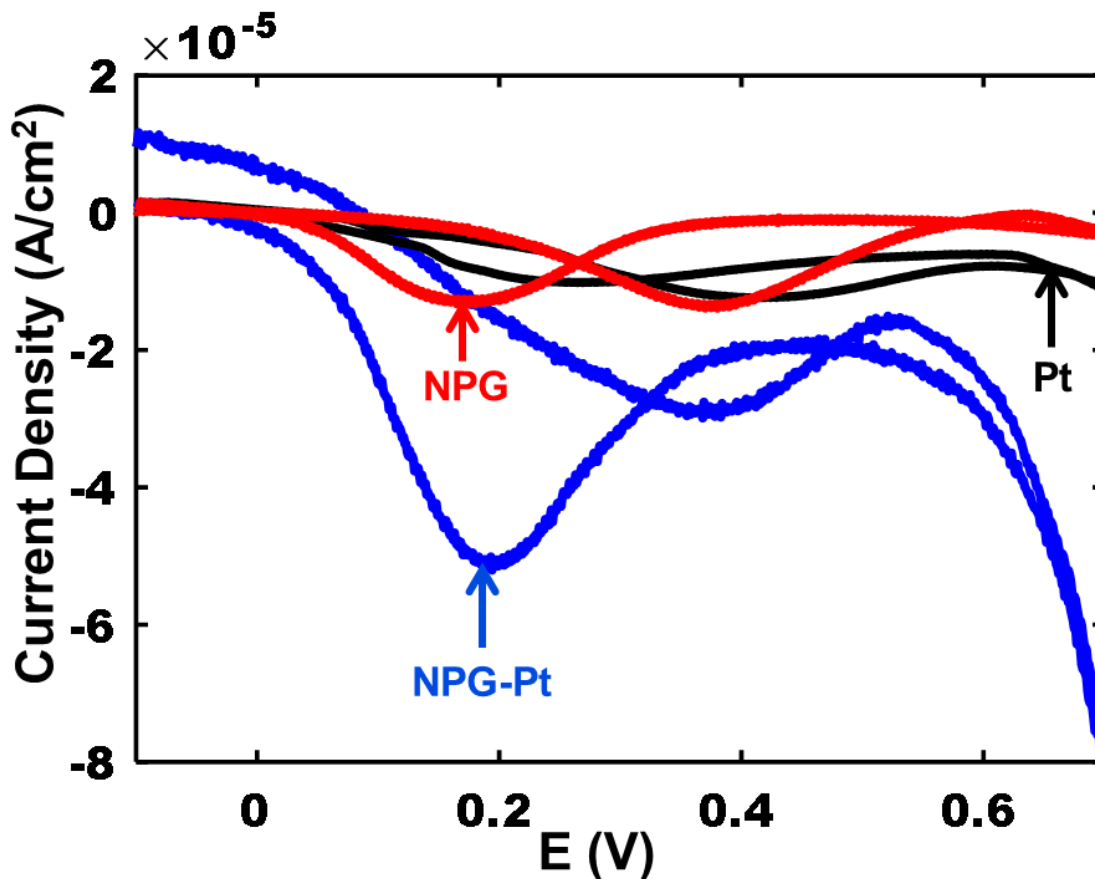


Figure 6.2. Cyclic voltammagram of methanol oxidation using NPG (**red**) commercial platinum (**black**) and NPG-Pt (**blue**) electrodes all at 1 M concentration in 0.5 M H₂SO₄. Potential window of -0.1 to 0.7 V, scan rate 50 mV/s.

oxidation of adsorbed carbon monoxide and adsorbed hydroxide to carbon dioxide in the reverse scan (Eq. 6.1).³ The efficiency of the NPG-Pt electrodes was shown to enhance the oxidation capacity towards methanol compared to both NPG and planar platinum electrodes (Fig. 6.2).

The catalytic activity of ethanol was then measured using the same procedure described to measure methanol activity except the potential window was adjusted to accommodate the oxidative response of ethanol from -0.2 to 1.2 V (Fig. 6.3). The two anodic peaks at 0.35 and 0.78 V, respectively, in the forward scan and the anodic peak at 0.1 V in the reverse scan all support the activity of ethanol on the NPG-Pt electrodes whereas the NPG electrodes only show the oxidative and corresponding reduction peak of gold oxide in the presence of 1 M ethanol in

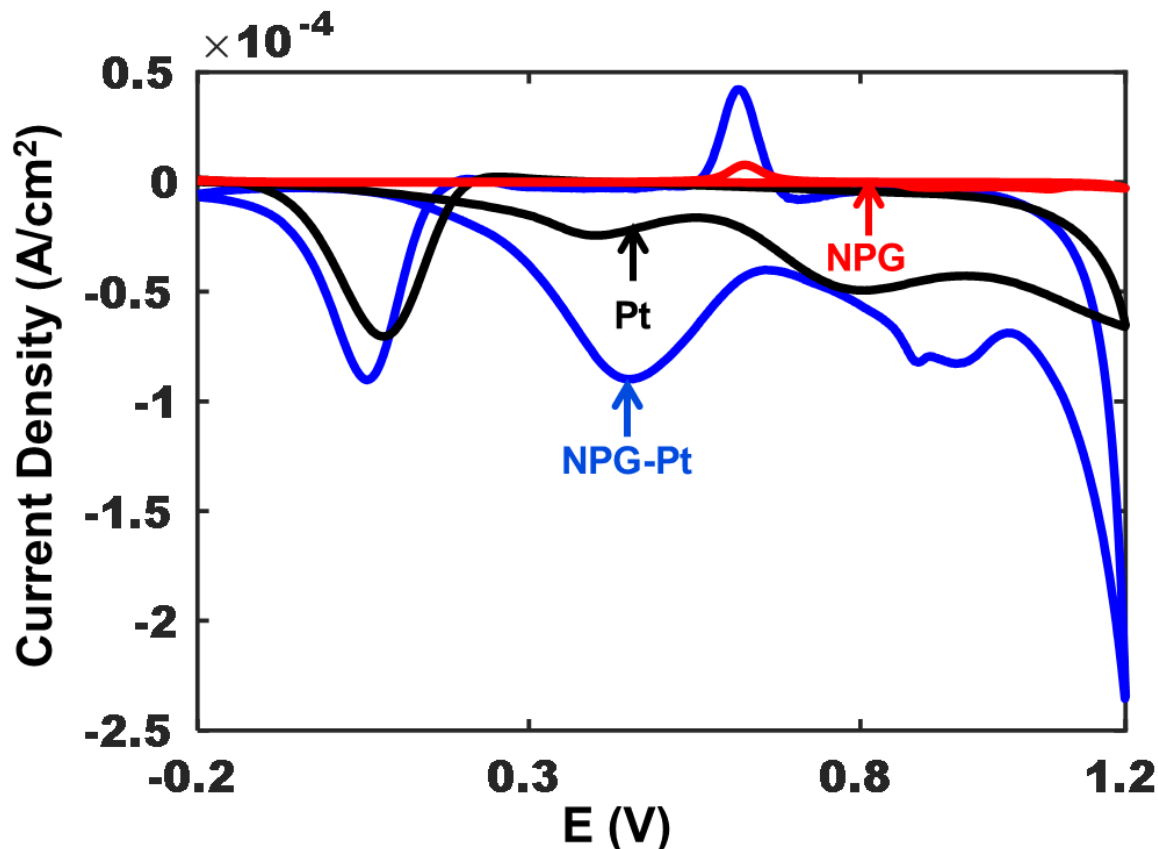


Figure 6.3. Cyclic voltammogram of ethanol oxidation peaks using NPG (**red**) commercial platinum (**black**) and NPG-Pt (**blue**) electrodes all at 1 M concentration in 0.5 M H₂SO₄. Potential window of -0.2 to 1.2 V, scan rate 50 mV/s.

0.5 M H₂SO₄. These results were again compared to a planar platinum electrode and the corresponding larger current densities for all three anodic peaks, characteristic of ethanol oxidation, show the benefit of using a NPG framework with a minimal deposition of platinum.

To further show the increased activity of platinum deposited electrodes, formic acid was also investigated to analyze the catalytic activity of platinum electrodes so it was expected to have a response on the Pt-speckled NPG electrodes and not on NPG alone. The potential window of -0.4 to 1.0 V showed a smaller anodic peak at -0.05 V in the forward scan and a larger peak at a similar potential in the reverse scan on the NPG-Pt electrodes and either a significantly reduced or non-existent response on the NPG electrodes alone (**Fig.6.4**). These two anodic peaks show

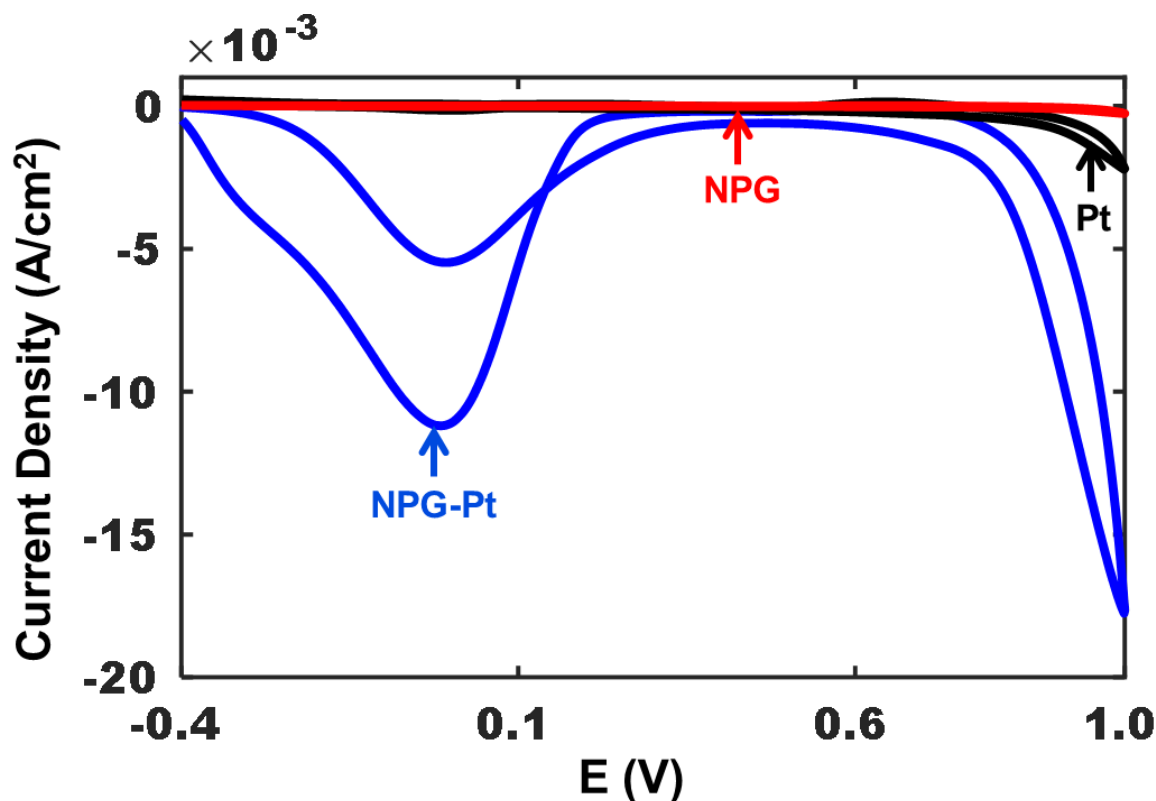


Figure 6.4. CV overlay of formic acid oxidation peaks using commercial platinum (dashed) and NPG-Pt (solid) electrodes in 0.5 MH₂SO₄. Potential window of -0.4 to 1.0 V, scan rate 50 mV/s.

the oxidation of formic acid to a deprotonated formic acid bonded to a platinum site and the subsequent oxidation of this bound species to carbon dioxide in the reverse scan for both planar platinum and fabricated NPG-Pt electrodes.

The activity of NPG-Pt electrodes were shown to be superior to both NPG and planar platinum electrodes in the presence of methanol and formic acid. In comparison to planar platinum electrodes in the presence of ethanol, the NPG-Pt electrodes showed similar and slightly enhanced activity. (**Table 6.1**)

Table 6.1. Comparison of electrooxidative current densities of platinum-speckled nanoporous gold (NPG-Pt), nanoporous gold (NPG), and planar platinum (Pt) electrodes in presence of different fuels in 0.5 M H₂SO₄.

| Fuel | Electrode Material | Peak current density ($\mu\text{A}/\text{cm}^2$) |
|-------------|---------------------------|--|
| Methanol | NPG-Pt | 50 |
| Methanol | NPG | 10 |
| Methanol | Pt | 10 |
| Ethanol | NPG-Pt | 75 |
| Ethanol | NPG | Not sufficiently active |
| Ethanol | Pt | 60 |
| Formic Acid | NPG-Pt | 11 mA/cm ² |
| Formic Acid | NPG | Not sufficiently active |
| Formic Acid | Pt | Not sufficiently active |

6.4. Conclusion

Previously reported fabrication of platinum-speckled nanoporous gold (NPG-Pt) electrodes were shown to have a comparable and enhanced activity in the electro-oxidation of three potential fuels to be used in direct oxidation fuel cells (DOFCs). The presence of platinum was shown to greatly increase the current density for oxidation of methanol and formic acid when compared to both nanoporous gold (NPG) electrodes and a commercial planar platinum electrode. The oxidation of ethanol showed similar activity between NPG-Pt electrodes and

planar platinum, both of which were greatly increased as compared to NPG only. The porous structure of the NPG substrate allows for an increased exposed surface area compared to the geometric area supporting the reduced size of fuel cells. Using acidic media works well due to the lack of destruction of the glass substrate and facile diffusion of protons to the cathode in a completed fuel cell.

6.5. References

1. Cacciola, G., Antonucci, V. and Freni, S. Technology up date and new strategies on fuel cells. *J. Power Sources* **100**, 67–79 (2001).
2. Kakati, N., Maiti, J., Lee, S. H., Jee, S. H., Viswanathan, B. and Yoon, Y. S. Anode catalysts for direct methanol fuel cells in acidic media: Do we have any alternative for Pt or Pt-Ru? *Chem. Rev.* **114**, 12397–12429 (2014).
3. Zainoodin, a. M., Kamarudin, S. K. and Daud, W. R. W. Electrode in direct methanol fuel cells. *Int. J. Hydrogen Energy* **35**, 4606–4621 (2010).
4. Cameron, D. S., Hards, G. a, Harrison, B. and Potter, R. J. Direct Methanol Fuel Cells: Recent Developments in the Search for Improved Performance. *Platin. Met. Rev.* **31**, 173–181 (1987).
5. Sheng, T., Xu, Y.-F., Jiang, Y.-X., Huang, L., Tian, N., Zhou, Z.-Y., Broadwell, I. and Sun, S.-G. Structure Design and Performance Tuning of Nanomaterials for Electrochemical Energy Conversion and Storage. *Acc. Chem. Res.* **49**, 2569–2577 (2016).
6. Wang, W., Lv, F., Lei, B., Wan, S., Luo, M. and Guo, S. Tuning Nanowires and Nanotubes for Efficient Fuel-Cell Electrocatalysis. *Adv. Mater.* **28**, 10117–10141 (2016).
7. Tian, X. L., Xu, Y. Y., Zhang, W., Wu, T., Xia, B. Y. and Wang, X. Unsupported Platinum-Based Electrocatalysts for Oxygen Reduction Reaction. *ACS Energy Lett.* 2035–2043 (2017). doi:10.1021/acsenergylett.7b00593
8. Sheng, T., Tian, N., Zhou, Z.-Y., Lin, W.-F. and Sun, S.-G. Designing Pt-Based Electrocatalysts with High Surface Energy. *ACS Energy Lett.* 1892–1900 (2017). doi:10.1021/acsenergylett.7b00385
9. Porter, N. S., Wu, H., Quan, Z. and Fang, J. Shape-control and electrocatalytic activity-enhancement of pt-based bimetallic nanocrystals. *Acc. Chem. Res.* **46**, 1867–1877 (2013).
10. Antolini, E. Structural parameters of supported fuel cell catalysts: The effect of particle size, inter-particle distance and metal loading on catalytic activity and fuel cell performance. *Appl. Catal. B Environ.* **181**, 298–313 (2016).
11. Xu, C., Wang, R., Chen, M., Zhang, Y. and Ding, Y. Dealloying to nanoporous Au/Pt alloys and their structure sensitive electrocatalytic properties. *Phys. Chem. Chem. Phys.* **12**, 239–246 (2010).
12. Reier, T., Nong, H. N., Teschner, D., Schlögl, R. and Strasser, P. Electrocatalytic Oxygen Evolution Reaction in Acidic Environments – Reaction Mechanisms and Catalysts. *Adv. Energy Mater.* **7**, (2017).
13. Strasser, P., Koh, S., Anniyev, T., Greeley, J., More, K., Yu, C., Liu, Z., Kaya, S., Nordlund, D., Ogasawara, H., Toney, M. F. and Nilsson, A. Lattice-strain control of the activity in dealloyed core–shell fuel cell catalysts. *Nat. Chem.* **2**, 454–460 (2010).
14. Freeman, C. J., Farghaly, A. A., Choudhary, H., Chavis, A. E., Brady, K. T., Reiner, J. E. and Collinson, M. M. Microdroplet-Based Potentiometric Redox Measurements on Gold Nanoporous Electrodes. *Anal. Chem.* **88**, 3768–3774 (2016).
15. Farghaly, A. a., Lam, M., Freeman, C. J., Uppalapati, B. and Collinson, M. M. Potentiometric Measurements in Biofouling Solutions: Comparison of Nanoporous Gold to Planar Gold. *J. Electrochem. Soc.* **163**, H3083–H3087 (2016).
16. Fujita, T., Guan, P., McKenna, K., Lang, X., Hirata, A., Zhang, L., Tokunaga, T., Arai, S., Yamamoto, Y., Tanaka, N., Ishikawa, Y., Asao, N., Yamamoto, Y., Erlebacher, J. and Chen, M. Atomic origins of the high catalytic activity of nanoporous gold. *Nat. Mater.* **11**,

- 775–780 (2012).
17. Krajčí, M., Kameoka, S. and Tsai, A. P. Understanding the catalytic activity of nanoporous gold: Role of twinning in fcc lattice. *J. Chem. Phys.* **147**, (2017).
 18. Wittstock, A., Biener, J. and Bäumer, M. Nanoporous gold: a new material for catalytic and sensor applications. *Phys. Chem. Chem. Phys.* **12**, 12919 (2010).
 19. Graf, M., Haensch, M., Carstens, J., Wittstock, G. and Weissmüller, J. Electrocatalytic Methanol Oxidation with Nanoporous Gold: Microstructure and Selectivity. *Nanoscale* **29**, 17839–17848 (2017).
 20. Pedireddy, S., Lee, H. K., Tjiu, W. W., Phang, I. Y., Tan, H. R., Chua, S. Q., Troadec, C. and Ling, X. Y. One-step synthesis of zero-dimensional hollow nanoporous gold nanoparticles with enhanced methanol electrooxidation performance. *Nat. Commun.* **5**, 4947 (2014).
 21. Mallat, T. and Baiker, A. Potential of Gold Nanoparticles for Oxidation in Fine Chemical Synthesis. *Annu. Rev. Chem. Biomol. Eng.* **3**, 11–28 (2012).
 22. Ge, X., Wang, R., Liu, P. and Ding, Y. Platinum-decorated nanoporous gold leaf for methanol electrooxidation. *Chem. Mater.* **19**, 5827–5829 (2007).
 23. Jia, J., Cao, L. and Wang, Z. Platinum-Coated Gold Nanoporous Film Surface : Electrodeposition and Enhanced Electrocatalytic Activity for Methanol Oxidation Platinum-Coated Gold Nanoporous Film Surface : Electrodeposition and Enhanced Electrocatalytic Activity for Methanol Oxidation. 8097–8101 (2008). doi:10.1021/la800163f
 24. Vega, A. A. and Newman, R. C. Methanol electro-oxidation on nanoporous metals formed by dealloying of Ag–Au–Pt alloys. *J. Appl. Electrochem.* **46**, 995–1010 (2016).
 25. Hamnett, A. Mechanism and electrocatalysis in the direct methanol fuel cell. *Catal. Today* **38**, 445–457 (1997).
 26. Kumar, S. and Zou, S. Electrooxidation of Carbon Monoxide and Methanol on Platinum-Overlayer-Coated Gold Nanoparticles: Effects of Film Thickness. *Langmuir* **23**, 7365–7371 (2007).
 27. Melke, J., Schoekel, A., Gerteisen, D., Dixon, D., Ettingshausen, F., Cremers, C., Roth, C. and Ramaker, D. E. Electrooxidation of ethanol on Pt. An in situ and time-resolved XANES study. *J. Phys. Chem. C* **116**, 2838–2849 (2012).
 28. Li, M. Electrocatalysts for Ethanol Oxidation in Direct Ethanol Fuel Cell (DEFC). (2011).
 29. Heinen, M., Jusys, Z., Chen, Y. X. and Behm, R. J. Ethanol, acetaldehyde and acetic acid adsorption/electrooxidation on a Pt thin film electrode: An in-situ ATR-IR spectroscopy flow-cell study. *J. Phys. Chem. C* **114**, 9850–9864 (2010).
 30. Ferreira Frota, E., Silva de Barros, V. V., de Araújo, B. R. S., Gonzaga Purgatto, Â. and Linares, J. J. Pt/C containing different platinum loadings for use as electrocatalysts in alkaline PBI-based direct glycerol fuel cells. *Int. J. Hydrogen Energy* **42**, 23095–23106 (2017).
 31. Zhu, Y., Ha, S. Y. and Masel, R. I. High power density direct formic acid fuel cells. *J. Power Sources* **130**, 8–14 (2004).
 32. Chen, A. and Holt-Hindle, P. Platinum-based nanostructured materials: Synthesis, properties, and applications. *Chem. Rev.* **110**, 3767–3804 (2010).

Chapter 7

Conclusions and Future Work

7.1. Conclusions

The investigation of nanoporous gold (NPG) electrodes fabricated on a gold substrate demonstrated the increased ability of the porous structure to resist electrode passivation due to the presence of the biofouling agent fibrinogen. Using a chemical dealloying method by submerging 12K gold leaf into concentrated acid for 13 seconds, the planar surface of a gold slide was modified with a nanostructured framework. The porous structure was shown to resist the loss of current due to the adsorption of fibrinogen onto the electrode surface. The signal reduction was very apparent on planar electrodes in cyclic voltammetry measurements, even at concentrations of 200 μM of the redox couple ferricyanide and ferrocyanide. Potentiometric experiments did not show a significant difference between planar and NPG electrodes at the starting concentration of 200 μM where both displayed Nernstian one-electron transfer slopes near 59.2 mV. However, as the concentration was reduced to 75 μM , a very large reduction (10 mV) in slope was seen in planar electrodes whereas the NPG electrodes maintained the same slope throughout. Additionally, in the presence of the biologically redox molecule ascorbic acid, potentiometric measurements showed a linear response after being subjected to biofouling and planar gold had no response to additions. CV measurements also showed a decrease in signal on planar gold versus NPG in the presence of fibrinogen. In addition, the potential was measured in human plasma and showed a marked difference in open-circuit potential. The porous structure of the NPG has allowed for the continued electron transfer of redox active species even in the presence of biofouling agents that led to the passivation of planar gold electrodes. The improved ability of the NPG electrodes to respond suggests a more accurate potential measurement of plasma due to the response of a larger number of redox active molecules present in the sample.

In order to decrease the cost of electrode fabrication while maintaining the porous framework and biofouling capability, electrodes were fabricated using a glass microscope slide functionalized with (3-mercaptopropyl) trimethoxysilane (MPTMS). The sulfur group on MPTMS was anchored to hydroxyl groups on the glass and dealloyed gold was captured on the surface. The immediate benefit was seen as a cost reduction as the glass microscope slides are a fraction of the price as gold-coated slides while preserving the reactivity of the porous framework. Additionally, the optical transparency of the glass substrate is exploited in coupling the fabricated electrode to an inverted microscope. This allowed for the visualization of minute sample volumes (280-1400 pL) on the electrode surface. The porous gold surface was submerged in hydrophobic hexadecane to eliminate the effects of evaporation. However, the surface required modification due to the hydrophilic nature of gold with 1-hexanethiol to improve droplet shape and deter the loss of sample into the porous framework. This allowed for the potential measurements of three sets of standard redox couples: ferri-ferrocyanide, ferric-ferrous ammonium sulfate, and hydro-benzoquinone. The first redox couple displayed the expected one-electron transfer Nernstian slope ~ 59.2 mV as did the second, one-electron transfer couple in nanoliter volumes. Due to the presence of both forms of a redox couple being present (poised system) the measurement were stabilized so, it was important to investigate the electrode response to only one form of a redox couple (unpoised). This was completed using ferricyanide and still showed an expected Nernstian one-electron transfer slope. All of the standard redox molecule validation supported the move to a biologically relevant redox molecule, ascorbic acid that was previously studied on NPG on gold electrodes. Interestingly, two slopes were obtained: a two-electron transfer slope (~ 29.6 mV) at low concentrations (100-300 μM) and a one-electron transfer slope (~ 59.2 mV) at higher concentrations (300 μM to 1.5 mM). The adsorption of

ascorbic acid on the surface of the electrode was suggested as a potential cause of electrode passivation reducing the available sites of electron-transfer. Ascorbic acid is known to adsorb on gold surfaces and has been proposed as part of the oxidation mechanism of ascorbic acid. The response of these electrodes to a variety of redox molecules using very small volumes has laid the groundwork for the fabrication of miniaturized electrodes.

In an effort to continue to reduce the overall cost of electrochemical analysis of redox molecule using NPG, a commonly available substrate was used to fabricate mini-nanoporous gold (mNPG) electrodes. Glass capillary tubes were functionalized with MPTMS and were used to capture dealloyed NPG. The cylindrical shape of the substrate and subsequent electrode allowed for the reduction the overall electrode size while increasing of electroactive surface area due to the utilization of the 3D porous Au framework. The reduction in size allowed for measurements in a drop size volume of 100 μ L. Electrodes were first validated using the ferri-ferrocyanide redox couple to ensure ideal Nernstian electrode behavior and displayed an expected one-electron transfer slopes (~ 59.2 mV). The previously established ability of NPG electrodes to respond to a biologically relevant redox molecule (ascorbic acid) was used to compare the behavior of mNPG electrodes, which were shown to behave in an expected fashion (two-electron transfer slopes ~ 29.6 mV). This advanced the investigation of two other relevant molecules, cysteine, and uric acid. Cysteine behaved in an expected fashion with a two-electron transfer slope, however, uric acid behaved somewhat unexpectedly. Uric acid has been shown to transfer two electrons in voltammetric experiments where oxidation is induced. In the potentiometric experiments, the electrochemical equilibrium that was reached between the electrode and uric acid suggest a one-electron transfer process. It is theorized this is due to the stability of the urate ion formed after the deprotonation of uric acid in pH 7.4. With the responses

of the molecules on mNPG electrodes, the library of potential redox active molecules was broadened to include glucose and hydrogen peroxide. Unfortunately, neither of these molecules showed a response to analyte addition, which precipitated the incorporation of an additional electrode material in the form of platinum due to the known ability of platinum to respond to both of these molecules. Using a short, two second electrodeposition in a low concentration (0.75 mM) of platinum salt, platinum was successfully incorporated into the Au structure producing Pt-speckled mini-nanoporous gold (mNPG-Pt) electrodes. The short deposition time and very low concentration coupled with the small solution volume (100 μ L) reduced the amount of platinum required which reduces the cost as compared to other reported platinum deposition methods. Platinum incorporation enhanced the response of electrodes to glucose and hydrogen peroxide, while showing a similar response in the presence of ferri-ferrocyanide, ascorbic acid, cysteine, and uric acid. The minimal deposition has increased the number of redox active molecules the mNPG-Pt electrodes respond to furthering the potential applications of these electrodes as biosensing platforms.

Finally, the known activity of platinum in the presence of fuels used in direct oxidation fuel cells stimulated the investigation of the catalytic ability of the previously described mNPG-Pt electrodes. Three electrodes were compared in the presence of methanol, ethanol, and formic acid, respectively, in acidic media as a potential anode material. The fabricated mNPG and mNPG-Pt electrodes were compared in addition to a commercial platinum electrode. The incorporation of platinum was clearly beneficial as shown in an increase in current density as compared to both mNPG and planar Pt commercial electrodes in the presence of methanol. When ethanol was used as a potential fuel, mNPG electrodes were not active enough to see a response as compared to the similar current densities seen on mNPG-Pt and commercial planar

Pt electrodes. The mNPG-Pt electrodes also showed an increased oxidation ability as compared to both mNPG and commercial planar Pt electrodes, which had a negligible response in comparison. This work provides a foundation upon which further testing can occur.

7.2. Future Work

Further research will focus on the coupling of microdroplet and miniaturized electrode fabrication methods to create biosensing devices. Additionally, great emphasis will put on further investigation of direct oxidation on fabricated electrodes for potential fuel cell applications.

7.2.1. Miniaturized Device Fabrication

The previously mentioned fabrication of microdroplet electrodes via the functionalization of glass microscope slides can be coupled with flow cell advancements.¹ A glass slide with micromachined channels can provide a platform on which a solution and sample can flow.^{2,3} A location, or multiple locations in the channels can be first functionalized with MPTMS and dealloyed gold can be captured creating an electroactive surface for the sample to interact. This can allow multiple measurements to be run simultaneously using a very small amount of sample.

7.2.2. Specific Surface Modification

The push to detect individual molecules down to nanomolar concentrations has provided numerous examples of how a surface can be modified to improve analyte detection. As was described previously, NPG is an excellent platform for the immobilization of enzymes,⁴ DNA probes,⁵ or antibodies⁶ directly on the surface. Using the instrumental setup used in the

microdroplet technique, specific areas of the electrode surface can be modified by immobilizing a target reactive site that produces a signal when in the presence of a target analyte.

7.2.3. Increased Platinum Loading for Direct Oxidation

The improvement of current density with the incorporation of platinum into the NPG framework can be further exploited through the investigation of increasing the platinum loading. Given the already small amount of platinum incorporated into the electrode structure as well as the small volume of plating solution used (100 μL) can be used to increase platinum without a dramatic increase in cost. An increase in deposition time or plating solution concentration, has been shown to produce a monolayer of platinum onto an underlying substrate.⁷ From what was shown in the direct oxidation chapter, the combination of NPG and Pt in the mNPG-Pt electrodes showed the best overall response to all three potential fuels. The investigation of increased platinum loading will identify an optimal percent of platinum incorporated to elicit the largest response without a substantial increase in electrode cost.

7.3. References

1. Chin, C. D., Linder, V. and Sia, S. K. Commercialization of microfluidic point-of-care diagnostic devices. *Lab Chip* **12**, 2118 (2012).
2. Wang, J., Tian, B. and Sahlin, E. Integrated electrophoresis chips/amperometric detection with sputtered gold working electrodes. *Anal. Chem.* **71**, 3901–3904 (1999).
3. Tantra, R. and Manz, A. Integrated potentiometric detector for use in chip-based flow cells. *Anal. Chem.* **72**, 2875–2878 (2000).
4. Zhang, S., Wang, N., Yu, H., Niu, Y. and Sun, C. Covalent attachment of glucose oxidase to an Au electrode modified with gold nanoparticles for use as glucose biosensor. *Bioelectrochemistry* **67**, 15–22 (2005).
5. Rashid, J. I. A. and Yusof, N. A. The strategies of DNA immobilization and hybridization detection mechanism in the construction of electrochemical DNA sensor: A review. *Sens. Bio-Sensing Res.* **16**, 19–31 (2017).
6. Moina, C. and Ybarr, G. Fundamentals and Applications of Immunosensors. *Adv. Immunoass. Technol.* (2012).
7. Banerjee, I., Kumaran, V. and Santhanam, V. Synthesis and characterization of Au@Pt nanoparticles with ultrathin platinum overlayers. *J. Phys. Chem. C* **119**, 5982–5987 (2015).

Vita
Christopher James Freeman

freemancj2@vcu.edu

EDUCATION**VIRGINIA COMMONWEALTH UNIVERSITY**

Ph.D. in Chemistry GPA: 3.9/4.0

Advisor: Dr. Maryanne Collinson

Dissertation: "Biosensing and Catalysis Applications of Nanoporous Gold (NPG) and Platinum-Speckled Nanoporous Gold (NPG-Pt) Electrodes."

Richmond, VA

May 2018

VIRGINIA COMMONWEALTH UNIVERSITY

B.S. in Chemistry GPA: 3.9/4.0

Dean's List: Spring 2008 to Spring 2011

Dean's Scholar Award

Richmond, VA

May 2011

**TEACHING
EXPERIENCE****VIRGINIA COMMONWEALTH UNIVERSITY****Department of Chemistry**

Richmond, VA

Jan 2013 –

Present

Organic Chemistry Lab, Teaching Assistant

19 sections averaging 22 students per section

- Supervised and assisted students in developing introductory and advanced organic synthesis techniques and instrumentation used to characterize products.
- Created written quizzes to challenge and encourage students as well as evaluated student understanding of technique and chemistry principles throughout lab.

Organic Chemistry Lecture, Teaching Assistant

8 sections averaging 200 students per section

- Assisted instructors in grading quizzes and exams.
- Met with students individually and in group sessions to further their understanding of course material and help identify particular areas of improvement.

General Chemistry Lab, Teaching Assistant

4 sections averaging 24 students per section

- Introduced students to general lab techniques and procedures.
- Focused proper formatting of laboratory notebook, data collection and analysis, and safety policies.
- Ongoing evaluation of student competency and understanding of recent experimental procedures.

General Chemistry Recitation, Teaching Assistant

4 sections averaging 30 students per section

- Engaged students through work on activities to clarify and reinforce main points of lecture.
- Administered quizzes based on the material presented.
- Responsible for grading activities, quizzes, and exams while providing feedback to students to improve.

Quantitative Analysis Lab, Teaching Assistant

2 sections averaging 20 students per section

- Supervised and assisted students in honing their analytical skill and techniques through solution preparation and analyte quantification.
- Taught students proper instrumental technique through hands-on experience with ion selective electrodes, gas chromatographic detection, UV-Vis spectrophotometric detection, fluorescence spectroscopy, and several titrations to calibrate glassware, standardize solutions, and calculate solute concentration.
- Supervised and evaluated student competencies in overall data analysis completed using linear regression and data fitting.

Quantitative Analysis Lecture, Teaching Assistant

3 sections averaging 140 students per section

- Assisted instructors in grading homework problem sets.
- Led student group sessions and worked through online and in-class homework problem examples as a supplement to main lecture.
- Guided students in how to prepare for quizzes and exams based on identifying individual areas of strength and deficiency.

GED TUTOR

Adult Career Development Center

Richmond, VA

Jan 2010 –

May 2010

- Worked with adults and minors individually and in small groups of 3-4 in pursuit of a high school diploma or GED
- Specialized in tutoring mathematics to at-risk youth

RESEARCH EXPERIENCE

VIRGINIA COMMONWEALTH UNIVERSITY

Department of Chemistry Graduate Research

Richmond, VA

Jan 2013–

Present

- Fabricated microdroplet, nanoporous gold (NPG) electrodes and investigated the response to biologically relevant molecules. Reduced sample volumes to nano- and picoliter range. Conducted open-circuit potential (OCP) measurements using several oxidation-reduction potential (ORP) calibrants as well as ascorbic acid.
- Developed method of NPG electrode fabrication using glass capillary tubes to conduct OCP measurements in 100 microliter sample volumes. Measured response to several biologically relevant redox molecules (ascorbic acid, uric acid, and cysteine) in single-drop samples.
- Incorporated a minimal amount of platinum into the gold nanostructure (NPG-Pt) using electrodeposition to enhance response in the presence of glucose and hydrogen peroxide.
- Investigated the catalytic ability of NPG-Pt electrodes through the oxidation of methanol, ethanol, and formic acid as a potential anode material for direct oxidation fuel cells.

VIRGINIA COMMONWEALTH UNIVERSITY

Department of Chemistry Undergraduate Research

Richmond, VA

Jun 2010 –

Aug 2010

- Researched and tailored a technique of preparing porous gold samples captured on gold microscope slides.
- Characterized samples using electrochemical techniques in order to measure the change in sample surface area.
- Investigated porous gold as a platform for biological detection of relevant redox species.

PROFESSIONAL EXPERIENCE

IN-PROCESS CHEMISTRY TECHNICIAN Hospira, Inc.

Austin, TX
Jul 2012–
Dec 2012

- Responsible for in-process testing of IV products including UV/Vis spectroscopy, HPLC, flame photometry, osmometry, TOC analysis, polarimetry, and several chemical assays.

ASSISTANT STORE MANAGER

Richmond, VA

AandN Clothing Store

Oct 2007 –
Jan 2008

- Supervised a team of 5 employees.
- Responsibilities included: Overseeing store operations; store opening and closing procedures; control of safe and register monies; customer service and care; biweekly ad merchandising; freight control; scheduling.

DEPARTMENT MANAGER – ELECTRICAL Lowe's, Inc.

Richmond, VA
May 2004 –
Oct 2007

- Supervised a team of 7 employees.
- Responsibilities included: customer service and support; merchandising; inventory maintenance; shrink management; product resets; analysis of sales metrics and trends.

PUBLICATIONS

- “Microdroplet-Based Potentiometric Redox Measurements on Gold Nanoporous Electrodes.” **C. J. Freeman**, A. A. Farghaly, H. Choudhary, A. E. Chavis, K. T. Brady, J. E. Reiner, M. M. Collinson. *Anal. Chem.* **2016**, *88*, 3768–3774.
- “Potentiometric Measurements in Biofouling Solutions: Comparison of Nanoporous Gold to Planar Gold.” A. A. Farghaly, M. Lam, **C. J. Freeman**, B. Uppalapati. *Journal of the Electrochemical Society*, 163 (4) H3083–H3087 (2016).